Western Graduate&PostdoctoralStudies

Electronic Thesis and Dissertation Repository

11-10-2017 2:00 PM

Exploiting Temporal Image Information in Minimally Invasive Surgery

Jonathan McLeod
The University of Western Ontario

Supervisor
Dr. Terry Peters
The University of Western Ontario

Graduate Program in Biomedical Engineering
A thesis submitted in partial fulfillment of the requirements for the degree in Doctor of Philosophy
© Jonathan McLeod 2017

Follow this and additional works at: https://ir.lib.uwo.ca/etd

Part of the Biomedical Engineering and Bioengineering Commons

Recommended Citation

Abstract

Minimally invasive procedures rely on medical imaging instead of the surgeon's direct vision. While preoperative images can be used for surgical planning and navigation, once the surgeon arrives at the target site real-time intraoperative imaging is needed. However, acquiring and interpreting these images can be challenging and much of the rich temporal information present in these images is not visible. The goal of this thesis is to improve image guidance for minimally invasive surgery in two main areas. First, by showing how high-quality ultrasound video can be obtained by integrating an ultrasound transducer directly into delivery devices for beating heart valve surgery. Secondly, by extracting hidden temporal information through video processing methods to help the surgeon localize important anatomical structures.

Prototypes of delivery tools, with integrated ultrasound imaging, were developed for both transcatheter aortic valve implantation and mitral valve repair. These tools provided an on-site view that shows the tool-tissue interactions during valve repair. Additionally, augmented reality environments were used to add more anatomical context that aids in navigation and in interpreting the on-site video.

Other procedures can be improved by extracting hidden temporal information from the intraoperative video. In ultrasound guided epidural injections, dural pulsation provides a cue in finding a clear trajectory to the epidural space. By processing the video using extended Kalman filtering, subtle pulsations were automatically detected and visualized in real-time. A statistical framework for analyzing periodicity was developed based on dynamic linear modelling. In addition to detecting dural pulsation in lumbar spine ultrasound, this approach was used to image tissue perfusion in natural video and generate ventilation maps from free-breathing magnetic resonance imaging. A second statistical method, based on spectral analysis of pixel intensity values, allowed blood flow to be detected directly from high-frequency B-mode ultrasound video.

Finally, pulsatile cues in endoscopic video were enhanced through Eulerian video magnification to help localize critical vasculature. This approach shows particular promise in identifying the basilar artery in endoscopic third ventriculostomy and the prostatic artery in nerve-sparing prostatectomy. A real-time implementation was developed which processed full-resolution stereoscopic video on the da Vinci Surgical System.

Keywords: Augmented reality, TAVI, mitral valve repair, dural pulsation, Kalman filtering, state-space time series, dynamic linear modeling, Bartlett's test, Eulerian video magnification, nerve-sparing prostatectomy

Acknowledgments

I would like to express my sincere gratitude to my supervisor, Dr. Terry Peters, for his mentorship, friendship and support over all the years I have been working with him. I first joined Terry's lab as a summer student in high school in 2006. I have had the opportunity to learn so much from Terry and the collaborative environment he encourages in the lab is very special and enriching. Through these collaborations, I participated in many exciting projects and gained a much broader understanding of the field. I have also greatly enjoyed many summers of lab retreats and BBQs at his cottage. It has been an incredible journey.

I would also like thank my advisory committee Dr. Sandrine de Ribaupierre, Dr. Aaron Ward and Dr. Louis Collins. Their guidance has been invaluable and I very much appreciate all the time they have spent with me.

It has been a privilege to be able to work with surgeons and clinicians on the projects in this thesis. The work would not have been possible without their insight, time and expertise. I would like to thank Dr. Maria Currie, Dr. Bob Kiaii, Dr. Mike Chu and Dr. Dan Bainbridge with whom I worked on image-guided cardiac interventions, Dr. Sugantha Ganapathy on detecting dural pulsation for epidural injections and spinal anesthesia, Dr. Sandrine de Ribaupierre on ETV and Dr. Stephen Pautler on nerve sparing prostatectomy.

I have also had the opportunity to collaborate with other groups at Robarts and would like to acknowledge Dr. Matthew Lowerison, Dr. Hon Leong and Dr. James Lacefield for our work together on microvascular segmentations from B-mode ultrasound and Dante Capaldi and Dr. Grace Parraga for our work on using DLM for ventilation mapping from free breathing MRI. While doing my PhD, I did a six month internship at Intuitive Surgical. This was a fabulous experience. I would like to thank Dr. Mahdi Azzizian and Dr. Azad Shademan for their guidance and friendship. I would like to thank everyone from Terry's lab and Imaging at Robarts, in particular, Dr. John Baxter, Dr. Mohammad Kayvanrad, Dr. Pencilla Lang, Uditha Jayarathne, Golafsoun Ameri, Dr. Jonathan Lau, Dr. Martin Rajchl and Dr. Xiongbiao Luo for many valuable discussions and collaborations that have made this time so stimulating and fun. John Moore, Chris Wedlake and Dr. Elvis Chen, it has been great working with you. Your input, advice and help have been invaluable.

Finally, I would like to thank my parents, Ian and Maree, my brother, Matthew, and my grandparents for their love, support and encouragement. I am so grateful for everything you have done for me.

Coauthorship Statement

Once again, I would like to thank all of my coauthors without whom I would not have been able to accomplish the work described in this thesis. In all of the chapters and the papers on which they were based, my supervisor, Dr. Peters, provided invaluable insight, mentorship and guidance. The contributions of the other co-authors is summarized in this section.

Chapter 2: I developed the augmented reality guidance systems, performed the analysis and wrote the papers. All authors contributed to editing the papers. In the TAVI project, Dr. Maria Currie and I worked together on the specifications for the guidance system and planning the experiments. She also participated in the TAVI experiments. John Moore created the phantoms for both the TAVI and Neochord project, did the computer aided design of the NeoChord tool and provided general guidance and help with running the experiments. Dr. Daniel Bainbridge, Dr. Bob Kiaii and Dr. Michael Chu provided insightful clinical guidance.

Chapter 3: I developed the EKF method for detecting dural pulsation, designed the experiments, performed the analysis and wrote the papers. All authors contributed to editing the paper. Dr. Sugantha Ganapathy identified dural pulsation as a cue to enhance, acquired the ultrasound videos and participated in the phantom experiments. Dr Elvis Chen created the phantom and helped extend his augmented reality guidance system to include the dural pulsatile cues as seen in Section 3.4.1. Dr. John Baxter and Golafsoun Ameri contributed many fruitful discussions and assisted in running the experiments.

Chapter 4: I developed the DLM method for analysing periodicity in image sequences. I collected and analysed the natural video examples and applied this method to the ultrasound data from Chapter 3. Dante Capolti proposed applying this method to FDMRI and Dr. Grace Parraga provided the MRI data for this final example. Dr. John Baxter contributed many suggestions and discussions and assisted in preparing this work for publication. Dr. Xiongbiao Luo provided valuable discussions and feedback.

Chapter 5: I developed the B-mode blood segmentation method, designed and analysed the experiments and wrote the paper. Dr. Mattew Lowerison suggested we look into processing blood flow from B-mode ultrasound and collected the data, including the ground truth segmentations. I had many valuable discussions and a productive collaboration with him on this project. Dr. Mai Elfarnawany provided the code and expertise for the conventional Doppler processing. Ashley Makela tuned the ultrasound acquisition parameters. I also received valuable feedback and guidance from Dr. Hon Leong and Dr. James Lacefield. Dr. Leong provided the chick embryo models used in this study and Dr. Lacefield provided guidance and insight into blood flow measurements and high frequency ultrasound.

Chapter 6: I implemented EVM and developed techniques for artifact reduction and wrote the papers. Dr. Sandrine de Ribaupierre provided the ETV videos and clinical feedback.

iv

Contents

vii

List of Figures

List of Tables

List of Abbreviations, Symbols, and Nomenclature

2D: two dimensional
3D: three dimensional
AR: augmented reality
AUC: area under curve
AV: aortic valve
bpm: beats per minute
CAM: chorioallantoic membrane
CPD: color pixel density
CT: computed tomography
DLM: dynamic linear models
DOF: degrees of freedom
EKF: extended Kalman filter
EKG: electrocardiogram
EMA: exponential moving average
ETV: endoscopic third ventriculostomy
EVM: Eulerian video magnification
FDMRI: Fourier decomposition magnetic resonance imaging
FPR: false positive rate
fps: frames per second
GPU: graphics processing unit
ICE: intracardiac echocardiography
IQ: quadrature demodulated
MLE: maximum likelihood estimate
MRI: magnetic resonance imaging
MV: mitral valve
PPG: photoplethysmogram
QPI: quadratic peak interpolation
RMSE: root mean square error
ROC: receiver operating characteristic
ROI: region of interest
SNR: signal to noise ratio
TAVI: transcatheter aortic valve implantation
TEE: transesophogeal echocardiography
TPR: true positive rate
US: ultrasound
VEGF: vascular endothelial growth factor

Chapter 1

Introduction

Surgery is an invasive but necessary course of treatment for many patients, accounting for 1.4 million of the 3.0 million annual inpatient hospitalizations in Canada[1]. Much of the trauma and complications associated with open surgery is caused by gaining access to tissue deep within the body. Minimally invasive procedures can reduce these side-effects by keeping the patient closed and operating through small keyhole insertions [2, 3, 4], percutaneously [5, 6, 7, 8] or through the patient's natural orifices [9]. However, without open surgical access the surgeons are forced to rely on medical imaging to guide the procedure as they no longer have direct visual access inside the patient.

Historically, minimally invasive procedures have addressed this challenge in two main ways. Traditional image-guided interventions (IGI) had their origins in stereotactic neurosurgery where computed tomographic imaging allowed the position tracked surgical tools to be displayed relative to preoperative images of the patient's anatomy. As the images were acquired before the surgery began, only the position of the surgical tools can be updated intraoperatively. This approach is well suited to situations where the target tissue is relatively stationary and, once the target site is reached, the surgical procedure is simple.

Other minimally invasive procedures rely on intraoperative imaging to visualize both the patient's anatomy and surgical tools. Since the images are acquired live, tissue motion is not so much of a problem and more complex surgical tasks can be performed, such as laparoscopic suturing or catheter stent deployments. However, the type and quality of the images are limited by the constraints of the operating room environment and the need for real-time feedback.

Increasingly, minimally invasive procedures seek to combine preoperative images, which can take advantage of the tissue contrast and high-resolution attainable in diagnostic scans, with intraoperative imaging to provide real-time feedback during surgery. For instance, SonoWand is a neuronavigation system that includes intraoperative ultrasound. Both real-time 2D ultrasound and free-hand 3D reconstructions can be acquired intraoperatively [10, 11]. The 3D ultrasound has proved particularly useful for tumor resections where large amounts of brain shift can occur as the surgery progresses. Continuous fluoroscopy is frequently used in deep brain stimulation to monitor lead placement (Figure 1.1). This real-time imaging is used to prevent electrode tip migration and detect intracranial hemorrhaging [12].

On the other hand, procedures that rely primarily on intraoperative imaging are seeking to augment the real-time video with more spatial context and anatomical knowledge derived from preoperative imaging. In minimally invasive cardiac surgery, preoperative CT volumes can be registered to intraoperative fluoroscopy [13] or ultrasound [14, 15] to help identify important anatomy and reduce the use of nephrotoxic contrast agents for fluoroscopy. Endoscopic video can also be augmented with peroperative data to show information that would otherwise be invisible to the surgeon. This includes tumors [16, 17] and critical vasculature [17, 18, 19] and nerves [19].
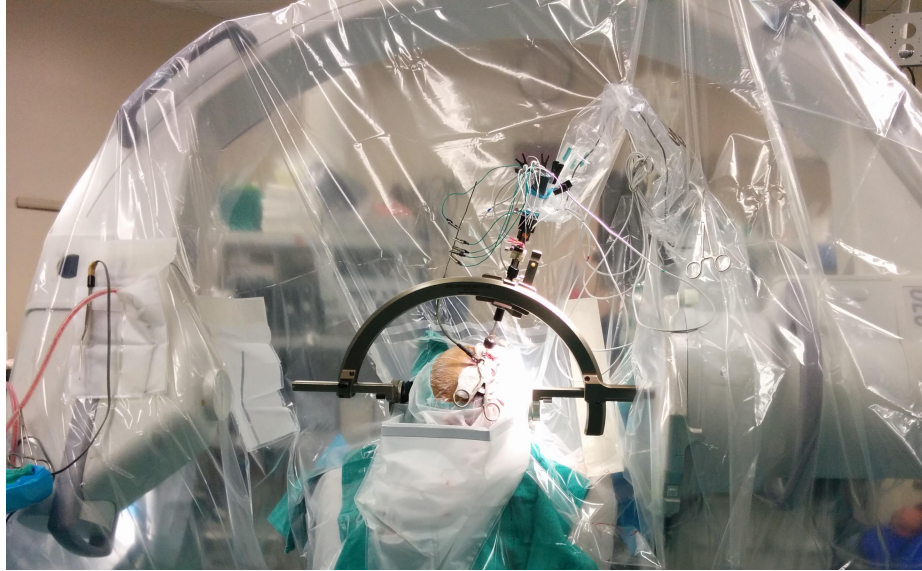
Figure 1.1: Stereotactic deep brain stimulation with real-time fluoroscopic imaging. The centre of the stereotactic frame is aligned with the surgical target, ie globus pallidus. As the leads are placed, continous fluoroscopy is acquired with the C-arm.

The goal of this thesis is to improve real-time image guidance for minimally invasive surgery in two main areas. Firstly, by developed surgical tools with integrated ultrasound imaging to provide feedback for monitoring tool-tissue interactions during beating heart surgery. Secondly, by extracting hidden temporal information from intraoperative video that can be used to localize arteries as well as other vasculature and important structures.

1.1 Image-Guided Surgery

Image-guided surgery emerged as a field approximately 30 years ago when newly developed computed tomography (CT), in combination with stereotaxy, was used to visualize target tissue deep within the patient's brain. Neurosurgery was particularly well suited to image guidance for a number of reasons:

- **Static environment:** Brain tissue is relatively stationary allowing preoperative images acquired well before the surgery to be used for intraoperative guidance. Although some brain shift occurs during surgery due to the loss of cerebral spinal fluid, this displacement is most prevalent at the cortical surface and is less significant for deep brain targets [20].

- **Rigid skull:** The patient's skull provides landmarks and a solid base needed to affix the stereotactic frame. It also allows for stable skin markers and natural landmarks on the patient's head to be used for registration with frameless neuronavigation systems.

- **Non-regenerative tissue:** By necessity, neurosurgery must be minimally invasive. Damage to eloquent regions of the brain can result in severe and irreversible side-effects. Since there is no open surgical alternative to accessing targets deep within the brain, direct vision is impossible and surgeons must rely on imaging or their anatomical knowledge to reach these targets.

- **Simple surgical objectives:** Dramatic functional changes in the brain can be achieved by removing or ablating small amounts of tissue, or through implanting electrodes. Once the target site is reached, these tasks are relatively simple to perform and can often be performed without additional imaging.

After the initial success in neurosurgery, other surgical and non-surgical procedures adopted similar guidance. The same fundamental problem of bringing the preoperative images of the patient and tracked surgical tools (or other interventional devices) into a common coordinate system occurs in many other fields including orthopedic surgery [21, 22], percutaneous interventions [23], and radiation therapy [24]. Galloway and Peters [25] divided image guided interventions into five subprocesses.

1 **Collect preoperative data:** The first step in image-guided interventions is to acquire the preoperative images that will be used for guidance.

2 **Track surgical tools:** The location of the surgical instruments must be tracked. This is usually accomplished using either mechanical, optical or magnetic systems.

3 **Register tracking system, preoperative data and patient into common coordinate system:** The preoperative images and tracking system need to be registered to the patient. This is typically accomplished by identifying homologous landmarks on the preoperative images (in image space) and on the patient (in tracker space).

4 **Display position of the tool relative to structures visible in preoperative data:** The position of the tool is visualized relative to preoperative data to guide the surgeon to the target.

5 **Account for differences between preoperative data and intraoperative reality:** After registration, there will still be some residual error. As the surgery progresses larger errors may be introduced and need to be corrected.

This paradigm for image-guided interventions seeks to maintain up-to-date locations of the surgical tools within a mostly static reference image. This is accomplished in the first four subprocesses where preoperative images are acquired, registered into a common co-ordinate system with the patient and tracked surgical tools, and displayed to the surgeon. Here, the only real-time feedback provided to the surgeon is through updating the location of the tracked tools. The fifth subprocess attempts to correct for differences between the preopertive data and reality and usually consists of using intraoperative imaging, such as ultrasound, to update the registration [26] or acquiring a new image volume intraoperatively

to serve as the reference [10, 27]. This type of image guidance works very well for navigating to a target site. However, once the target site is reached the guidance system offers little help in positioning or manipulating the tools to accomplish complex surgical tasks. Modern navigation systems are accurate to 3mm after initial registration and become worse as the surgery progresses [28]. This level of accuracy is sufficient for positioning an electrode within the right anatomical region, such as the globus pallidus or subthalamus, but not for achieving satisfactory margins during tumor resection. In addition, the lack of real-time image feedback to monitor tool-tissue interactions limit the surgeon to performing only the most simple actions once the target site is reached.

1.1.1   Preoperative Imaging

One of the advantages of image-guided interventions is the ability to use a wealth of different imaging technologies to reveal more information than would otherwise be visible to the surgeon. Preoperative imaging is typically performed in a diagnostic imaging suite well in advance of the actual surgery. Traditional diagnostic modalities such as CT, magnetic resonance imaging (MRI) and nuclear medicine are used to acquire detailed structural and functional information to help guide the surgery.

Volumetric Imaging

Preoperative images must cover the entire surgical volume so the tracked tools can be related to the patient's anatomy as the procedure progresses. The first human stereotactic system developed by Spiegel et al. [29], preceded the development of volumetric imaging and instead used two orthogonal x-ray projection images so that the coordinates of anatomical landmarks visible in both images could be calculated and used during navigation. Later, CT

enabled the reconstruction of full image volumes from multiple x-ray projections. When used in a navigation system, the position of the tracked tools could be shown precisely in the patient's anatomy. Other modalities, including MRI, nuclear medicine, and ultrasound can all produce volumetric images used for image-guided surgery.

Tissue Contrast

The images used for IGI need to show the important anatomical structures to the surgeon. CT images are formed based on the x-ray attenuation of the tissue being imaged. While these images provide excellent contrast between bone, soft-tissue and air, distinguishing between different types of soft tissue is challenging. In CT angiography, high contrast between vasculature and surrounding tissue is obtained by administering an intravenous radiopaque contrast agent. These images are frequently used for image-guidance in cardiac interventions[30] and neurosurgery[31]. However, one of the great strengths of MRI is its ability to obtain good soft tissue contrast. The pulse sequence of the MRI scan determines how the magnetic relaxation properties of hydrogen atoms in the tissue contribute to the final image and can be tuned to suit the desired application.

Functional Imaging

Besides obtaining structural information, preoperative imaging techniques have been developed to measure functional properties of tissue. This can provide important information that would otherwise be invisible to the surgeon. Functional MRI measures changes in blood oxygenation as a proxy for brain activity. Eloquent areas of the brain can be identified preoperatively and loaded into the neuronavigation system to help protect the patient's language, vision and motor function [32, 33]. Positron emission tomography can localize

tumors by imaging their high glucose metabolism. These images can then be used to guide minimally invasive surgery [34] and radiation therapy [35] in cancer patients.

1.1.2   Tracking Technologies

In stereotactic surgery the reference coordinate system is set by the stereotactic frame which is rigidly affixed to the patient's skull. Frameless neurosurgery, and most non-neurosurgical applications of IGI use either magnetic or optical tracking to track the location of the surgical tools.

Optical Tracking

Optical tracking systems use cameras to triangulate the position of fiducials mounted on the surgical tools. Active tracking systems use a series of infrared LEDs mounted on the surgical tool. These LEDs are pulsed one at a time so they can be uniquely identified by at least two cameras. Passive systems replace the LEDs with highly reflective spheres while an infrared light source mounted in the tracking system illuminates the scene. Since all the fiducials are imaged simultaneously they must be identified from their spatial configuration on the surgical tools. Videometric systems extract the location of fiducials by processing images of an easily recognizable pattern, such as a checkerboard. Optical tracking systems can achieve a very high degree of accuracy, with tracking errors of approximately 0.25mm [36]. However, they require a clear line of sight between the tracking system and the fiducials mounted on the tools. This can be encumbering in the operating room environment and is impossible to achieve with non-rigid tools once they are inserted into the patient.

Magnetic Tracking

Magnetic tracking uses a field generator to induce current in small solenoids mounted on the surgical tools. These systems do not require a direct line of sight, and the sensor, 1-2mm in diameter, can easily be integrated into surgical tools. However, the volume over which tools can be tracked is smaller than optical systems, requiring the field generator to be placed near the patient. Furthermore, metal objects interfere with tracking accuracy.

1.2 Intraoperative Imaging

Endoscopy, fluoroscopy and ultrasound are all routinely used in minimally invasive interventions to provide real-time image feedback replacing the surgeon's direct vision.

1.2.1 Endoscopy

The first diagnostic and interventional endoscopes required the clinician to look through the eyepiece of an optical device. First analog and then digital cameras removed this constraint by acquiring video feed which was displayed on a monitor in the operating room [37]. This provided the rest of the operating room staff with an endoscopic view and freed the surgeon from having to peer through the eyepiece.

1.2.2 Fluoroscopy

In fluoroscopy, x-ray images are acquired and displayed to the clinician in real-time. Originally, this was accomplished using a screen that fluoresced when exposed to x-ray radiation (Figure 1.2). These screens could be handheld or head-mounted; however, they required

Figure 1.2: A surgeon extracts a bullet under fluoroscopic guidance at an army hospital in France during the first world war. Credit: The Book of Modern Marvels, Leslie-Judge Company, 1917 - Digitized by Google Books

large doses of continuous x-ray radiation to produce faint images on the display. Fluoroscopy now uses the same flat panel detectors used in x-ray and cone-beam CT systems, which are usually capable of acquiring intraoperative real-time fluoroscopy.

1.2.3 Ultrasound

Ultrasound is an attractive modality for intraoperative imaging. When compared with CT and MRI systems, ultrasound scanners are compact and can easily be integrated into the operating room environment and surgical workflow. To form an image, the piezoelectric transducer transmits ultrasonic pulses which are then reflected back wherever there is a change in acoustic impedance. This occurs both on the interface between different tissue types, such as the interface between bone and softer tissues, and due to small scatterers within tissue, such as erythrocytes in blood. The ultrasound image is reconstructed based

on the speed of sound, and the time elapsed before the echos are received. Typically 2D B-mode ultrasound is used for guiding interventions [38]. However, 3D ultrasound reconstructed from freehand B-mode scans [10], as well as real-time 3D imaging through a matrix phased array probe [39], are also used intraoperatively.

1.2.4   Magnetic Resonance Imaging

MRI is difficult to integrate into surgical workflow since it usually requires a specialized operating room with electro-magnetic shielding and specialized, non-metallic, surgical beds, tools, and other devices. In addition, the small bore of diagnostic scanners greatly limit the surgeon's access to the patient. Some specialized open bore MRI systems have been developed to allow greater access to the patient. However, field strength and homogeneity are lower, reducing image quality in these systems. To maintain image quality, closed bore, rail mounted MRI systems have been developed so that updated images can be acquired intraoperatively [27]. Another class of non-surgical interventions can be performed inside the bore of a conventional MRI scanner, including percutaneous needle interventions [40], cardiac catheter procedures [41] and high intensity focused ultrasound ablations [42, 43].

1.2.5   Cone Beam Computed Tomography

Cone beam CT uses a flat panel detector and x-ray source mounted on a rotational gantry, often called a C-arm due to its shape, to reconstruct 3D volumes from a series of 2D projection images. This enables fast acquisitions of the entire volume with a single rotation of the gantry. In addition, cone beam CT systems can also be used to acquire real-time fluoroscopy enabling a seamless workflow where the perioperatively acquired CT volume is inherently registered to live fluoroscopy. In TAVI (transcatheter aortic valve implantation)

procedures using the DynaCT, first a 3D volume showing the anatomy of the aortic root is acquired before switching to fluoroscopy to guide valve deployment [44, 45].

1.3   Augmented Reality Environments

Broadly speaking, augmented reality environments combine real and virtual objects and images. In medical interventions, such environments can be used to fuse spatial and temporal information from many different sources, including preoperative imaging, intraoperative imaging, and tool tracking data.

1.3.1   Milgram's Taxonomy

The term, augmented reality, has been used to describe a wide range of environments. Milgram proposed a taxonomy for describing display environments that include mixtures of virtual and real objects and images [46]. These environments were placed on a continuum (Figure 1.3) from entirely real environments to entirely virtual. The term mixed reality is used to refer to all systems with a mixture of real and virtual elements and a distinction is made between augmented reality, where reality is augmented with virtual objects and augmented virtuality, where the environment is primarily virtual but includes some real images or objects. However, this distinction is often blurred in systems that use extensive virtual models with a difficult to interpret imaging modality, such as ultrasound. The terms augmented reality [47, 48], mixed reality [49] and augmented virtuality [50] are all used in the literature to refer to systems displaying real-time tracked ultrasound together with virtual representations of tracked tools and important anatomical structures.
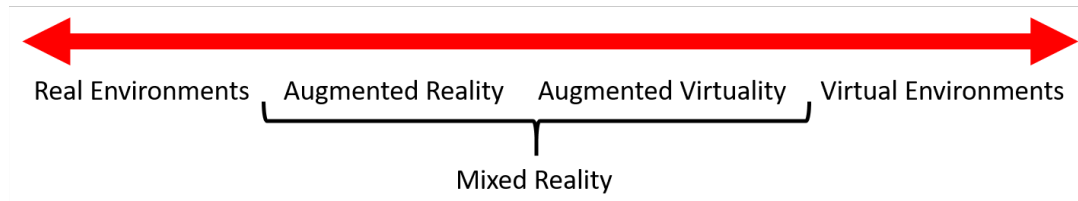
Figure 1.3: Milgram's virtuality continuum categorizes different display environments based on their mixture of real and virtual objects.

1.3.2 Display Strategies

The augmented reality environment needs to display real and virtual information to the surgeon. One strategy is to display images and virtual objects directly onto the patient. This can be accomplished using head-mounted displays [51], half silvered mirrors [52], or by projecting graphics directly onto the patient [53]. Alternatively, an auxiliary monitor can introduced to the operating room to bring all the elements of the augmented reality environment into a single display. Finally, when the surgery is performed primarily using intraoperative imaging, as is the case for many endoscopic and fluoroscopic procedures, virtual elements can be overlayed on this video without requiring additional displays or otherwise changing the surgical workflow.

1.4 Research Challenges

Modern minimally invasive interventions rely increasingly on intraoperative imaging to perform more sophisticated surgical tasks without the need for open surgery. However, the type and quality of this imaging is often limited by the constraints of the operating room environment. This thesis aims to improve guidance for minimally invasive surgery in two main areas:

1 Using intraoperative ultrasound to guide cardiac valve surgery

Beating heart aortic and mitral valve surgery rely predominately on fluoroscopy and transesophageal ultrasound for guidance. However, fluoroscopy requires the use of nephrotoxic contrast agents and transesophageal ultrasound suffers from severe artifacts once the surgical tools have been introduced into the heart. We address these issues by integrating a small ultrasound transducer array directly into the delivery tool for TAVI and neochordae implantation.

2 Extracting hidden temporal information from intraoperative video

While intraoperative video shows the gross motions of tools and tissue, it also contains considerable information that is not obvious to the surgeon. The cardiac and respiratory cycles induce subtle changes in the video, which can, among other things, provide cues as to the location of critical vasculature. We aim to develop methods for extracting this information through temporal processing and to apply them to intraoperative ultrasound and endoscopic video.

1.5   Thesis Outline

This thesis is presented in integrated article format with Chapters 2-6 derived from journal articles and conference proceedings. Some of these chapters combine two closely related publications and additional material has been added throughout the thesis to improve the flow and address interesting points relating to the research not covered in the original publications. I was the first author of the papers from which these chapters were derived and was responsible for developing the proposed methods, designing and conducting the experiments and analyzing results. My sincere thanks goes to all of my co-authors, who

contributed their expertise, time and resources to these projects. This thesis would not have been possible without them.

1.5.1 Chapter 2: Ultrasound Guidance for Beating Heart Cardiac Surgery

One of the major challenges of minimally invasive cardiac valve surgery is the difficulty of obtaining real-time imaging inside the beating heart. Ultrasound is an attractive modality as it does not require nephrotoxic contrast agent or ionizing radiation. However, ultrasound images are difficult to interpret especially once the surgical tools are introduced as they create artifacts and occlusions in the image. We address this issue by integrating ultrasound directly into surgical devices for deploying TAVI valves and neochordae implants. This onsite ultrasound provides a direct view of the tissue where the implants are being deployed. In addition, augmented reality is used to provide more anatomical context. In phantom models, this onsite imaging with augmented reality performed as well as fluoroscopy in deploying TAVI valves. Furthermore, it showed potential in capturing the mitral leaflets for neochordae implantation while achieving consistent bite depth and spacing of the implants.

1.5.2 Chapter 3: Detection and Visualization of Dural Pulsation

While the previous chapter dealt with improving the acquisition and display of real-time intraoperative ultrasound, here we developed processing methods to extract subtle pulsations, a valuable cue in spine needle interventions where the pulsating dura can be used to find a clear needle trajectory to the epidural space. These pulsations were detected using extended Kalman filtering to find regions of the image that exhibited periodicity at the right frequency and amplitude. The processing ran in real-time on a commercial ultrasound

system. In phantom experiments, it was shown to decrease the number of attempts and re-
sulted in more direct needle trajectories when compared against conventional ultrasound
guidance. In addition, it was integrated into an augmented reality environment, similar to
the kind developed in Chapter 2, but with virtual models of spinal anatomy and the tracked
needle.

1.5.3   Chapter 4: Analysis of Periodicity in Video Sequences through Dynamic Linear Modeling

This chapter expands on the periodicity analysis from Chapter 3. In particular, dynamic
linear modeling was used to provide a more general statistical framework for analyzing
videos. Using this methodology, periodicity could be detected through a likelihood ratio
test along with maximum likelihood estimates of important model parameters. In addi-
tion to processing ultrasound videos, this approach succeeded in heart rate estimation and
perfusion mapping from natural video and ventilation imaging from free-breathing MRI.

1.5.4   Chapter 5: Microvasculature Segmentation from B-mode Ultra-sound Video Sequences

Time series analysis of medical videos is not limited to periodicity detection. In this chap-
ter, we show how Bartletts test, a statistical method based on the cumulative periodogram,
can be used to identify flowing blood in high frequency, microvasculature ultrasound. This
processing was performed on chick embryo models, which are commonly used for studying
angiogenesis in cancer, where it outperformed conventional power Doppler in segmenting
the microvasculature.

1.5.5 Chapter 6: Motion Magnification for Endoscopic Surgery

The other chapters on temporal video processing focused on the detection of pulsation and blood flow or explicit modeling where parameters, such as heart rate, were extracted from the videos. These tasks are much harder where complex motion patterns are visible. In this chapter we used Eulerian video magnification to enhance subtle pulsations in endoscopic videos. This approach produced very natural videos where the pulsation of important vasculature was increased, making them more salient. This chapter presented techniques for reducing artifacts and improving the quality of the enhanced video, as well as tracking the heart rate automatically through adaptive filtering. These techniques are applied to enhance the basilar artery in endoscopic third ventriculostomy and pulsations in the neurovascular area in radical prostatectomy. A local phase variant of Eulerian video magnification was implemented to run on the da Vinci Xi system, processing full resolution stereoscopic video in real-time. An ongoing retrospective study seeks to demonstrate the efficacy of these methods in finding the prostatic artery in robotic prostatectomy cases.

Bibliography

[1] Canadian Institute for Health Information. Inpatient hospitalizations,surgeries, new-borns and childbirth indicators, 2015-2016, 2017.

[2] Robert Reisch, Axel Stadie, Ralf A Kockro, and Nikolai Hopf. The keyhole concept in neurosurgery. *World Neurosurgery*, 79(2):S17–e9, 2013.

[3] Peter M Bonutti, Michael A Mont, Margo McMahon, Phillip S Ragland, and Mark Kester. Minimally invasive total knee arthroplasty. *JBJS*, 86(2):26–32, 2004.

[4] Lawrence H Cohn, David H Adams, Gregory S Couper, David P Bichell, Donna M Rosborough, Samuel P Sears, and Sary F Aranki. Minimally invasive cardiac valve surgery improves patient satisfaction while reducing costs of cardiac valve replacement and repair. *Annals of Surgery*, 226(4):421, 1997.

[5] Sigmund Silber, Per Albertsson, Francisco F Avilés, Paolo G Camici, Antonio Colombo, Christian Hamm, Erik Jørgensen, Jean Marco, Jan-Erik Nordrehaug, Witold Ruzyllo, et al. Guidelines for percutaneous coronary interventions: the task force for percutaneous coronary interventions of the european society of cardiology. *European Heart Journal*, 26(8):804–847, 2005.

[6] John G Webb, Lukas Altwegg, Robert H Boone, Anson Cheung, Jian Ye, Samuel Lichtenstein, May Lee, Jean Bernard Masson, Christopher Thompson, Robert Moss, et al. Transcatheter aortic valve implantation. *Circulation*, 119(23):3009–3016, 2009.

[7] Matthew R Cooperberg and Marshall L Stoller. Percutaneous neuromodulation. *Urologic Clinics*, 32(1):71–78, 2005.

[8] Tamas Ungi, Purang Abolmaesumi, Rayhan Jalal, Mattea Welch, Irene Ayukawa, Simrin Nagpal, Andras Lasso, Melanie Jaeger, Daniel P Borschneck, Gabor Fichtinger, et al. Spinal needle navigation by tracked ultrasound snapshots. *IEEE Transactions on Biomedical Engineering*, 59(10):2766–2772, 2012.

[9] Santiago Horgan, John P Cullen, Mark A Talamini, Yoav Mintz, Alberto Ferreres, Garth R Jacobsen, Bryan Sandler, Julie Bosia, Thomas Savides, David W Easter, et al. Natural orifice surgery: initial clinical experience. *Surgical Endoscopy*, 23(7):1512–1518, 2009.

[10] Aage Gronningsaeter, Atle Kleven, Steinar Ommedal, Tore Erling Aarseth, Torgrim Lie, Frank Lindseth, Thomas Langø, and Geirmund Unsgård. Sonowand, an ultrasound-based neuronavigation system. *Neurosurgery*, 47(6):1373–1380, 2000.

[11] Geirmund Unsgård, Ole Solheim, Frank Lindseth, and Tormod Selbekk. Intraoperative imaging with 3d ultrasound in neurosurgery. In *Intraoperative Imaging*, pages 181–186. Springer, 2011.

[12] Andre Machado, Ali R Rezai, Brian H Kopell, Robert E Gross, Ashwini D Sharan, and Alim-Louis Benabid. Deep brain stimulation for parkinson's disease: surgical technique and perioperative management. *Movement Disorders*, 21(S14), 2006.

[13] Amar Krishnaswamy, E Murat Tuzcu, and Samir R Kapadia. Three-dimensional computed tomography in the cardiac catheterization laboratory. *Catheterization and Cardiovascular Interventions*, 77(6):860–865, 2011.

[14] Pencilla Lang, Petar Seslija, Michael WA Chu, Daniel Bainbridge, Gerard M Guiraudon, Douglas L Jones, and Terry M Peters. Us–fluoroscopy registration for

transcatheter aortic valve implantation. *IEEE Transactions on Biomedical Engineering*, 59(5):1444–1453, 2012.

[15] Gang Gao, Graeme Penney, Yingliang Ma, Nicolas Gogin, Pascal Cathier, Aruna Arujuna, Geraint Morton, Dennis Caulfield, Jaswinder Gill, C. Aldo Rinaldi, Jane Hancock, Simon Redwood, Martyn Thomas, Reza Razavi, Geert Gijsbers, and Kawal Rhode. Registration of 3d trans-esophageal echocardiography to x-ray fluoroscopy using image-based probe tracking. *Medical Image Analysis*, 16(1):38 – 49, 2012.

[16] Takakazu Kawamata, Hiroshi Iseki, Takao Shibasaki, and Tomokatsu Hori. Endoscopic augmented reality navigation system for endonasal transsphenoidal surgery to treat pituitary tumors. *Neurosurgery*, 50(6):1393–1397, 2002.

[17] Li-Ming Su, Balazs P Vagvolgyi, Rahul Agarwal, Carol E Reiley, Russell H Taylor, and Gregory D Hager. Augmented reality during robot-assisted laparoscopic partial nephrectomy: toward real-time 3d-ct to stereoscopic video registration. *Urology*, 73(4):896–900, 2009.

[18] Ève Coste-Manière, Louaï Adhami, Fabien Mourgues, and Olivier Bantiche. Optimal planning of robotically assisted heart surgery: first results on the transfer precision in the operating room. *The International Journal of Robotics Research*, 23(4-5):539–548, 2004.

[19] Qinquan Gao, Ping-Lin Chang, Daniel Rueckert, S. Mohammed Ali, Daniel Cohen, Philip Pratt, Erik Mayer, Guang-Zhong Yang, Ara Darzi, and Philip Eddie Edwards". Modeling of the bony pelvis from mri using a multi-atlas ae-sdm for registration and tracking in image-guided robotic prostatectomy. *Computerized Medical Imaging and Graphics*, 37(2):183–194, 2013.

[20] Peter Hastreiter, Christof Rezk-Salama, Grzegorz Soza, Michael Bauer, Günther Greiner, Rudolf Fahlbusch, Oliver Ganslandt, and Christopher Nimsky. Strategies for brain shift evaluation. *Medical Image Analysis*, 8(4):447–464, 2004.

[21] DA Simon, RV Otoole, M Blackwell, F Morgan, AM DiGioia, and T Kanade. Accuracy validation in image-guided orthopaedic surgery. In *Proceedings of the Second International Symposium on Medical Robotics and Computer Assisted Surgery*, volume 6, pages 185–192, 1995.

[22] Uli Mezger, Claudia Jendrewski, and Michael Bartels. Navigation in surgery. *Langenbeck's archives of surgery*, 398(4):501–514, 2013.

[23] Bradford J Wood, Hui Zhang, Amir Durrani, Neil Glossop, Sohan Ranjan, David Lindisch, Eliott Levy, Filip Banovac, Joern Borgert, Sascha Krueger, et al. Navigation with electromagnetic tracking for interventional radiology procedures: a feasibility study. *Journal of vascular and interventional radiology*, 16(4):493–505, 2005.

[24] Thomas Rockwell Mackie, Jeff Kapatoes, Ken Ruchala, Weiguo Lu, Chuan Wu, Gustavo Olivera, Lisa Forrest, Wolfgang Tome, Jim Welsh, Robert Jeraj, Paul Harari, Paul Reckwerdt, Bhudatt Paliwal, Mark Ritter, Harry Keller, Jack Fowler, and Minesh Mehta. Image guidance for precise conformal radiotherapy. *International Journal of Radiation Oncology*Biology*Physics*, 56(1):89 – 105, 2003.

[25] Robert Galloway and Terry Peters. Overview and history of image-guide interventions. In Terry Peters and Kevin Cleary, editors, *Image-guided Interventions: Technology and Applications*. 2008.

[26] Roch M Comeau, Abbas F Sadikot, Aaron Fenster, and Terry M Peters. Intraopera-tive ultrasound for guidance and tissue shift correction in image-guided neurosurgery. *Medical Physics*, 27(4):787–800, 2000.

[27] Garnette R Sutherland, Isabelle Latour, and Alexander D Greer. Integrating an image-guided robot with intraoperative mri. *IEEE Engineering in Medicine and Biology Magazine*, 27(3):59–65, 2008.

[28] Lennart Henning Stieglitz, Jens Fichtner, Robert Andres, Philippe Schucht, Ann-Kathrin Krähenbühl, Andreas Raabe, and Jürgen Beck. The silent loss of neuron-avigation accuracy: a systematic retrospective analysis of factors influencing the mismatch of frameless stereotactic systems in cranial neurosurgery. *Neurosurgery*, 72(5):796–807, 2013.

[29] Edward A Spiegel, Henry T Wycis, M Marks, and AJ Lee. Stereotaxic apparatus for operations on the human brain. *Science*, 106(2754):349–350, 1947.

[30] Laurens F Tops, Jeroen J Bax, Katja Zeppenfeld, Monique RM Jongbloed, Hildo J Lamb, Ernst E van der Wall, and Martin J Schalij. Fusion of multislice computed tomography imaging with three-dimensional electroanatomic mapping to guide ra-diofrequency catheter ablation procedures. *Heart Rhythm*, 2(10):1076–1081, 2005.

[31] P. Jabbour, S. Tjoumakaris, and R. Rosenwasser. *Angiography, MRA in Image Guided Neurosurgery*, pages 299–305. Springer Berlin Heidelberg, 2009.

[32] I-A Rasmussen, F Lindseth, OM Rygh, EM Berntsen, T Selbekk, J Xu, TA Nagelhus Hernes, E Harg, A Håberg, and G Unsgaard. Functional neuronavigation combined with intra-operative 3d ultrasound: initial experiences during surgical resections close

to eloquent brain areas and future directions in automatic brain shift compensation of preoperative data. *Acta neurochirurgica*, 149(4):365–378, 2007.

[33] Joy Hirsch, Maximilian I Ruge, Karl HS Kim, Denise D Correa, Jonathan D Victor, Norman R Relkin, Douglas R Labar, George Krol, Mark H Bilsky, Mark M Souweidane, et al. An integrated functional magnetic resonance imaging procedure for preoperative mapping of cortical areas associated with tactile, motor, language, and visual functions. *Neurosurgery*, 47(3):711–722, 2000.

[34] V Braun, S Dempf, R Weller, S-N Reske, W Schachenmayr, and HP Richter. Cranial neuronavigation with direct integration of 11 c methionine positron emission tomography (pet) data–results of a pilot study in 32 surgical cases. *Acta Neurochirurgica*, 144(8):777–782, 2002.

[35] Michael MacManus, Ursula Nestle, Kenneth E Rosenzweig, Ignasi Carrio, Cristina Messa, Otakar Belohlavek, Massimo Danna, Tomio Inoue, Elizabeth Deniaud-Alexandre, Stefano Schipani, et al. Use of pet and pet/ct for radiation therapy planning: Iaea expert report 2006–2007. *Radiotherapy and Oncology*, 91(1):85–94, 2009.

[36] Andrew D Wiles, David G Thompson, and Donald D Frantz. Accuracy assessment and interpretation for optical tracking systems. In *Proceedings of SPIE*, volume 5367, pages 421–432, 2004.

[37] G Berci and KA Forde. History of endoscopy. *Surgical Endoscopy*, 14(1):5–15, 2000.

[38] Hans Henrik Holm and Bjørn Skjoldbye. Interventional ultrasound. *Ultrasound in Medicine & Biology*, 22(7):773–789, 1996.

[39] Andrea Colli, Erica Manzan, Fabio Zucchetta Fabio, Cristiano Sarais, Demetrio Pittarello, Giovanni Speziali, and Gino Gerosa. TEE-guided transapical beating-heart neochord implantation in mitral regurgitation. *JACC: Cardiovascular Imaging*, 7(3):322–323, 2014.

[40] Gregory S Fischer, Iulian Iordachita, Csaba Csoma, Junichi Tokuda, Simon P Di-Maio, Clare M Tempany, Nobuhiko Hata, and Gabor Fichtinger. Mri-compatible pneumatic robot for transperineal prostate needle placement. *IEEE/ASME Transactions on Mechatronics*, 13(3):295–305, 2008.

[41] Adrienne E Campbell-Washburn, Mohammad A Tavallaei, Mihaela Pop, Elena K Grant, Henry Chubb, Kawal Rhode, and Graham A Wright. Real-time MRI guidance of cardiac interventions. *Journal of Magnetic Resonance Imaging*, 2017.

[42] Ferenc A Jolesz. MRI-guided focused ultrasound surgery. *Annual Review of Medicine*, 60, 2009.

[43] Mario Ries, Baudouin Denis De Senneville, Sébastien Roujol, Yasmina Berber, Bruno Quesson, and Chrit Moonen. Real-time 3D target tracking in MRI guided focused ultrasound ablations in moving tissues. *Magnetic Resonance in Medicine*, 64(6):1704–1712, 2010.

[44] Jörg Kempfert, Volkmar Falk, Gerhard Schuler, Axel Linke, Denis Merk, Friedrich W Mohr, and Thomas Walther. DynaCT during minimally invasive off-pump transapical aortic valve implantation. *Ann Thorac Surg*, 88(6):2041, 2009.

[45] Koichi Maeda, Toru Kuratani, Kei Torikai, Kazuo Shimamura, and Yoshiki Sawa. Transcatheter aortic valve replacement using dynact. *Journal of cardiac surgery*, 27(5):551–553, 2012.

[46] Paul Milgram and Fumio Kishino. A taxonomy of mixed reality visual displays. *IEICE Transactions on Information and Systems*, 77(12):1321–1329, 1994.

[47] John T Moore, Michael WA Chu, Bob Kiaii, Daniel Bainbridge, Gerard Guiraudon, Chris Wedlake, Maria Currie, Martin Rajchl, Rajni V Patel, and Terry M Peters. A navigation platform for guidance of beating heart transapical mitral valve repair. *IEEE Transactions on Biomedical Engineering*, 60(4):1034–1040, 2013.

[48] Golafsoun Ameri, John SH Baxter, A Jonathan McLeod, Terry M Peters, and Elvis CS Chen. Augmented reality ultrasound guidance for central line procedures: Preliminary results. In *Workshop on Augmented Environments for Computer-Assisted Interventions*, pages 11–20. Springer, 2015.

[49] Cristian A Linte, Katherine P Davenport, Kevin Cleary, Craig Peters, Kirby G Vosburgh, Nassir Navab, Pierre Jannin, Terry M Peters, David R Holmes, Richard A Robb, et al. On mixed reality environments for minimally invasive therapy guidance: Systems architecture, successes and challenges in their implementation from laboratory to clinic. *Computerized Medical Imaging and Graphics*, 37(2):83–97, 2013.

[50] Terry M Peters and Cristian A Linte. Image-guided interventions and computer-integrated therapy: Quo vadis? *Medical Image Analysis*, 33:56–63, 2016.

[51] Jannick P Rolland and Henry Fuchs. Optical versus video see-through head-mounted displays in medical visualization. *Presence: Teleoperators and Virtual Environments*, 9(3):287–309, 2000.

[52] George D Stetten and Vikram S Chib. Overlaying ultrasonographic images on direct vision. *Journal of Ultrasound in Medicine*, 20(3):235–240, 2001.

[53] Kate A Gavaghan, Matthias Peterhans, Thiago Oliveira-Santos, and Stefan Weber. A portable image overlay projection device for computer-aided open liver surgery. *IEEE Transactions on Biomedical Engineering*, 58(6):1855–1864, 2011.

Chapter 2

Ultrasound Guidance for Beating Heart Cardiac Surgery

This chapter includes material adapted from:

A. Jonathan McLeod, Maria E. Currie, John T. Moore, Daniel Bainbridge, Bob B. Kiaii, Michael WA Chu, and Terry M. Peters. Phantom study of an ultrasound guidance system for transcatheter aortic valve implantation. *Computerized Medical Imaging and Graphics* 50: 24-30, 2016.

A. Jonathan McLeod, John T. Moore, and Terry M. Peters, Beating heart mitral valve repair with integrated ultrasound imaging. In *Proc. SPIE* 9415: 941504-1-8, 2015.

2.1 Introduction

Off-pump, beating heart therapies are quickly becoming standard of care for patients previously deemed inoperable [1]. Since the first human transcatheter aortic valve implantation

27

(TAVI) was performed in 2002 [2] over 200,000 TAVI procedures have been performed worldwide to treat severe aortic stenosis [3]. In this procedure a catheter, equipped to deploy an expanding prosthetic valve, is navigated to the aortic annulus where the prosthesis is deployed inside the native aortic valve (AV). Originally, TAVI's use was restricted to high-risk patients ineligible for conventional surgery where the risks of this relatively new procedure were justified as there was no established safe and effective treatment available [4]. However, as more evidence of TAVI's effectiveness and safety emerges, its use is expanding to intermediate risk patients for whom it can offer a less invasive alternative with shorter hospital stays than conventional surgery [5]. Given the recent success of minimally invasive aortic valve therapy, attention is turning to the mitral valve (MV) with a plethora of valve repair and replacement devices now in clinic or under development. One of the most prevalent is the MitraClip device, which performs edge-to-edge repair through a catheter deployed clip to treat mitral regurgitation and has been used in over 35,000 patients [6]. Several other valve repair devices have recently made the transition to human trials, including the NeoChord MV repair device, which received CE mark of approval in 2012 and has been used in over 500 patients [7]. In addition, transcatheter mitral valve replacement has the potential to treat a wider range of mitral valve disease anatomy than possible through minimally invasive repair. Several commercial systems for transcatheter mitral valve replacement have been developed and used in humans with preliminary results on 5 to 30 patients being reported [8].

Both minimally invasive AV and MV procedures rely extensively on intraoperative imaging through fluoroscopy and transesophogeal echocardiography (TEE).

1. **Navigation:** the surgical tools must be navigated from their entry point into the body to the region of interest. Most transcatheter valve repairs and replacements

are performed using either a transapical or transfemoral approach. Intraoperative imaging is limited by the poor tool visualization in ultrasound and the low soft-tissue contrast in fluoroscopy.

2. **Positioning:** Once the surgical tools arrive at the target they must be positioned in the precise location needed for effective treatment. The highly dynamic environment inside the moving heart necessitates intraoperative imaging to provide real-time feedback.

3. **Therapy:** Finally, the therapeutic aspect of the surgery must be accomplished. The minimally invasive tools used in beating heart surgery are designed to accomplish this step as mechanically as possible. For instance, with the NeoChord device a harpoon shaped needle is used to pull the suture through the valve leaflet while in TAVI procedures the prosthetic valves are either deployed by inflating a balloon or are self-expanding. Intraoperative imaging is used to monitor final deployment of the device and confirm valve function.

Much of the effort in improving image guidance for intra-cardiac surgery has focused on the navigation phase of the procedures. Linte et al. [9] developed an augmented reality (AR) guidance system that displayed magnetically tracked surgical tools and intraoperative ultrasound relative to 3D models of the heart derived from preoperative images. These models could include dynamic surface models played as a cine loop and synchronized with intraoperative EKG readings. Registration between the preoperative models and the intraoperative environment can be accomplished through aligning both the mitral and aortic valve annuli [10]. Building on this work, a mitral valve repair guidance system proposed by Moore et al. [11] displayed only the valve annuli without any preoperative data. This

greatly simplified clinical work flow and, in animal studies, was found to significantly reduce the time, path length and potential for injury when navigating to the mitral valve. However, this guidance system was limited to the navigation task and, once the mitral valve was reached, it was not used any further. This chapter discusses two procedures where we develop image guidance to aid in positioning and present preliminary results. In Section 2.2, we develop an AR guidance system for TAVI. Since the catheter is advanced along a guide wire, deploying the TAVI prosthesis is largely a 1D positioning problem where the surgeon must choose the appropriate depth to avoid blocking the coronary ostia or impeding mitral valve function. Furthermore, rapid ventricular pacing keeps the aortic valve relatively static while the valve prosthesis is positioned and deployed. We propose an AR guidance system that lets the surgeon choose the deployment depth based on intraoperative ultrasound and then guides the catheter to the ideal position. In addition, we develop a specialized delivery tool that integrates intracardiac echocardiography (ICE) imaging directly into the tool itself, to visualize the stent and pertinent anatomy and to monitor deployment. In Section 2.3, we similarly develop a modified NeoChord DS-1000 device that includes integrated ICE. Grasping the mitral valve leaflets is a more complex task than expanding the TAVI stent. The addition of integrated ICE imaging enables the AR guidance to extend into the positioning phase of the procedure by providing high-quality onsite ultrasound that is incorporated into the AR environment.

2.2   Transcatheter Aortic Valve Implantation

TAVI procedures rely primarily on single-plane fluoroscopy for guidance with which only gross structures are visible [12]. In addition, the contrast agents injected into the aortic root during fluoroscopic guidance are nephrotoxic and can increase a patients risk of acute

kidney injury[13, 14, 15, 16]. This is a major concern as many TAVI patients have un-derlying renal dysfunction and are more vulnerable to acute kidney injury. Furthermore, fluoroscopic imaging exposes both the patient and physicians to ionizing radiation. While the radiation dose for a single procedure is low, the cumulative radiation exposure of health care professionals at centers with a high throughput of TAVI is a concern [17]. There have been several proposed alternatives to single plane fluoroscopy that aim to improve stent placement and reduce or eliminate the use of nephrotoxic contrast and ionizing radiation, including rotational angiography, magnetic resonance imaging (MRI), and transesophageal echocardiograph (TEE) guidance. In rotational angiography, an intraoperative cone beam computer tomography (CT) volume is acquired by rotating a C-arm around the patient. This volume can be used to generate models of the aortic root which are overlaid on the fluoroscopy images to provide more anatomical context and can also be used to select the ideal fluoroscopy imaging plane [18]. This technique requires contrast and ionizing radia-tion to acquire the intraoperative CT volume and for fluoroscopy throughout the procedure. Alternatively, intraoperative magnetic resonance imaging has been used to guide placement of the valve stent, resulting in successful implantation in animal studies [19]. Although this technique eliminates contrast and radiation exposure, intraoperative MRI is expensive and not widely available [20].

Intraoperative ultrasound provides a more attractive modality for image guidance since it does not require nephrotoxic contrast agents or ionizing radiation in addition to being inexpensive and easily integrated into surgical workflow. TEE is frequently used during TAVI procedures for assessing valve function after the stent is deployed. Intraoperative guidance using only TEE [21] and TEE with fluoroscopy (without contrast agents)[22] has been previously reported. However, TEE does not provide satisfactory imaging of the

catheter or surrounding tissue due to the highly reflective surface of the catheter and result-
ing shadowing artifacts. For this reason, TEE has been proposed as a bridging modality
allowing preoperative models to be registered into the intraoperative environment. Lang
et al. [23], proposed using TEE to register preoperative CT models to fluoroscopy to im-
prove image guidance without requiring rotational angiography. Luo et al. [17] proposed
a system using magnetic tracking of the TEE and catheter to eliminate the need for flu-
oroscopy entirely. In this system, a preoperative model of the aortic root was registered
to the tracked ultrasound. The tracked catheter could then be visualized in relation to the
aortic model so that the stent could be deployed at the desired depth. One challenge of
these techniques is that the registration between ultrasound and preoperative CT is diffi-
cult, resulting in a target registration error of 5.9±3.2 mm and 3.3±1.6 mm respectively. In
addition, both these works used a manual segmentation of the aorta from preoperative CT
which is time consuming and difficult to integrate into clinical workflow. Previous work
with mitral valve repair has found that simply defining the valve annuli from tracked TEE is
sufficient for image guidance and eliminates the need for complex preoperative models and
registrations with associated errors [11]. Here, a simplified guidance system using TEE and
magnetic tracking is developed and validated against fluoroscopic guidance in a phantom
environment.

2.2.1   Methods

Augmented Reality

The proposed guidance system consists of a augmented reality environment displaying real-
time ultrasound along with the location of the tracked valve stent and the intraoperatively
defined anatomy. In order to display the TEE images and catheter in a common frame of
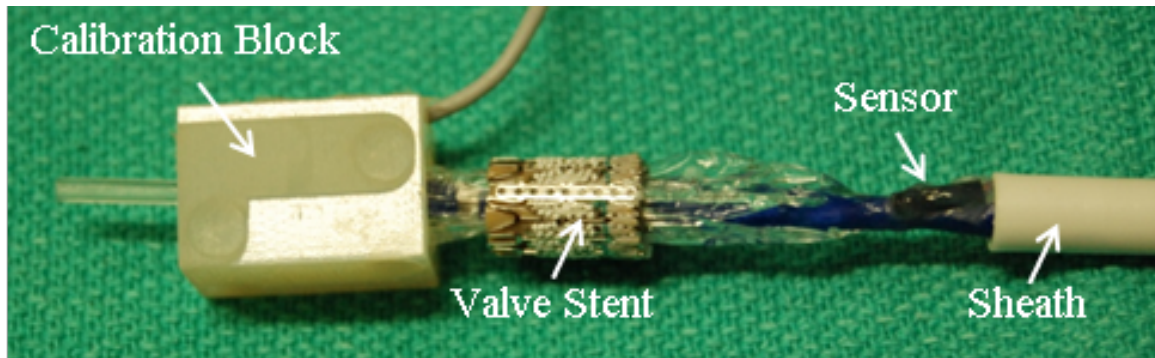
Figure 2.1: Magnetically tracked catheter with crimped valve and calibration block. The sensor was affixed to the catheter tip just below the balloon as shown. The white outer sheath can be moved up to completely cover the sensor. A ledge inside the calibration block allows the crimped valve to be held in a specific configuration so that the transformation between the catheter sensor and the prosthetic valve can be defined.

reference, both of these tools were magnetically tracked using the Aurora tabletop tracking system (NDI, Waterloo, Ontario). A 6 degree of freedom (DOF) magnetic tracking sensor was affixed to the Ascendra TAVI catheter (Edwards Life Sciences, Irvine, California) just below the balloon with the cable running inside the outer sheath of the catheter. The iE33 ultrasound system with an X7-2t TEE probe (Philips Healthcare, Andover, Massachusetts) was used and is capable of providing 2D, biplane and live 3D imaging. A second 6 DOF sensor was integrated into a custom-made cap that attaches to the TEE probe and calibrated using a Z-bar phantom. Once the valve was crimped onto the catheter, it was inserted it into a tracked calibration block designed to hold the catheter shaft and valve in a precise configuration with the leading edge of the valve resting against a ledge inside the calibration block (Figure 2.1). This calibration procedure finds the spatial transform between the magnetic sensor and the crimped valve and catheter shaft.

The aortic valve can ve defined intraoperatively in the augmented reality environment by selecting points on the aortic valve in the tracked biplane ultrasound. These points, along
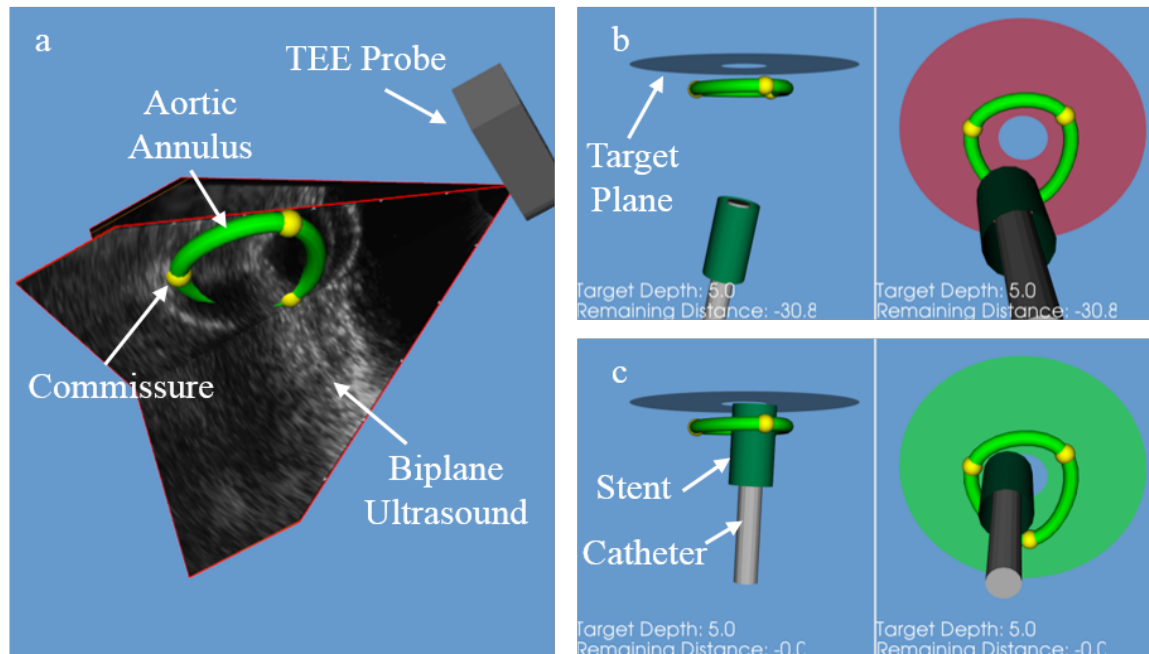
Figure 2.2: The aortic valve is defined on the tracked biplane ultrasound (a). The tracked catheter with the calibrated stent, the user defined aortic valve and the targeting plane are displayed in the augmented reality guidance system (b). A split screen view presents two camera angles appropriate for centering and advancing it to the correct depth. The targeting plane changes from red to green when the stent reaches the desired deployment depth (c).

with a tubular spline outlining the valve, are displayed in the augmented reality guidance system and a targeting plane is then created at the ideal deployment depth. The remaining distance from the catheter to this plane is displayed numerically and the targeting plane changes color to indicate when the ideal deployment depth is reached (Figure 2.2). When visible in the echo image, other pertinent anatomy including the coronary ostia can also be displayed in the guidance system.

Delivery Tool with Integrated ICE

One limitation of relying on mixed reality guidance is the lack of adequate imaging during deployment. In conventional procedures, live fluoroscopy video provides feedback to mon-
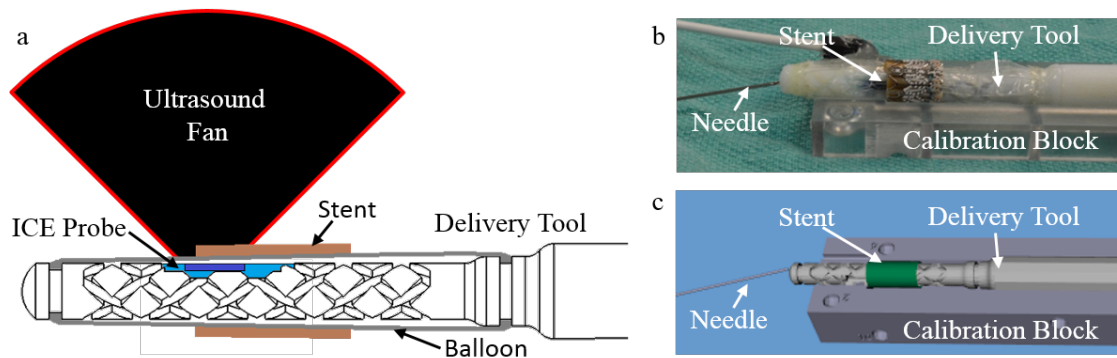
Figure 2.3: A diagram of the delivery tool with ICE (a), a photograph of the calibration procedure (b) and a screenshot of the augmented reality models (c) are shown.

itor deployment and fine tune the position of the stent as the balloon is inflated. The image quality of TEE is very poor once the catheter and stent have entered the aortic valve, limiting its usefulness at this stage of the procedure. To overcome these issues a custom-made stent delivery tool with integrated ultrasound imaging was created for transapical procedures. The delivery tool contains a channel through which an intracardiac echocardiography probe can be inserted. The ICE probe acquires images through an acoustic window in the shaft of the tool. The prosthetic valve is positioned so that it partially covers the ICE transducer. This ensures that the leading edge of the stent will be visible in the ultrasound image. Calibration is performed using a similar method to the one used for the tracked catheter. The delivery tool is placed inside a calibration block with the leading edge of the valve resting against a ledge in the block. However, this calibration block is half open to accommodate the delivery tool and a tracked needle is used to locate the tip of the delivery tool so that both the tool and the valve may be tracked and visualized in the guidance system (Figure 2.3).

The tool itself was manufactured through rapid prototyping, using VeroWhite material on an Objet30Pro printer (Stratasys, Eden Prairie, Minnesota), and contained a channel

for an AcuNav10F ICE catheter (Siemens, Erlangen, Germany). The outer diameter of the shaft was 14mm to accommodate the fragility of the rapid prototyping material. In comparison, the TAVI introducer used in conventional transapical procedures is 10mm in diameter and other transapical tools are of similar sizes. For instance, the Neochord (Neochord, Eden Prairie, Minnesota) is a rigid tool being used successfully for mitral valve repair and is approximately 9mm diameter. The diameter of the delivery tool could easily be reduced to under 10mm if machined from stronger material. While the size and rigidity of the tool are unlikely to pose a problem for transapical procedures, it would be very difficult to create a similar system for transfemoral procedures as a small and flexible catheter is required for this approach.

Phantom

The phantom used in this experiment is a modified version of a custom-made system designed to simulate functional mitral and aortic valves. The phantom consists of a left ventricle, atrial reservoir, valve sheet containing mitral and aortic valves, and an actuator system. The ventricle has an apical access port to simulate interventions such as TAVI. In this instance, the phantom was made of a soft silicone (Shore A 30 durometer) while water was used to simulate blood. The inner diameter across the aortic valve was 23mm at the commissures. To facilitate fluoroscopic imaging for this study, the aortic valve annulus was placed approximately 30mm beyond the mitral valve plane, relative to the apical entry point. Experiments were performed in a static model to simulate rapid pacing, but a raised tower was attached beyond the aortic root to increase pressure on the basal side of the valve, allowing realistic simulation of contrast enhancement for fluoroscopy (Figure 2.4).
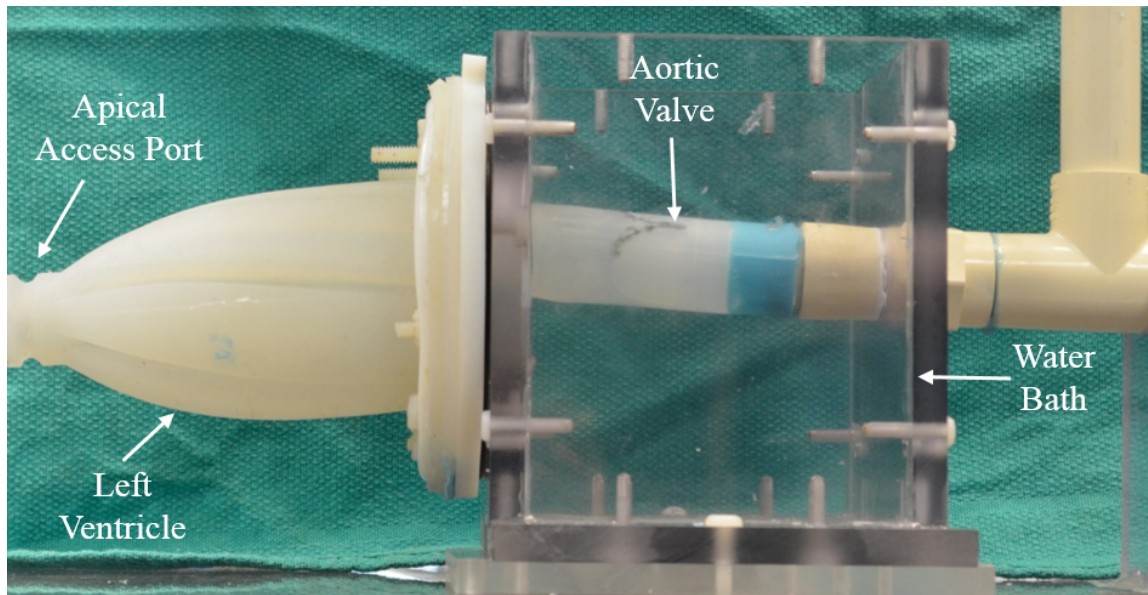
Figure 2.4: The phantom used in this study consists of a silicone left ventricle and aorta. The aorta is contained in a water bath and the outflow tract connects to the reservoir. Note that the distance between the mitral and aortic valves has been exaggerated to facilitate improved imaging away from the edge of the water bath where the ventricle is joined with the silicone valves.
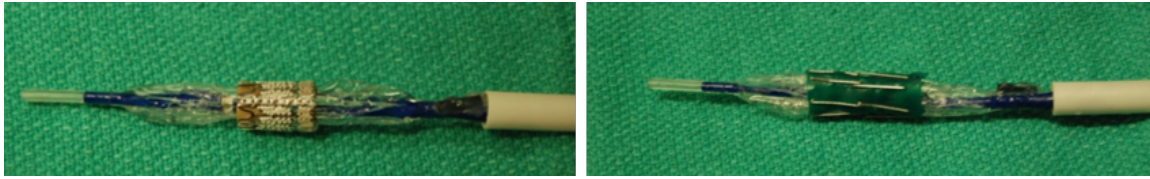
Figure 2.5: The real stent (left) and surrogate stent (right) are shown attached to the delivery catheter.

Surrogate Stent

As the balloon-inflated TAVI valves are single use, a surrogate stent was used for the experiments to allow a larger number of trials to be performed (Figure 2.5). The surrogate stent was made from an elastic material with radiopaque markers simulating the struts of the stent and had an appearance in both fluoroscopy and ultrasound similar to the real valve stent. The surrogate stent could be reused without significant wear and would collapse as the balloon was deflated. For this reason, all measurements were acquired while the balloon was inflated.

Valve Deployment Experiments

The proposed guidance system, both with and without the ICE delivery tool, was compared against fluoroscopic guidance in the phantom model. A cardiac surgery resident deployed the surrogate valve in the phantom 10 times using each of the three guidance methods. After each deployment, a camera jig was positioned over the phantom to photograph the stent inside the aorta from a fixed position. A reference checkerboard was mounted beside the aorta at the same depth as the two commissures visible from the camera's position. Immediately after deployment, a photograph was acquired for retrospective analysis in which the stent struts and the two visible commissures were manually identified. The distance between the commissure plane and the furthest visible stent strut was measured
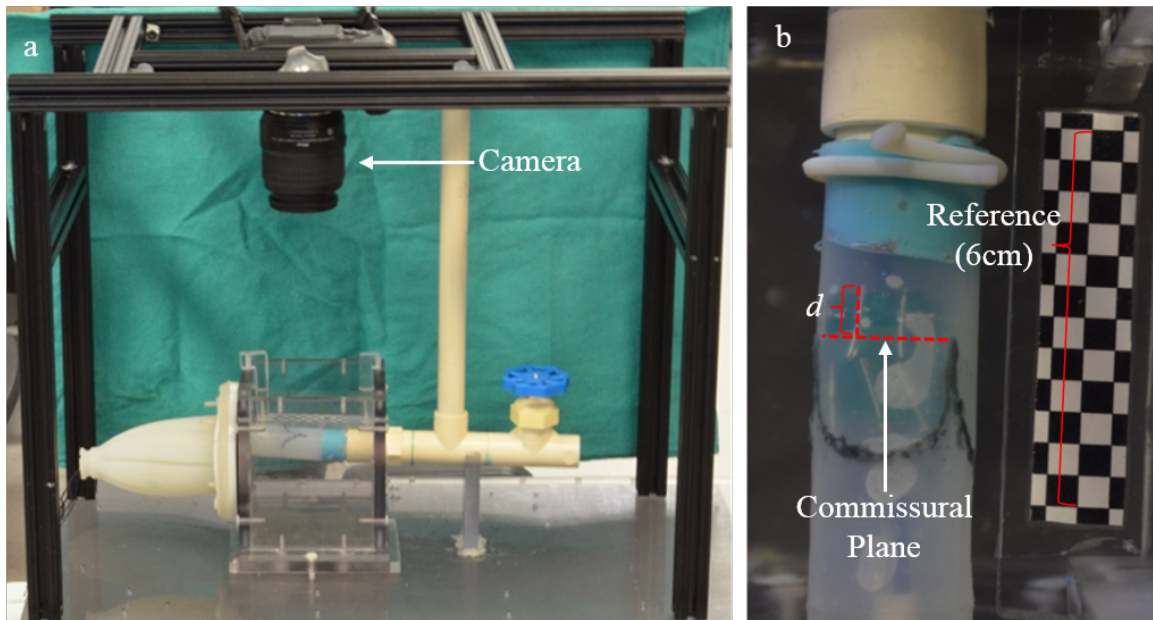
Figure 2.6: Measurements were taken from photographs acquired from the camera jig (left) which holds the camera directly above the aortic valve and perpendicular to the surface of the water bath. The commissures, valve and reference checkerboard were all visible in these photographs (right). The depth of deployment, d, is measured between the commissural plane and furthest visible stent strut as illustrated.

using the checkerboard reference for scale (Figure 2.6).

Fluoroscopy

The first experiment simulated conventional contrast enhanced fluoroscopic guidance. First, a guidewire was inserted through the apex of the phantom and passed through the ventricle and aortic valve, terminating in the aortic reservoir. A pigtail catheter was deployed through the aortic reservoir and rested above one of the aortic leaflets. In a real procedure, the pigtail catheter is used to deliver contrast and serves as a radiopaque marker identifying the aortic valve. The valve delivery catheter was inserted onto the guidewire and into the left ventricle of the phantom. Prior to each trial, contrast was injected into the aortic root

so that the valve, including commissures and nadir, were visible in the fluoroscopic image. The stent was positioned using fluoroscopic video so that it appeared that half of the stent lay on either side of the valve (Figure 2.7). Before deployment, the pigtail catheter was withdrawn to ensure that it would not become caged by the stent. As the current standard of care is to deploy the valve using the fluoroscopy images qualitatively without any quantitative target, it is difficult to give an exact deployment error or location for ideal deployment. In this experiment, the user was instructed to strive to achieve consistent deployment in all 10 trials. The variability of valve deployment depths give an estimate of the minimum error achieved in fluoroscopic guidance.

Augmented Reality

In the second experiment, valve deployment took place using the proposed guidance system. As in the fluoroscopy study, a guidewire was passed through the aortic valve. The surrogate stent was placed on the modified valve delivery catheter and the position of the stent was determined using the calibration block. After the delivery catheter was inserted into the left ventricle, all three aortic commissures were identified in the ultrasound image. A targeting plane was created 5mm beyond the commissural plane, and the valve was deployed at this location. The aortic valve and stent calibration were repeated for each trial so that variability in these steps was included in the stent deployment. In addition to the photographic measurements, the deployment depth reported by the guidance system was also recorded.

The choice of features and deployment depth were arbitrary and the valve nadir or any identifiable points on the aortic valve could be used instead of the commissures so long as the deployment depth is adjusted accordingly. In our case the commissures were chosen
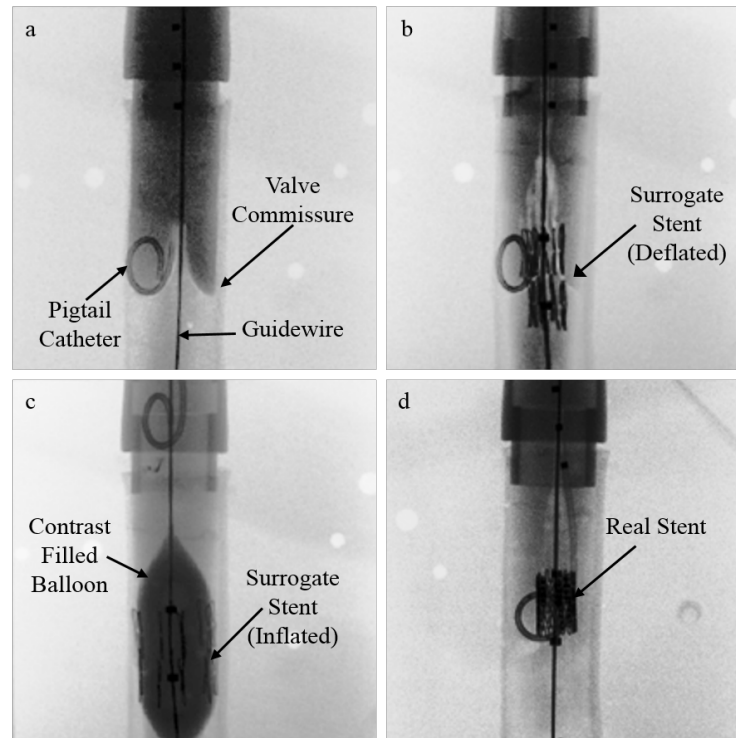
Figure 2.7: Fluoroscopic images during all phases of deployment are shown. First, contrast is injected into the aortic reservoir so the aortic valve can be seen (a). The pigtail catheter resting above one of the valve leaflets serves as a valuable landmark throughout the procedure. Next, the catheter is advanced to the desired position (b) and the balloon inflated (c). The surrogate valve (b) has a similar appearance to the real valve (d) under fluoroscopic guidance.

as they were easily identified and were the features closest to where the leading edge of the stent should be deployed. The deployment depth of 5mm was chosen to ensure the leading edge of the valve was deployed beyond the commissures and clear photographic measurements could be acquired. In practice, the deployment depth would depend on the patient's anatomy and the profile of the prosthetic valve to ensure the coronary ostia are not obstructed by the stent.

Augmented Reality with ICE

In the final experiment, the specialized delivery tool was used instead of the traditional catheter. As when using the tracked catheter in the previous experiment, the position of the stent on the device was determined using a specialized calibration block. The same image guidance system was used to guide the delivery tool into the aortic valve and in initial positioning of the stent. As the tool was advanced, both the stent and aortic valve leaflets were visible on the live ICE video (Figure 2.8). The stent was deployed such that the tip of the leaflet was approximately 5mm behind the leading edge of the stent as seen in the ICE images.
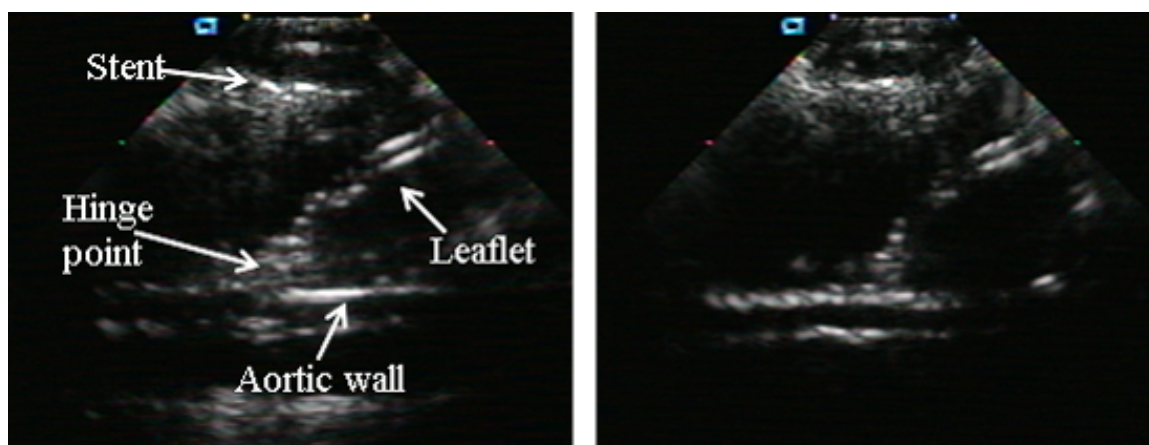
Figure 2.8: ICE imaging acquired with the delivery tool. The stent along with the aorta including leaflets are visible. Here the hinge point of the aortic valve is clearly visible in the center of the image. The real stent (left) and surrogate stent (right) result in similar image quality.

2.2.2 Results

The results for all three guidance systems are shown in Table 2.1. The fluoroscopy guidance system achieved a deployment depth of 6.3±3.4mm (mean±standard deviation). The guidance system resulted in a deployment depth of 7.0±2.9 mm as recorded by photographic measurements while the deployment depth report by the guidance system itself was 5.03±0.03mm. Finally, when the ICE delivery tool was used a deployment depth of 5.7mm±2.3mm was achieved. The deployment depth for all trials is reported in Table 1 and box plots summarizing the distribution are shown in Figure 2.9.

Table 2.1: Deployment depths using the three guidance systems (target depth = 5mm).

Trial	1	2	3	4	5	6	7	8	9	10
Fluoro(mm)	6.95	1.29	0.62	5.99	9.28	11.07	7.31	9.40	5.96	4.94
AR(mm)	9.83	7.84	2.97	7.70	6.76	6.59	7.92	9.95	9.23	0.84
AR+ICE(mm)	2.46	0.98	5.76	7.94	7.47	4.91	7.86	7.77	6.04	5.34
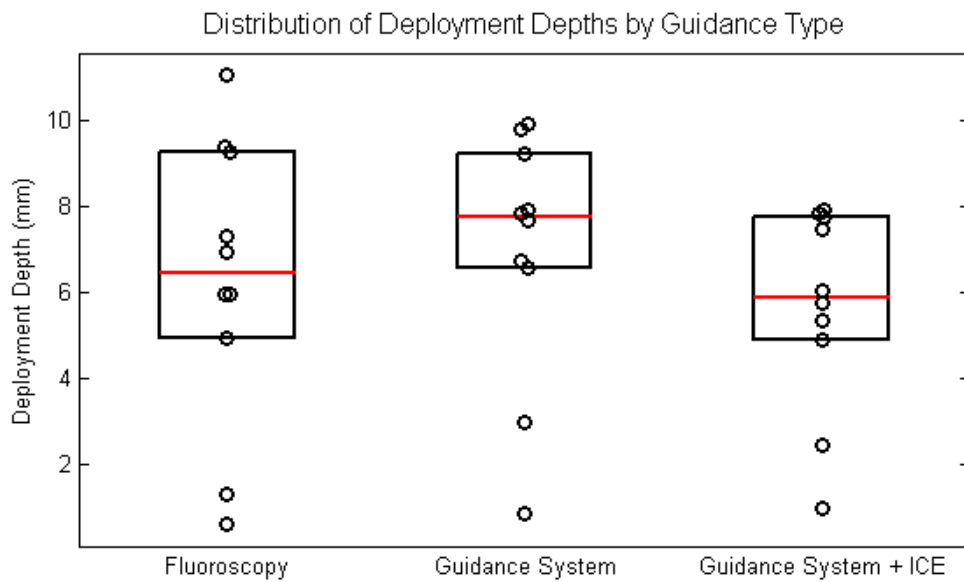
Figure 2.9: Box plots showing the distribution of deployment depths for the different guidance systems. Each box includes the interquartile range in deployment depth with the median indicated by the central horizontal line. Individual deployments are plotted with the ∘ symbol.

2.2.3 Discussion

Experimental Results

The root mean squared error (RMSE) of the deployment depth was 3.4mm when using the tracked catheter and 2.3mm when using the customized delivery tool with integrated ICE imaging. In comparison Luo et al. [17] achieved an RMSE of 3.3mm in transfemoral procedures on a porcine model using a magnetically tracked catheter. Our study also included a comparison with contrast enhanced fluoroscopic guidance. In clinical practice, the stent would need to be deployed at a depth sufficiently low to prevent obstruction of the coronary ostia but still far enough into the aorta to prevent migration or obstruction of the mitral valve. The fluoroscopic images are used to ensure these conditions are met before valve deployment. The qualitative nature of this type of image guidance makes it difficult to assign a desired target depth, and even if one were chosen, it would be difficult to accurately achieve this deployment depth without more elaborate intraoperative analysis of the fluoroscopic images. Instead, we only evaluate the precision of deployment in fluoroscopic guidance where we achieved a standard deviation in deployment depth of 3.4mm. In comparison standard deviation in AR and AR+ICE experiments were 3.0mm and 2.4mm respectively. However, the lower variance in deployment depth observed in both the augmented reality methods were not statistically significant when compared against fluoroscopy under an F-test for equal variance ($p > 0.05$). It is also worth noting that the RMSE in the augmented reality guidance systems, which incorporates both the bias (mean) and precision (standard deviation) added in quadrature, was as good or smaller (3.4mm for the tracked catheter and 2.3mm for the ICE delivery tool). This suggests that a similar level of accuracy can be achieved with these guidance systems even when discounting the possibility of a consistent bias in identifying the site for valve deployment in fluoroscopy.

In this study the ICE delivery tool appeared especially promising in producing low deployment errors. It is likely that the majority of the error in the image guidance system comes from defining the aortic annulus and the magnetic tracking itself. This is supported by the near perfect deployment depth reported by the magnetic tracking of 5.03±0.03. Integrating the ICE probe into the delivery tool allows the user to correct for these errors based on live ultrasound where both the stent and aortic valve are visible. It is interesting to note that all but the first two trials with the ICE delivery were within a 3mm range from 4.9 to 7.9mm. This experiment was the first exposure the cardiac surgery resident had to the new delivery tool and the ICE images were difficult to interpret leading to a substantial learning effect, which could explain why the first two trials were so far outside this range as seen in Figure 2.9.

Surgical Workflow

The proposed guidance system is easily integrated into the operating room. The NDI Aurora tabletop generator fits on top of the operating table, requiring less space than alternative systems, and was specifically designed to work in the presence of ferrous and conducting objects so that conventional surgical tools may be used. The tracking sensors attached to the TEE probe and stent delivery devices do not impede workflow in the operating room. The delivery tool with integrated ICE requires an additional ultrasound machine to be brought into the operating room; nevertheless, this system has a smaller footprint and lower costs than other alternatives relying on intraoperative MRI or rotational angiography.

Besides the additional ultrasound and magnetic tracking equipment required, the aortic valve and other pertinent anatomy must be defined intraoperatively so they may be displayed in the guidance system. In balloon deployed TAVI procedures, an ideal opportunity

to define the valve is presented during rapid pacing. Rapid pacing is performed twice during these procedures: first, to test the leads prior to advancing the catheter into the aortic valve and then again to arrest cardiac motion as the stent is deployed. The aortic valve may be defined during the first rapid pacing without disrupting surgical workflow. This also ensures that, when the valve is defined from tracked biplane ultrasound, the heart is relatively stationary and in the same condition as during final deployment. The real time tracked ultrasound is displayed in the mixed reality environment. If the aortic valve or any other pertinent features have moved, they can be redefined before proceeding.

2.3   Mitral Valve Repair

In the NeoChord procedure, AR has been shown to improve safety, reduce navigation task time, and greatly reduce the learning curve for the process of navigating the surgical device to its target region of the MV coaptation region[11]. However, the substantial motion of the MV leaflets (on the order of 15mm within the cardiac cycle) makes it essential to rely heavily on real time image data for completing the process of grasping a leaflet (the positioning task). Our previous results with TAVI suggest that having ultrasound imaging built into the intracardiac therapy device can substantially improve overall safety and accuracy of the procedure. This section summarizes our first attempts at implementing on-site ultrasound support for mitral valve grasping and therapy delivery. The on-site ultrasound can be used to ensure the jaws of the NeoChord device will fully engage the mitral valve leaflet and also to achieve even spacing of the implanted neochordae along the leaflet (typically 2-7 neochordae are implanted per procedure). These tasks are important for the success of the procedure but are very difficult using TEE imaging alone.

2.3.1   Methods

Device Modification

Using rapid prototyping technologies (Objet30 Pro polyjet printer, Stratasys Inc.), the Neo-Chord DS-1000 MV repair device (NeoChord Inc.) was modified to incorporate a 10-French intra-cardiac echocardiography (ICE) transducer (Siemens Sequoia ICE console). The ICE transducer was positioned behind the jaws of the NeoChord device with the imaging plane running through the middle of the jaws. The bottom jaw of the NeoChord had a narrow window cut through its center which allowed for imaging even when the jaws were closed (Figure 2.10). This setup allowed for nearly uninterrupted imaging of tissue in front of the NeoChord device as well any tissue between the jaws when they were opened. The modified tool included two tracking sensors allowing it to be magnetically tracked and incorporated into an augmented reality guidance system.[11]

Ultrasound Imaging

Conventional TEE guidance for this procedure relies on both 2D and 3D imaging. The current practice in human cases is to use 2D imaging during the positioning phase of the procedure when the NeoChord device is inserted into the mitral annulus. Once the tool crosses the mitral valve plane, the TEE is switched to 3D mode for leaflet capture and neocordae deployment [24, 25]. The 3D TEE imaging can visualize the Neochord device protruding through the mitral leaflets (Figure 2.11a). However, determining bit depth from the 3D images is difficult and the surgeon needs to rely on the four fiber optic sensors to confirm the leaflet has been captured.

    With the modified tool, the ICE probe provides high resolution ultrasound imaging from a fixed position relative to the jaws of the NeoChord device. The mitral valve leaflet
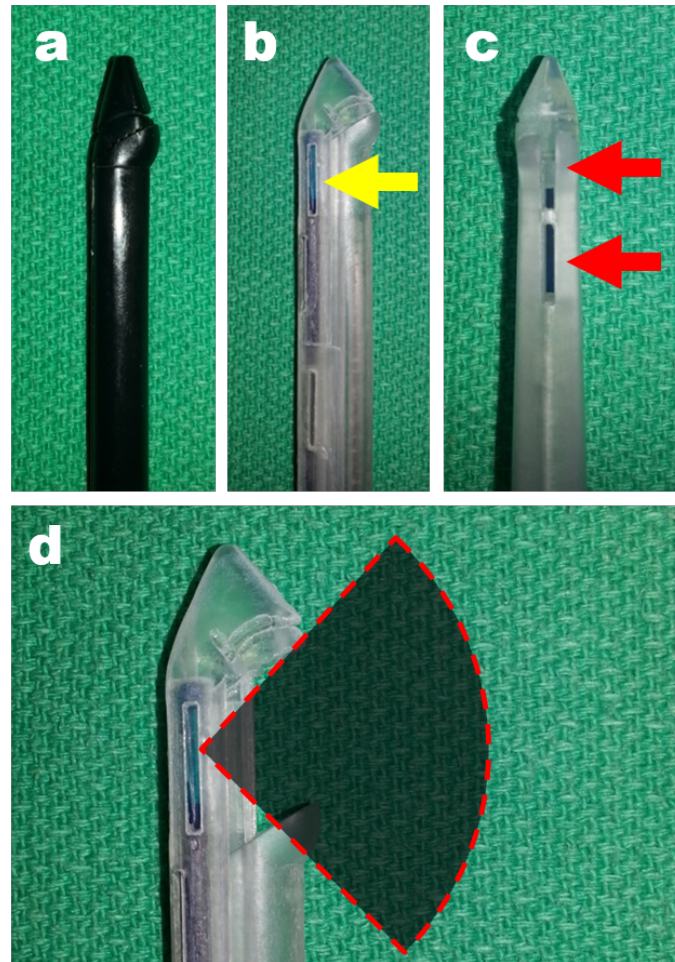
Figure 2.10: The original NeoChord tool (a) was modified to integrate an ICE imaging catheter (b,c,d). The yellow arrow in (b) shows the position of the ICE transducer inside the NeoChord tool and the red arrows in (c) show the position of the window cut into the bottom jaw to allow for ICE imaging even when the jaws are closed. The position of the ultrasound fan is shown in relation to the open jaws of the Neochord in (d).

can be imaged as it enters the jaws of the NeoChord so that the surgeon can make sure full engagement of the leaflet will be achieved before closing the jaws (Figure 2.11b). Previously deployed neochordae can also be identified from the ICE images allowing the NeoChord device to be returned to the location of a previous deployment, which appears as a hyperechogenicity on the valve leaflet due to the strong reflections from the implant.
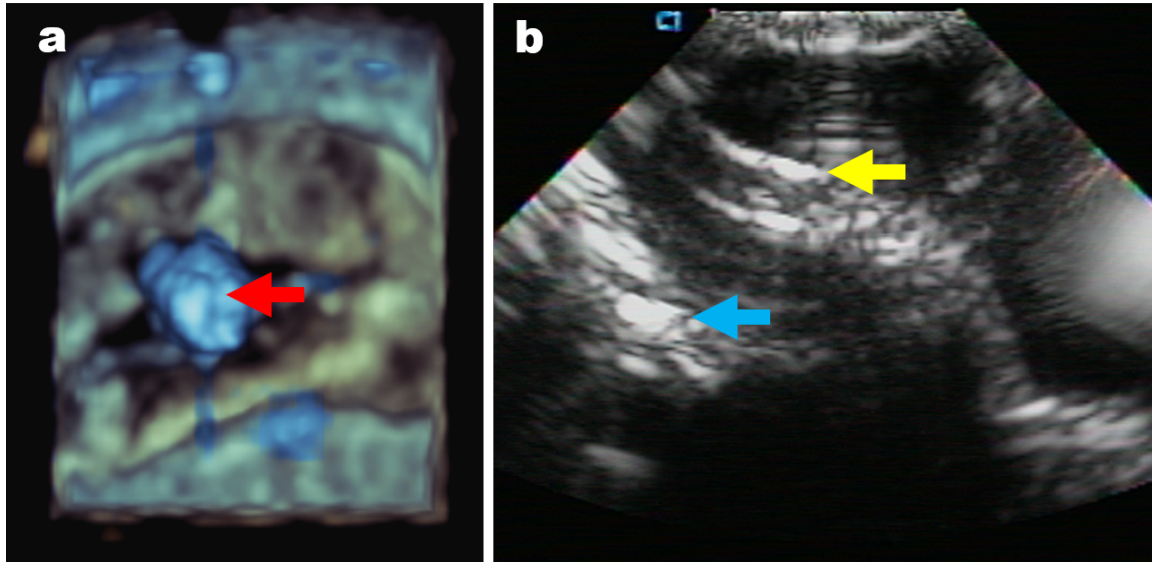
Figure 2.11: 3D TEE imaging shows the NeoChord device (red arrow) inserted through the mitral valve during leaflet capture (a). The integrated ICE imaging shows the mitral leaflet (yellow arrow) in relation to the bottom jaw of the neochord (blue arrow) to ensure a full bite is achieved (b).

Augmented Reality

The modified NeoChord device was integrated into the AR environment previously described by Moore et al. [11]. The virtual representation of the modified NeoChord included the ICE fan so the live images could be viewed in relation to the NeoChord device and previously identified anatomy (Figure 2.12). Within the AR environment, the user could identify points on the mitral annulus from the ultrasound images. A spline connecting these points would be displayed to represent the mitral annulus in the AR environment. In addition, previously deployed neochordae could be identified on the ICE images and a spherical marker was placed in the AR environment to denote their location. Although the AR environment was originally intended for navigation only the context it provides was helpful in interpreting the ICE images during positioning and leaflet capture.
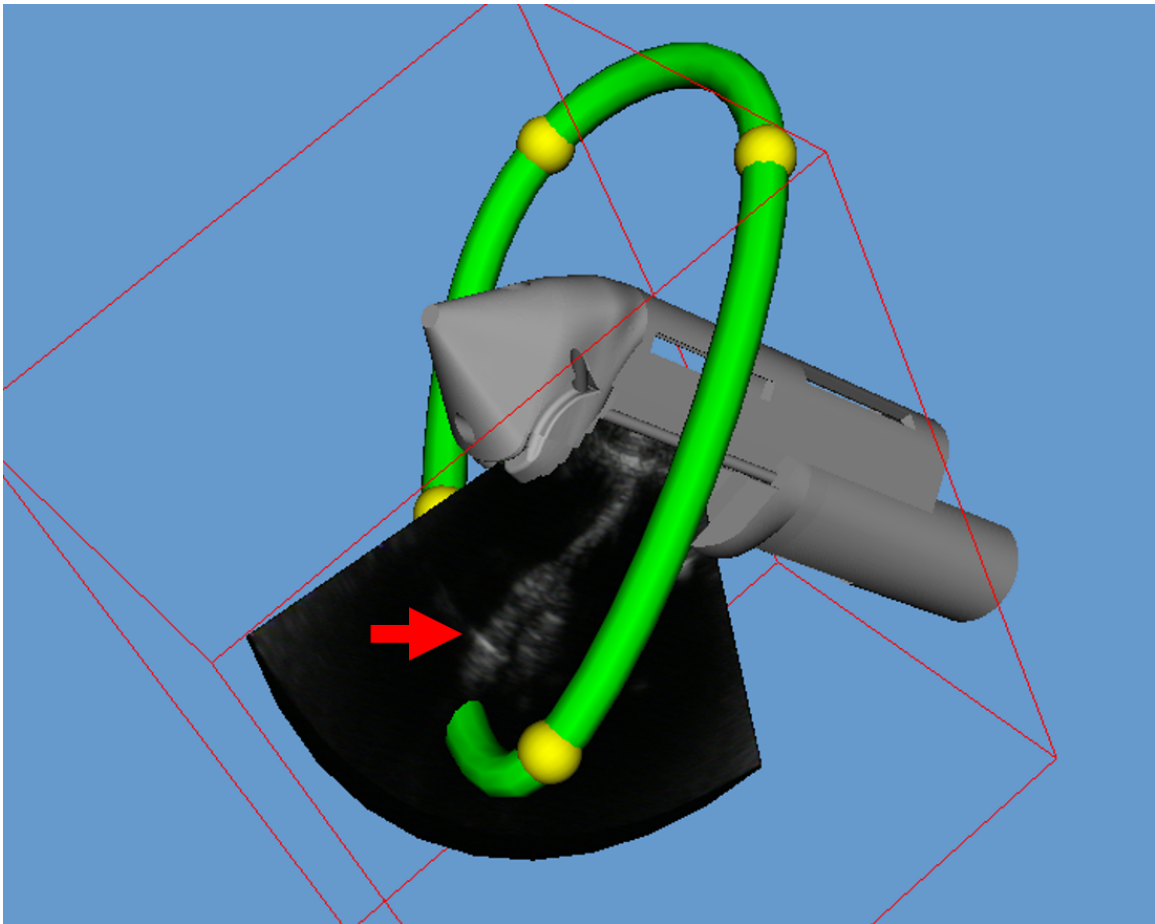
Figure 2.12: The AR environment includes a virtual model of the NeoChord device and ICE fan as well as pertinent anatomy identified from the ultrasound images. The mitral annulus is represented by the green ring connecting four yellow spheres which were defined by the user from ultrasound. The mitral leaflet is visible on the ICE image and can be seen extending from the mitral annulus to the jaws of the NeoChord (red arrow).

Phantom Environment

Neochordae implantation was tested in a dynamic cardiac phantom [26]. The phantom consisted of a silicone left ventricle, mitral valve flange and atrial reservoir (Figure 3.6a). The left ventricle was actuated using six pneumatic cylinders at 60bpm to simulate the contraction of the left ventricle. A custom built valve flange was used in which the mitral leaflets

were made from a fabric embedded in the silicone (Figure 3.6b). The leaflets had a realistic appearance under ultrasound and were strong enough to undergo multiple neochordae deployments without ripping.
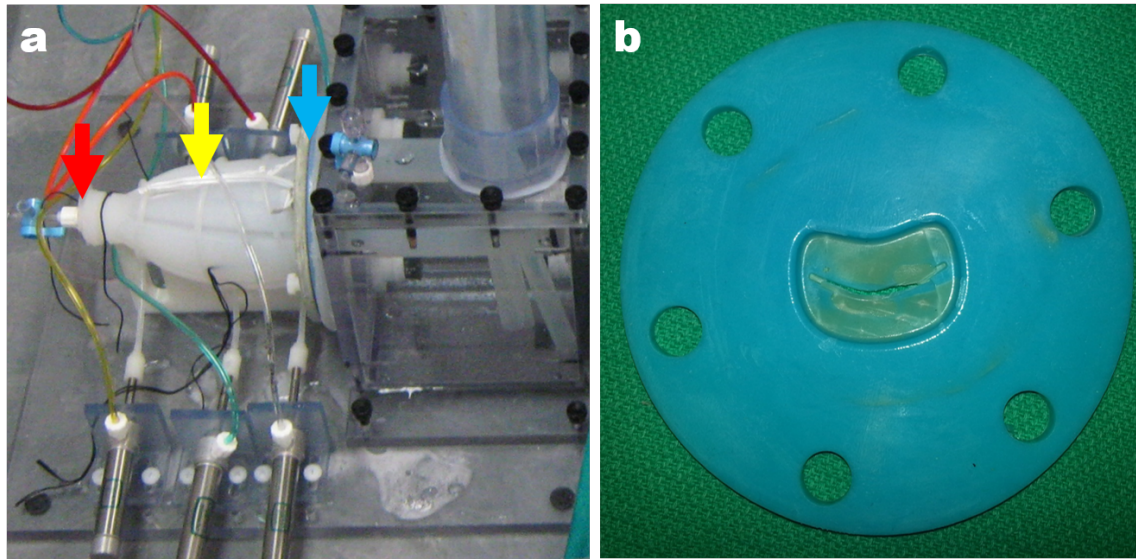
Figure 2.13: The phantom consisted of a left ventricle, mitral valve flange and an atrial reservoir (a). The NeoChord is inserted through an access port (red arrow) at the apex of the ventricle (yellow arrow). A flange containing the mitral valve (blue arrow) separated the left ventricle from the atrial reservoir. This flange (b) was constructed out of silicone with embedded fabric leaflets.

Neochordae Implantation

Simulated valve repair procedures were performed in the phantom to compare the modified tool with integrated ICE to an unmodified NeoChord DS-1000. In human procedures, 2-7 neochordae are implanted as needed until valve function is improved, each implantation being accomplished in three phases. The navigation phase involves moving the NeoChord tool from the apex of the ventricle to the mitral annulus. This phase is typically performed under 2D TEE guidance. For the positioning phase, the TEE is switched to 3D, the valve

leaflet is grasped by the NeoChord device and the implant is deployed. In the third phase, the surgeon adjusts the tension of the implanted neochord while monitoring valve function with 2D and 3D TEE imaging. Once satisfied, the free end of the neochord implant is secured to the apex of the left ventricle. Our experiment is only concerned with the positioning phase where the leaflet is grasped, as this is the stage at which we expect the ICE imaging to be most useful. For the experiment the user attempted to deploy a series of neochordae evenly spaced along the posterior mitral leaflet while achieving full engagement. Neochordae should only be deployed when the leaflet is fully captured by the jaws of the NeoChord device resulting in a bite depth of approximately 4mm [27]. A smaller bite depth could result in dehiscence when the tension in the neochord implant is adjusted. Additionally, we wished to see if the ICE images could be used to better target the deployment of multiple neochordae as the location of previous deployments are easily identified from the ICE images. Once the first implant was deployed, the user continued to deploy neochordae along the posterior leaflet (aiming to achieve a total of 3-5 deployments as evenly spaced as possible). After the deployments were complete, the mitral valve flange was removed from the phantom and the bite depths and spacing between the neochordae implants were measured with calipers (Section 2.3.2).

Integrated ICE Guidance

The mitral valve annulus was defined in the AR environment using four manually identified points. The modified delivery tool was navigated through the mitral valve. Using the 3D TEE image, the Neochord delivery tool was positioned at the desired location along the posterior leaflet and ICE imaging was used to assist in leaflet capture. The NeoChord device was maneuvered so the mitral leaflet rested on the bottom jaw of the device with

the tip of the leaflet as close to the back of the device as possible and the neochord implant was deployed. To help achieve an even spacing between implants, previously deployed neochordae were identified in the ICE images. Spherical markers were created in the AR environment to mark their location so the NeoChord device could be positioned relative to previous deployments.

TEE Only Guidance

When using the unmodified NeoChord, 3D TEE images were used for final positioning and leaflet capture. In addition to the TEE images, the unmodified tool had four optical sensors on the bottom jaw of the NeoChord that were connected fiber-optically to four display lights on a handheld monitoring unit. When the leaflet came into contact with the bottom jaw of the NeoChord, the lights on the handheld monitoring unit would brighten. The upper jaw of the NeoChord was then lowered to grasp the leaflet and the monitoring device was checked again to ensure that all for optical sensors were in contact with the leaflet.

2.3.2   Results

Four neochordae were implanted using the ICE guidance and three were implanted using TEE only. The third neochordae implanted using ICE guidance was poorly placed on the side of the leaflet and so a fourth neochordae was implanted. In addition, there was one failed attempt at deploying a chordae with ICE guidance and two failed attempts at deployment when using TEE only guidance. These failed attempts could have been caused by missing the leaflet entirely or having it slip from the jaws of the NeoChord device during leaflet capture. The final position of all of the implanted neochordae is shown in Figure 2.14.
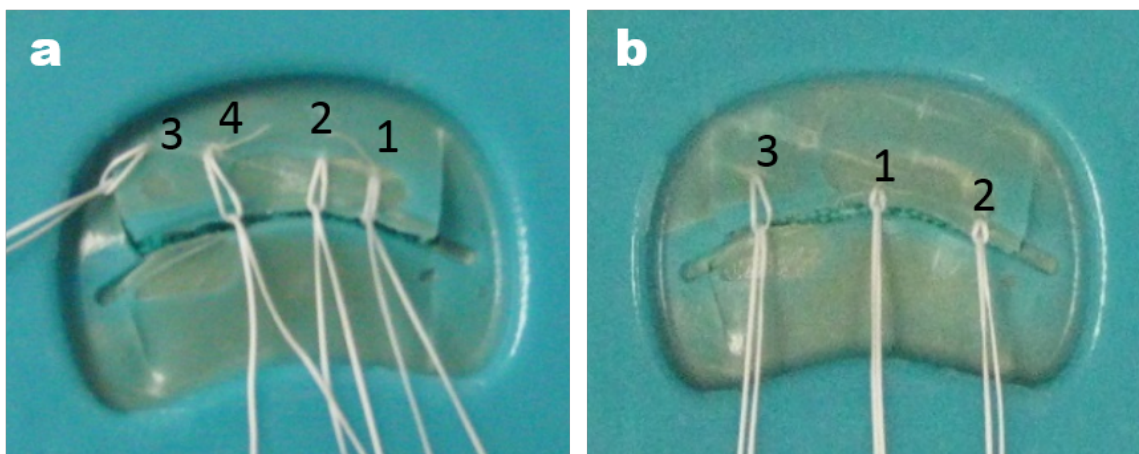
Figure 2.14: The neochordae implanted using ICE (a) and TEE only (b) guidance. Each implant is numbered in the chronological order of deployment.

Bite Depth

The bite depth was measured as the distance from each implant to the nearest point on the leaflet edge. When using ICE guidance the bite depth ranged from 4.4mm to 6.3mm for four implants, indicating full engagement of the leaflet was consistently achieved. When using the TEE only guidance the bite depth ranged from 1.3mm to 4.4mm. Two of the three implants barely engaged the leaflet with a bite depth of less than 2mm. The measured bite depth for all implants is shown in Table 2.2

Table 2.2: Bite depth achieved using integrated ICE and TEE only guidance

	Integrated ICE				TEE Only		
Implant #	1	2	3	4	1	2	3
Depth (mm)	4.4	5.0	5.0	6.3	1.4	1.7	4.4

Implant Spacing

The distance between adjacent neochordae was also measured and reported in Table 2.3. While there are too few measurements to get an accurate estimate of the spacing, the third

implant under ICE guidance was accidentally deployed on the side of the leaflet. This mis-positioning of the NeoChord device could have been prevented by better monitoring of the 3D TEE which was displayed to the user throughout the procedure. After this deployment the user was able to position the tool between the 2nd and 3rd implants, which were easily identified on the ICE images, and use the AR and 3D TEE to deploy a 4th neochord between them.

Table 2.3: Implant spacing achieved using integrated ICE and TEE only guidance

	Integrated ICE			TEE Only	
Implant #	1-2	2-4	3-4	1-2	1-3
Spacing (mm)	4.3	8.7	5.2	8.7	10.0

2.3.3   Discussion

The integrated ICE imaging allowed the mitral valve leaflet to be visualized between the jaws of the NeoChord device and led to consistent bite depths. Achieving a full bite depth is important for preventing dehiscence of the neochordae. This complication is more common in patients with poor tissue quality and may require the implantation of additional neochordae or intraoperative conversion to an alternative surgery [28]. However, achieving proper spacing of the implanted neochordae was difficult. We believe the main reason for this was cognitive load as the user needed to divide attention between the ICE imaging used for leaflet capture and the 3D TEE imaging needed to monitor the position of the Neo-Chord tool along the length of the leaflet. Even with the augmented reality system where previously deployed neochordae were shown, it was easy to over fixate on the ICE images as the jaws of the NeoChord were being closed. The user frequently would let the position of the tool drift significantly during leaflet capture before detecting the problem in the 3D

TEE images and repositioning the tool. These difficulties could be mitigated through more training and improvements to the AR environment such as providing feedback if the tool is moved during leaflet capture. It should be noted that user experience plays a large role in traditional procedures with experienced surgeons requiring significantly fewer attempts and less time to grasp the leaflet[29] and this study was limited by using only a single non-expert user. While the rapid-prototype tool provided a means of developing the custom valve implantation tool, it was not as mechanically robust as the original NeoChord DS-1000 and a sturdier material is required to make a device suitable for larger scale animal and phantom experiments.

2.4 Conclusion

Here we presented AR guidance systems for TAVI and minimally invasive mitral valve repair. Although these results are preliminary, in both systems we demonstrated how ultrasound imaging could be integrated directly into the surgical tool assist in final positioning and deployment. In the TAVI system both the AR and AR+ICE systems were tested in a phantom environment and compared against fluoroscopic guidance. The standard deviation in deployment depth using fluoroscopic guidance was 3.4mm providing a lower bounds for the RMSE deployment error. The RMSE for the AR system was also found to be 3.4mm using AR alone and 2.3mm when ICE imaging was integrated into the delivery tool. These results show that an augmented reality system may achieve similar or better results than contrast enhanced fluoroscopy while eliminating the use of nephrotoxic contrast and ionizing radiation. The proposed system used only intraoperatively defined anatomy resulting in simplified clinical workflow without requiring preoperative models to be registered to the intraoperative TEE. In addition, the tool with integrated ICE provided real-time imaging

during valve deployment that shows the position of the stent relative to the native aortic valve. In these experiments, the ICE imaging decreased the error in valve deployment. In addition, the direct imaging of the stent and pertinent anatomy provides an extra layer if there were errors in tracking the stent or in the definition of the aortic valve. The phantom study presented here provides a direct comparison of these techniques to fluoroscopic guidance on a larger scale than feasible in animal studies.

Integrated ICE imaging was then applied to mitral valve repair where it was incorporated into a modified NeoChord DS-1000. The augmented reality environment used in this experiment was developed for the targeting task where the tool is navigated to the mitral valve annulus. The surgeon would then switch to using the live TEE for positioning the NeoChord device and grasping the leaflet. However, by including the ICE images in the virtual reality environment we were able to provide the real-time feedback necessary for the positioning task within a unified guidance system. The virtual representation of the valve annulus, while on its own not useful during leaflet grasping, added valuable context to the ICE images. This on-site ultrasound imaging appears very promising for achieving consistent bite depth and can provide detailed images showing the leaflet being captured between the jaws of the NeoChord device. Although previously deployed neochordae can be easily identified from the ICE images it was difficult to use this information to deploy additional chordae at an adjacent site. In the future, this difficulty could be ameliorated through user training and improvements to the AR environment.

Bibliography

[1] Bernard Iung, Agnès Cachier, Gabriel Baron, David Messika-Zeitoun, François De-
    lahaye, Pilar Tornos, Christa Gohlke-Bärwolf, Eric Boersma, Philippe Ravaud, and
    Alec Vahanian. Decision-making in elderly patients with severe aortic stenosis: why
    are so many denied surgery? *European Heart Journal*, 26(24):2714–2720, 2005.

[2] Alain Cribier, Helene Eltchaninoff, Assaf Bash, Nicolas Borenstein, Christophe Tron,
    Fabrice Bauer, Genevieve Derumeaux, Frederic Anselme, François Laborde, and
    Martin B Leon. Percutaneous transcatheter implantation of an aortic valve prosthesis
    for calcific aortic stenosis. *Circulation*, 106(24):3006–3008, 2002.

[3] Enrico Cerrato, Luis Nombela-Franco, Tamim M Nazif, Helene Eltchaninoff,
    Lars Søndergaard, Henrique B Ribeiro, Marco Barbanti, Fabian Nietlispach, Peter
    De Jaegere, Pierfrancesco Agostoni, et al. Evaluation of current practices in tran-
    scatheter aortic valve implantation: The WRITTEN (WoRldwIde TAVI ExperieNce)
    survey. *International Journal of Cardiology*, 228:640–647, 2017.

[4] Martin B Leon, Craig R Smith, Michael Mack, D Craig Miller, Jeffrey W Moses,
    Lars G Svensson, E Murat Tuzcu, John G Webb, Gregory P Fontana, Raj R Makkar,
    et al. Transcatheter aortic-valve implantation for aortic stenosis in patients who cannot
    undergo surgery. *New Engl J Med*, 363(17):1597–1607, 2010.

[5] Martin B. Leon, Craig R. Smith, Michael J. Mack, Raj R. Makkar, Lars G. Svensson,
    Susheel K. Kodali, Vinod H. Thourani, E. Murat Tuzcu, D. Craig Miller, Howard C.
    Herrmann, Darshan Doshi, David J. Cohen, Augusto D. Pichard, Samir Kapa-
    dia, Todd Dewey, Vasilis Babaliaros, Wilson Y. Szeto, Mathew R. Williams, Dean

Kereiakes, Alan Zajarias, Kevin L. Greason, Brian K. Whisenant, Robert W. Hodson, Jeffrey W. Moses, Alfredo Trento, David L. Brown, William F. Fearon, Philippe Pibarot, Rebecca T. Hahn, Wael A. Jaber, William N. Anderson, Maria C. Alu, and John G. Webb. Transcatheter or surgical aortic-valve replacement in intermediate-risk patients. *New England Journal of Medicine*, 374(17):1609–1620, 2016. PMID: 27040324.

[6] Devdas T. Inderbitzin, Maurizio Taramasso, Fabian Nietlispach, and Francesco Maisano. Percutaneous mitral valve repair with mitraclip: Patient and valve selection for optimal outcome. *Current Cardiology Reports*, 18(12):129, 2016.

[7] NeoChord passes 500 patient treatment milestone follow-up data on 127 patients out to two years presented at EACTS 2016 [press release]. Oct 2016.

[8] Ander Regueiro, Juan F Granada, François Dagenais, and Josep Rodés-Cabau. Transcatheter mitral valve replacement: insights from early clinical experience and future challenges. *Journal of the American College of Cardiology*, 69(17):2175–2192, 2017.

[9] Cristian A Linte, John Moore, Chris Wedlake, and Terry M Peters. Evaluation of model-enhanced ultrasound-assisted interventional guidance in a cardiac phantom. *IEEE Transactions on Biomedical Engineering*, 57(9):2209–2218, 2010.

[10] Cristian A Linte, John Moore, Chris Wedlake, Daniel Bainbridge, Gérard M Guiraudon, Douglas L Jones, and Terry M Peters. Inside the beating heart: An in vivo feasibility study on fusing pre-and intra-operative imaging for minimally invasive therapy. *International Journal of Computer Assisted Radiology and Surgery*, 4(2):113, 2009.

[11] John T Moore, Michael WA Chu, Bob Kiaii, Daniel Bainbridge, Gerard Guiraudon, Chris Wedlake, Maria Currie, Martin Rajchl, Rajni V Patel, and Terry M Peters. A navigation platform for guidance of beating heart transapical mitral valve repair. *IEEE TBME*, 60(4):1034–1040, 2013.

[12] Pencilla Lang, Terry M Peters, Bob Kiaii, and Michael WA Chu. The critical role of imaging navigation and guidance in transcatheter aortic valve implantation. *J Thorac Cardiov Sur*, 143(6):1241–1243, 2012.

[13] Fabienne Aregger, Peter Wenaweser, Gerrit J Hellige, Alexander Kadner, Thierry Carrel, Stefan Windecker, and Felix J Frey. Risk of acute kidney injury in patients with severe aortic valve stenosis undergoing transcatheter valve replacement. *Nephrol Dial Transpl*, 24(7):2175–2179, 2009.

[14] Arnaud Van Linden, Jörg Kempfert, Ardawan J Rastan, David Holzhey, Johannes Blumenstein, Gerhard Schuler, Friedrich W Mohr, and Thomas Walther. Risk of acute kidney injury after minimally invasive transapical aortic valve implantation in 270 patients. *Eur J Cardio-Thorac*, 39(6):835–843, 2011.

[15] Justus T Strauch, Maximilian P Scherner, Peter L Haldenwang, Roman Pfister, Elmar W Kuhn, Navid Madershahian, Parwis Rahmanian, Jens Wippermann, and Thorsten Wahlers. Minimally invasive transapical aortic valve implantation and the risk of acute kidney injury. *Ann Thorac Surg*, 89(2):465–470, 2010.

[16] Rodrigo Bagur, John G Webb, Fabian Nietlispach, Eric Dumont, Robert De Larochelliere, Daniel Doyle, Jean-Bernard Masson, Marcos J Gutierrez, Marie-Annick Clavel, and Olivier F Bertrand. Acute kidney injury following transcatheter aortic valve im-

plantation predictive factors prognostic value and comparison with surgical aortic valve replacement. *European Heart Journal*, 31(7):865–874, 2010.

[17] Zhe Luo, Junfeng Cai, T Peters, and Lixu Gu. Intra-operative 2d ultrasound and dynamic 3d aortic model registration for magnetic navigation of transcatheter aortic valve implantation. *IEEE TMI*, 2013.

[18] Jörg Kempfert, Volkmar Falk, Gerhard Schuler, Axel Linke, Denis Merk, Friedrich W Mohr, and Thomas Walther. DynaCT during minimally invasive off-pump transapical aortic valve implantation. *Ann Thorac Surg*, 88(6):2041, 2009.

[19] Keith A Horvath, Dumitru Mazilu, Michael Guttman, Arthur Zetts, Timothy Hunt, and Ming Li. Midterm results of transapical aortic valve replacement via real-time magnetic resonance imaging guidance. *J Thorac Cardiov Sur*, 139(2):424–430, 2010.

[20] American Hospital Association. Adopting technological innovation in hospitals: who pays and who benefits? Technical report, American Hospital Association, October 2006.

[21] Enrico Ferrari, Christopher Sulzer, Elena Rizzo, and Ludwig Karl von Segesser. A fully echo-guided trans-apical aortic valve implantation. *Eur J Cardio-Thorac*, 36(5):938–940, 2009.

[22] Enrico Ferrari, Christopher Sulzer, Carlo Marcucci, Elena Rizzo, Piergiorgio Tozzi, and Ludwig K von Segesser. Transapical aortic valve implantation without angiography: proof of concept. *Ann Thorac Surg*, 89(6):1925–1932, 2010.

[23] Pencilla Lang, Martin Rajchl, A Jonathan McLeod, Michael W Chu, and Terry M Peters. Feature identification for image-guided transcatheter aortic valve implantation.

In *SPIE Medical Imaging*, pages 83162X–83162X. International Society for Optics and Photonics, 2012.

[24] Kestutis Rucinskas, Diana Zakarkaite, Rita Kramena, Robertas S Samalavicius, Vilius Vilius Janusauskas, Giovani Speziali, and Audrius Aidietis. Tct-803 3d transesophageal echocardiography provides optimal real-time guidance for off-pump, transapical implantation of artificial chordae tendineae. an imaging study. *Journal of the American College of Cardiology*, 64(11_S), 2014.

[25] Andrea Colli, Erica Manzan, Fabio Zucchetta Fabio, Cristiano Sarais, Demetrio Pittarello, Giovanni Speziali, and Gino Gerosa. TEE-guided transapical beating-heart neochord implantation in mitral regurgitation. *JACC: Cardiovascular Imaging*, 7(3):322–323, 2014.

[26] Claire Vannelli, John Moore, Jonathan McLeod, Dennis Ceh, and Terry Peters. Dynamic heart phantom with functional mitral and aortic valves. In *SPIE Medical Imaging*, page 941503. International Society for Optics and Photonics, 2015.

[27] Kestutis Rucinskas, Vilius Janusauskas, Diana Zakarkaite, Sigita Aidietiene, Robertas Samalavicius, Giovani Speziali, and Audrius Aidietis. Off-pump transapical implantation of artificial chordae to correct mitral regurgitation: early results of a single-center experience. *The Journal of Thoracic and Cardiovascular Surgery*, 147(1):95–99, 2014.

[28] Joerg Seeburger, Mauro Rinaldi, Sten Lyager Nielsen, Stefano Salizzoni, Ruediger Lange, Markus Schoenburg, Ottavio Alfieri, Michael Andrew Borger, Friedrich Wilhelm Mohr, and Audrius Aidietis. Off-pump transapical implantation of artificial neochordae to correct mitral regurgitation: the tact trial (transapical artificial chordae ten-

dinae) proof of concept. *Journal of the American College of Cardiology*, 63(9):914–919, 2014.

[29] Joerg Seeburger, Sergej Leontjev, Michael Neumuth, Thilo Noack, Michael Höbartner, Martin Misfeld, Michael A Borger, and Friedrich W Mohr. Trans-apical beating-heart implantation of neo-chordae to mitral valve leaflets: results of an acute animal study. *European Journal of Cardio-Thoracic Surgery*, 41(1):173–176, 2012.

Chapter 3

Detection and Visualization of Dural Pulsation

This chapter includes material adapted from:

3.1 Introduction

Epidural injections are a common intervention with an estimated 293 000 procedures performed annually in the United Kingdom [1]. There is increasing interest in using perioperative epidural injection as concurrent epidural and general anesthesia reduces the morbidity and mortality for a wide variety of surgeries [2]. Accurate localization of the dura is critical

65

in epidural and spinal anesthesia as advancing the needle too far has the potential to cause severe damage to the spinal cord, resulting in long-term neurological complications. In epidural injections, the analgesic must be injected into the epidural space inside the spinal canal but outside the dura. This procedure is traditionally performed using a blind technique in which the vertebral interspace is identified solely using palpation and the needle depth is determined by the anesthetist feeling for a loss of resistance indicative of the needle puncturing the ligamentum flavum and entering the epidural space. Spinal anesthesia is performed similarly, but the needle is inserted through the dura and the anesthetic injected into the subarachnoid space using a smaller needle delivering much less anesthetic. Without image guidance, even identifying a specific vertebral interspace is a challenging task where experts are successful in fewer than half the cases [3, 4]. Multiple attempts at needle insertion are common [5, 6], and a small but significant number of cases result in long term complications [7]. Spinal ultrasound, acquired from a midline or paramedian view, is becoming increasingly common in spinal needle interventions [8, 6]. Ultrasound guidance can significantly reduce the number of failed and traumatic procedures as well as the number of needle insertion attempts per procedure [9]. The vertebrae are readily visible in US, aiding in selecting the needle trajectory, but the image quality is poor within the spinal canal making it difficult to locate the dura and other important features.

However, the changing pressure of the cerebral spinal fluid throughout the cardiac cycle caused by the vascularization of the brain and spinal cord results in a subtle pulsation of the dural membrane which can be perceived in US. The visual presence of dura pulsation also confirms the correct paramedian position of the US probe as it indicates the presence of a large acoustic window between the vertebra which may be suitable for needle insertion. This pulsation is a valuable cue for identifying the dura, and ensuring that the needle is

inserted to the appropriate depth, but it is only perceived in approximately 30% of cases [6].

Currently, there is no suitable technique for detecting dural motion. While anesthetists have become accustomed to using Doppler US to detect important vessels in other nerve block procedures, identifying dural pulsation through Doppler US is challenging because of the low velocity of the motion, which is often orthogonal to the beam direction. Speckle tracking techniques are another alternative that have been used to assess dural pulsation in cervical laminoplasty, but require imaging perpendicular to the spinal cord using a view preselected with MRI [10]. The out-of-plane motion, particularly significant with the paramedian approach, severely degrades methods that rely on explicit motion or velocity estimation. This chapter develops a technique to identify and display subtle dural pulsation that may be missed in an interventional setting by fitting a harmonic model to individual pixel intensities through extended Kalman filtering. By only looking for periodicity in the intensity values, this method does not require an explicit motion model and is agnostic to whether the intensity changes are caused by out-of-plane motion. This method can run in real-time, requires only the B-mode video, and is easily integrated into existing imaging systems allowing pulsatile motion to be visualized on the original US image or in an augmented reality guidance system.

3.1.1 Related Work

Recently, there has been great interest in motion magnification techniques that can reveal almost imperceptible motions within a specified frequency band [11, 12, 13, 14]. The earliest of these methods, Liu et al. [11] tracked a dense collection of feature points automatically generated from a video, clustering them by the coherence of their motion. These

feature points could then be used to create motion maps which can be exaggerated or fil-tered accordingly. Wu et al. [12] proposed a fundamentally different technique by detecting changes in intensity on a pixel-by-pixel basis, eliminating the need for tracking features. This framework used a Laplacian pyramid to decompose the picture into a collection of frequency bands, each of which was subjected to temporal bandpass filtering on a pixel-level. The filtered signals were amplified and added back into the originals to synthesize a video with exagerated motions. Wadwa et al. [13, 14] built on this approach by filtering local phase instead of intensity which greatly improved the results on natural video. These frameworks were first used in the context of surgical interventions by McLeod et al. [15] in robot-assisted prostatectomy, and Amir-Khalili et al. [16] in robot-assisted partial nephrec-tomy. Rather than simply enhancing motion, Amir-Khalili et al, performed a multiscale segmentation using the filter response at different levels of the steerable pyramid.

Other work has focused on segmenting or detecting periodic motion in natural images. Sietz and Dyer [17] investigated the detection and classification of periodic motion after being transformed by a time-varying affine operator which they used to model a camera projection operator, but required explicitly tracking points on the object of interest. Polana and Nelson [18] developed a framework for periodic motion detection of tracked objects using Fourier analysis and harmonic detection on a motion field estimated between suc-cessive image frames. Cutler and Davis [19] presented a similar framework in which a similarity plot compares pairs of frames in which the tracked object is isolated in a bound-ing box. The power spectrum or autocorrelation of this similarity plot is used to detect the significant frequencies of the signal associated with periodic motion.

More recent work has focused on pixel-by-pixel analysis within the tracked patch, seg-menting the periodically moving object. Briassouli and Ahuja [20] developed an approach

for tracking multiple periodically-moving objects through their projections onto the x and y axes while Ran et al. [21] used a spectral analysis of each pixel intensity within a tracked patch to detect periodicity. Pogalin et al. [22] extended this approach by using principle component analysis to capture a compact representation of the temporal variation in the video so that where periodicity was present it was concentrated in a small number of principle components.

3.1.2 Contributions

This chapter presents a framework for the automatic detection and localization of subtle periodic motion in US images, specifically very low velocity and out-of-plane motion that cannot readily be detected by Doppler utlrasound. This framework, which uses extended Kalman filtering to fit a periodic model to the image intensity in a tracked image patch, is computationally inexpensive, and runs in real-time on a clinically available ultrasound machine, SonixTouch (Ultrasonix, Richmond, BC, Canada).

While previous approaches for periodic motion detection have focused on natural images with low background motion, ultrasound images present unique challenges. Even small breathing and probe motion, combined with the speckle, cause background pixels to exhibit more complex noise dynamics. This poses a distinct limitation for methods making the assumption of white background noise. Instead this framework fits a sinusoidal model with time-varying parameters using an extended Kalman filter. This approach is more computationally efficient than spectral techniques and segmentations based on the fitted parameters appear more robust to the background noise dynamics. This framework is presented and validated in the context of detecting otherwise imperceptible dural pulsation for image-guided epidural and spinal anesthesia, using both human and phantom data.

3.2   Methods

Our goal is to localize the dura by detecting pixels with a periodic intensity signal indicative of motion. Statistical tests for periodicity in a time series date back to Fisher [23] who derived a test for the presence of a periodic signal from the fraction of the power concentrated in the dominant spectral component. Since then, many spectral and epoch folding methods have been proposed, but their focus has been on offline use. Instead, we fit a harmonic model to the pixel intensities and use the fitted parameters (frequencies, amplitudes) as features for detecting pulsatile motion. Kalman filtering is well established for online model fitting and parameter estimation, and has be used extensively as a frequency tracker [24]. High order harmonic models have been previously used for modeling cardiac signals [25] and tracking the position of mitral valve leaflets in US [26].

3.2.1   Extended Kalman Filtering Model

An extended Kalman filter (EKF) is used for estimating the frequency and other pertinent parameters that can be used to locate periodicity in pixel intensity, z. The state vector, x, and nonlinear observation model, $h(x)$, are defined as:

$$x = \left[\begin{array}{ccccccc} \theta, & \omega, & \phi_2, & \ldots & \phi_N, & A_1, & \ldots & A_N, k \end{array} \right]^\top$$
$$h(x) = k + A_1 \sin(\theta) + \sum_{n=2}^{N} A_n \sin(n\theta + \phi_n)$$

(3.1)

where ω is the estimated fundamental frequency of the signal, A_1 and θ are the amplitude and phase at said frequency. $A_2 \ldots A_n$ and $\phi_2 \ldots \phi_n$ are the amplitudes and relative phases of the first N harmonics. The analytic Jacobian for the observation model can be easily derived

from these equations, yielding the extended Kalman filtering estimation framework:

State estimation: $x_{k|k-1} = F x_{k-1|k-1}$ where $F = \begin{bmatrix} 1 & 1 & & 0 \\ 0 & 1 & & \\ \hline 0 & & I \end{bmatrix}$

Estimation covariance: $P_{k|k-1} = F P_{k-1|k-1} F^\top + Q$

Residual: $\tilde{y}_k = z_k - h(x)$

Residual covariance: $S_k = H_k P_{k|k-1} H_k^\top + R$ where $H = \left. \dfrac{\delta h}{\delta x} \right|_{x_{k|k-1}}$

Kalman gain calculation: $K_k = P_{k|k-1} H_k^\top S_k^{-1}$

State estimation update: $x_{k|k} = x_{k|k-1} + K_k \tilde{y}_k$

Estimation covariance update: $P_{k|k} = (I - K_k H_k) P_{k|k-1}$

$$(3.2)$$

with all parameters except the phase, θ, following a random walk. In this framework, state transitions are linear, allowing F to be a constant state transition matrix. H is the Jacobian matrix associated with the nonlinear observation model, P the state estimate covariance matrix, Q the (constant) state noise covariance, and R the (constant) pixel intensity noise covariance. $\tilde{y}$ and S are the residual and residual covariance respectively.

One issue with this model is that it is easily trapped in local minima, particularly when the frequency is near zero. This can be mitigated by constraining the frequency parameter by restricting its value using Parameter Clamping, a well established method of applying inequality constraints in Kalman filtering [27]. Therefore, we clamp the EKF frequency to

be between 30bpm and 180bpm. Another issue with this model is that patient and probe motion can corrupt the periodic signal. This can be mitigated by applying a patch tracking algorithm that minimizes the sum of absolute differences (frame-to-frame translations within a 3 pixel radius) to track the ROI as this motion occurs.

The state vector of this model can be seen as a feature vector for each pixel and used for detecting and visualizing the dura. The frequency, amplitudes, and relative phase of higher order harmonics help characterize the motion at that pixel. For real-time applications, we found simply thresholding the fundamental frequency and its amplitude was sufficient to localize the dura. A heat map showing the amplitude at the fundamental for pixels within this segmentation helps visualize where the pulsation was strongest. In this study the thresholds were interactively specified by the user, but in future could be automatically determined from the state data. While processing higher order harmonics can help model the periodic intensity caused by pulsation, the increase in model complexity and computational costs were unnecessary for visualizing these structures.

3.2.2   Frequency Smoothing

While the EKF can be applied to each pixel independently, this ignores all information about the local neighborhood. In particular, the frequency estimates obtained from a single pixel can be very noisy. Ideally, the EKF would observe all pixels within a neighborhood but this greatly increases the memory and computational requirements. Faster and more stable convergence can be achieved by extending the model with a perfect observation of the average frequency of the surrounding 3-by-3 neighborhood:

$$\bar{z} = \left[\begin{array}{c} z \\ \hline \bar{\omega} \end{array} \right], \qquad \bar{Q} = \left[\begin{array}{c|c} Q & 0 \\ \hline 0 & \epsilon \end{array} \right],$$

$$\bar{x} = \left[\begin{array}{c} x \\ \hline \bar{\omega} \end{array} \right], \qquad \bar{R} = \left[\begin{array}{c|c} R & 0 \\ \hline 0 & 0 \end{array} \right], \qquad \bar{F} = \left[\begin{array}{c|c} & \alpha \\ & \alpha \\ F & 0 \\ & \vdots \\ \hline 0\dots & 1 \end{array} \right] \qquad (3.3)$$

where $\epsilon \to 0$ and $\bar{\omega}$ is the difference between the frequency of the pixel and the amplitude weighted mean frequency of the neighborhood. This improves the random walk model of the frequency estimate by causing it to drift towards the local mean. A parameter $\alpha \in [0, 1]$ was introduced to control the degree of this drift. This method is equivalent to spatially smoothing the frequencies weighted by their amplitude after each update phase of the EKF algorithm. This frequency smoothing is more efficient and numerically stable than appending the local frequency into the observation model and so permits a simpler and more efficient implementation.

3.3 Results

3.3.1 Synthetic Images

To verify robustness to noise and quantization error, this approach was tested on a set of synthetic videos consisting of a pulsating target located in the center of an otherwise static background. The target was a circle of radius 7 pixels whose intensity varied sinusoidally with an amplitude of 5 intensity levels at a frequency of 60 bpm sampled at 38 fps. Three levels of frequency smoothing were used where Gaussian white noise has been added with σ's of 0, 1.25, 2.5, and 3.5 intensity levels, the latter three corresponding to SNR's of 8, 2,

and 1 respectively.

Figure 3.1 displays the results of the synthetic experiment after 5 seconds of filtering. Frequency smoothing improved the performance of the filtering which was particularly noticeable at higher noise levels in which it helped to reduce the effects of noise in the background resulting in a much cleaner segmentation with fewer erroneously segmented pixels. In all cases, the error in estimated amplitude for the pulsating structure was negligible.
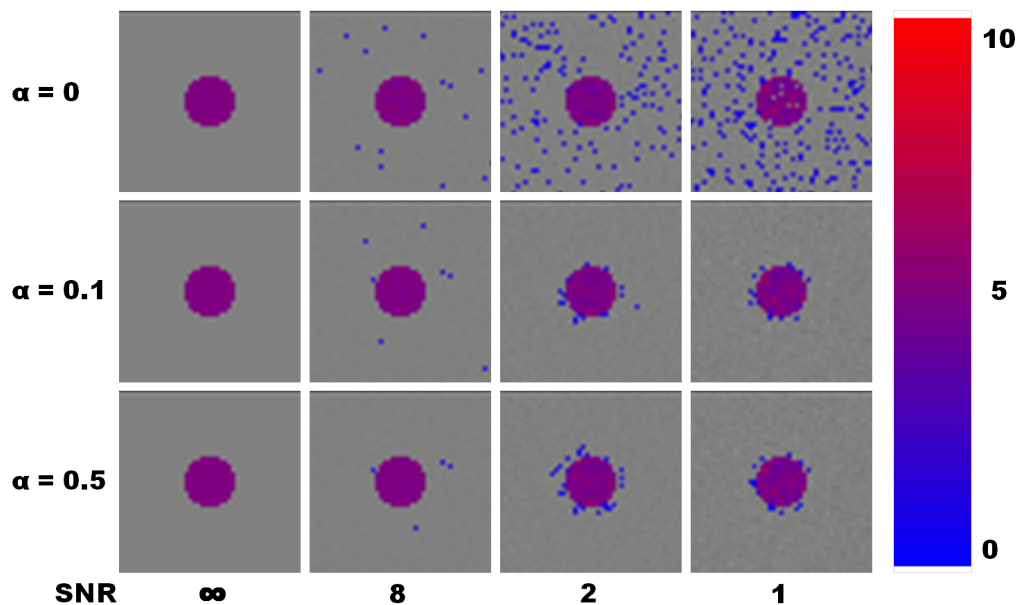
Figure 3.1: The detection of pulsation in synthetic images is shown for varying levels of white noise and the frequency smoothing parameter, α. A small amount of frequency smoothing greatly improves periodicity segmentation.

3.3.2 Human Data

Two paramedian US videos, acquired at 43 and 38 fps from two healthy humans, were processed retrospectively. The EKF detects the relevant pulsation in both subjects within five seconds, which can easily be incorporated into the current clinical work-flow. To visualize

the pulsation a segmentation was generated by thresholding based on the estimated parameters. This included all pixels with an estimated amplitude greater than 0.5 and a frequency within ±25% of 75bpm (54 frames per beat) and 60bpm (38 frames per beat) for the first and second videos respectively. A heat map showing the amplitude of these pixels was overlaid on the original images as shown in Figure 3.2. In practice, this target frequency can be adjusted interactively to estimate the heart rate and generate the visualization.

A time-profile taken through the center of the pulsating dura shows an oscillation in intensity for approximately two seconds before being detected by the EKF and rendered as a color overlay. The output of the EKF is also shown as it tracks this periodicity in pixel intensity in Figure 3.3 along with the corresponding state estimates.

For comparison, we examined the pixel-wise spectrum obtained from the video using the fast Fourier transform on the ROI after registration. Ran et al.[21] advocate using the ratio of peak power in the spectrum to the variance of the signal. This ratio is Fisher's g statistic for periodicity and has a known distribution under the assumption of white Gaussian noise, in which case thresholding is equivalent to a likelihood ratio test [28]. In addition to this statistic, we generated an alternate visualization using the same thresholds and priors on heart rate but based solely on the spectrum of the pixel intensities as shown in Figure 3.4. While more complex spectral estimation techniques go beyond the scope of this chapter, these visualizations show that directly using the frequency and amplitudes obtained through a Fourier transform or using Fisher's statistic for periodicity are not sufficient to detect the dura. It should also be noted that real-time Fourier analysis introduces its own challenges as a sufficiently large buffer of previous data must be stored and analyzed at every iteration.
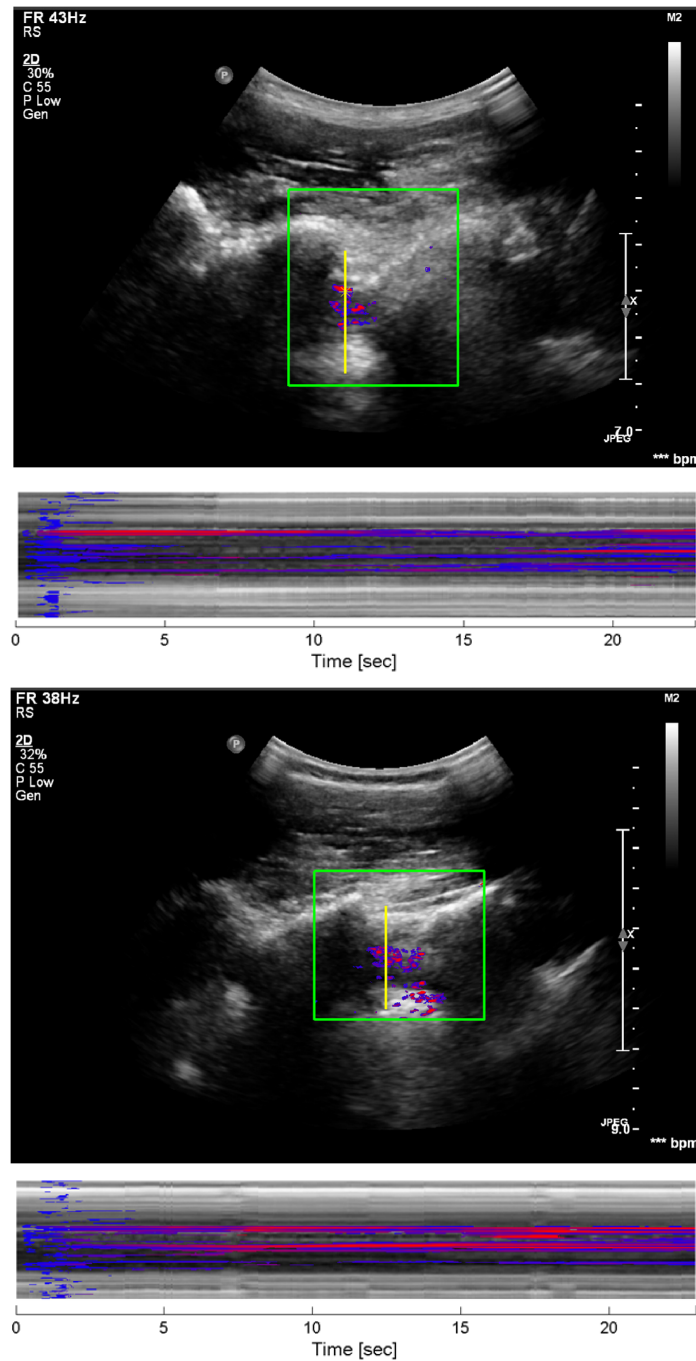
Figure 3.2: Retrospective processing was performed on the two human videos in the region of interest covering the spinal canal (shown in green) and the detected pulsation is visualized using a heat map. A time-profile view taken from the yellow line is displayed below the corresponding image. The Kalman filter output along with all of its states with respect to time are shown in Figure 3.3 at the point denoted by the yellow asterisk in the first image.

(a) Intensity of the video (black) and EKF prediction (red)

(b) Fundamental frequency estimate

(c) Amplitude estimate at fundamental frequency

(d) Phase estimate at fundamental frequency

(e) Local level estimate
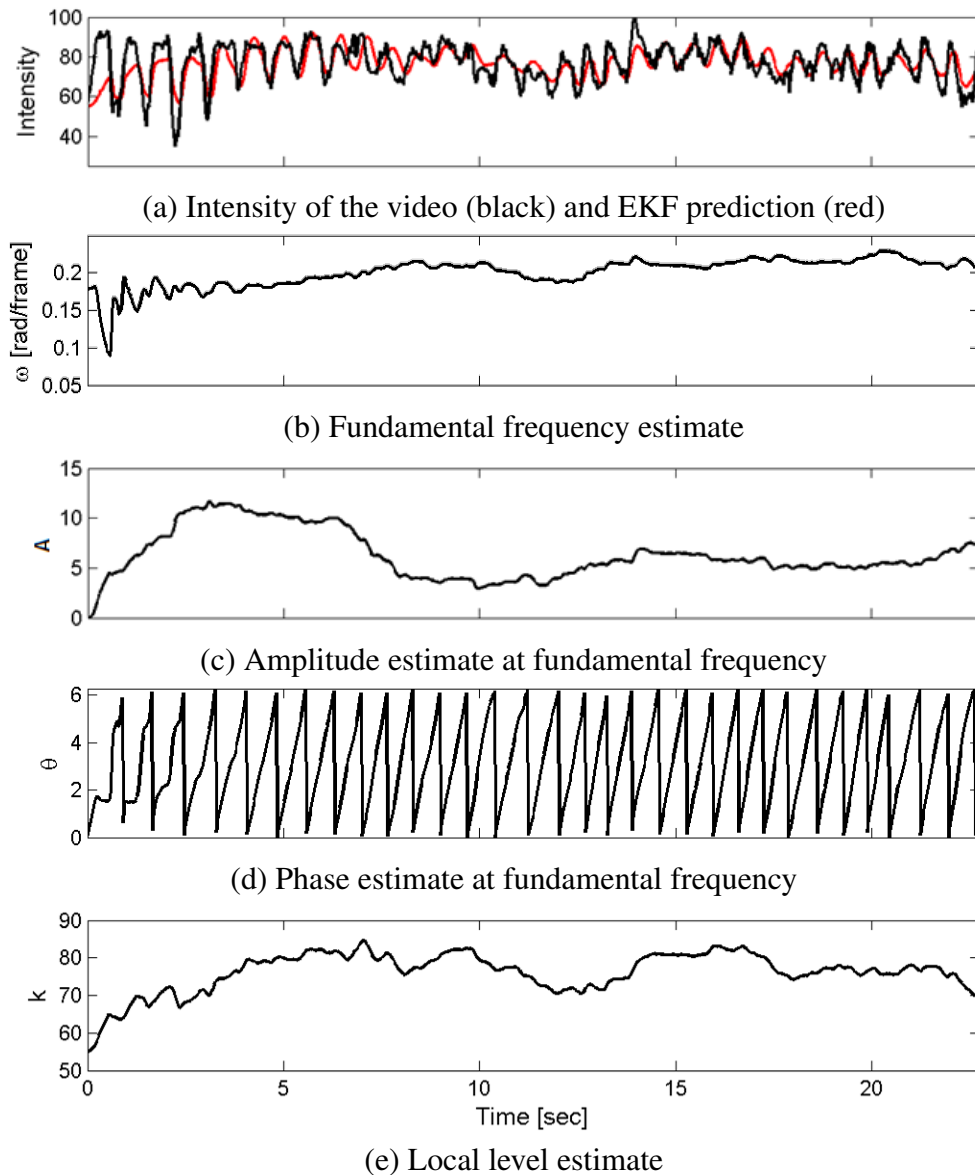
Figure 3.3: The pixel intensity and EKF prediction along with associated EKF estimates of fundamental frequency, amplitude, phase, and local level are shown at the point denoted by the yellow asterisk in Figure 3.2. The frequency converges after approximately 5 seconds. The local level is modeled by a random walk and takes into account most of the large non-periodic changes in intensity.

(a)   (b)   (c)
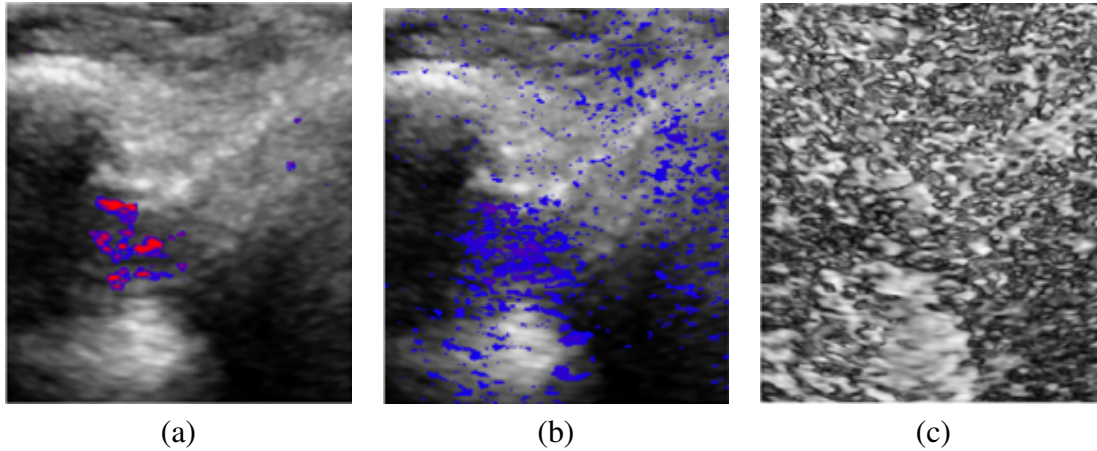
Figure 3.4: Results of the periodic visualization using the proposed method (a). Same visualization using the frequency and amplitudes obtained from spectral analysis (b). Image showing Fisher's statistic for periodicity (c).

(a)   (b)
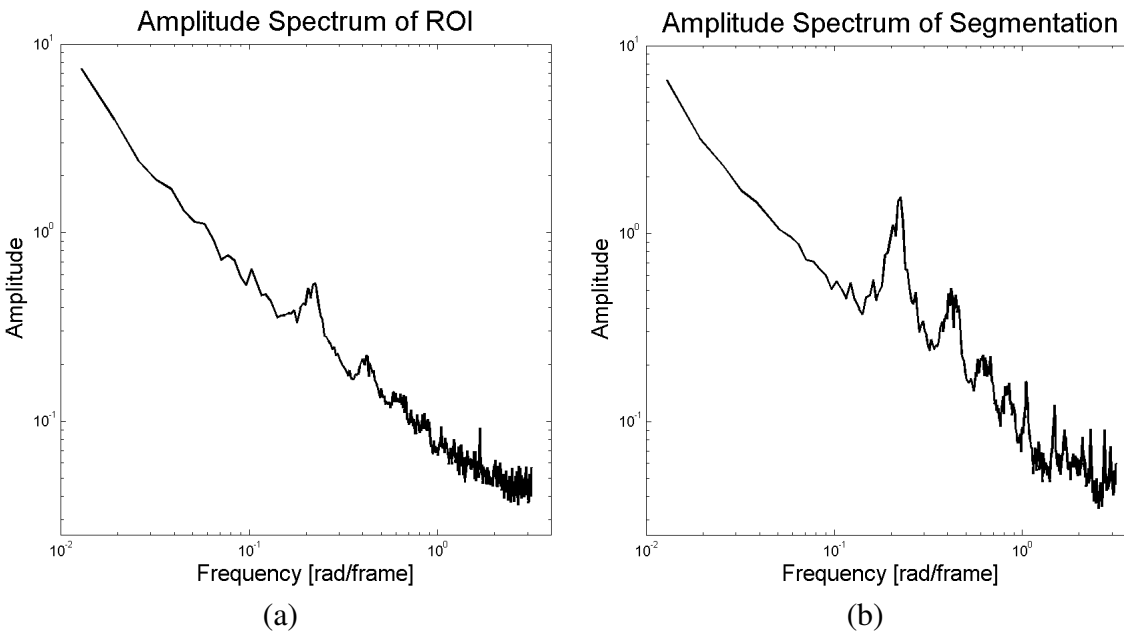
Figure 3.5: Amplitude spectrum of intensity within the entire ROI (a) and within the periodic segmentation using the proposed method (b) for the first human video. The peak in amplitude around $0.2 rad/frame$ is much more pronounced in the segmented region where the fundamental frequency and first three harmonics are clearly visible. However, the spectrum is still dominated by lower frequency noise and naive spectral analysis performs poorly.

The proposed method performed much better than simple spectral analysis techniques. To investigate this observation in more detail we plotted the amplitude spectrum of the entire ROI, as well as the spectrum of only the segmented pixels (Figure 3.5). Both spectra are clearly not consistent with white noise and are dominated by low frequencies. This causes severe problems with the spectral techniques unless a whitening filter or other appropriate preprocessing is applied. Brownian noise is associated with 20dB/decade falloff, an apparent slope of $-45°$ in Figure 3.5, which is much closer to the observed spectra and is consistent with the random walk model of the local level included in the Kalman filtering. Treating the remaining parameters as time-varying also adds more robustness to unmodeled dynamics.

3.3.3 Interventional Phantom

Lastly, the method was tested on a spinal phantom designed for training in spine needle procedures [29]. This phantom consists of five major components: a 3D printed spine segmented from a patient CT, silicone rubber tube simulating the ligatum flavum, latex tube simulating the dura, polyvinyl chloride-plastisol simulating fat, and a layer of opaque silicone rubber for the skin. Dural pulsation was induced at 60 bpm using a small motor. The phantom is shown in Figure 3.6.

Our software implementing this framework was instantiated on the US system (Sonix-Touch, Ultrasonix, Richmond, British Columbia) and a paramedian view was emulated. The amount of pulsation in the dura could be controlled to generate more subtle pulsation than present in our human videos. The algorithm was able to run at 18 frames per second on the US machine with a region of interest covering the vertebral interspace. After approximately 4 seconds, very subtle pulsation was detected and revealed (Figure 3.7). The
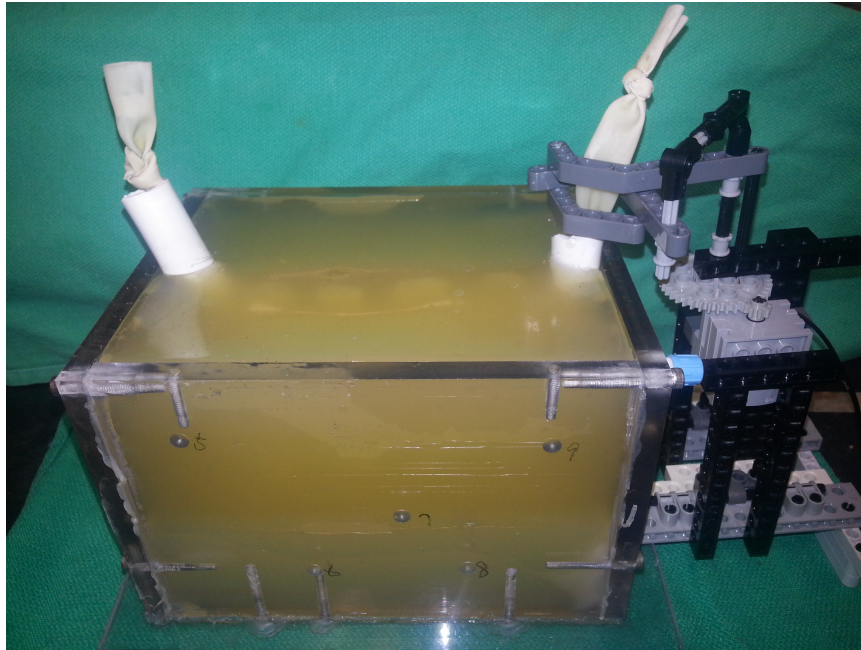
Figure 3.6: Spinal phantom consisting of 3D printed L2 to L5 vertebra surrounded by fat-mimicking polyvinyl chloride-plastisol. Pulsations of the dura-simulating latex tube were mechanically actuated at approximately 60 bpm.

peak-to-peak intensity amplitude in the area detected was approximately 6 intensity levels in an 8 bit image and at the edge of human perception. This pulsation was only noticed retrospectively after being detected by the filter.

To quantitatively evaluate the efficacy of our proposed motion detection framework, an expert anesthesiologist performed a sequence of epidural injections on this interventional phantom both with and without motion detection applied. Injection sites were chosen in the intervertebral spaces between L2-3 and L4-5 inclusive on both the left and right sides. A total of 12 trials were performed. For each trial, the injection was performed twice, once with and once without motion detection. The order in which the injections were performed was randomized to mitigate the effects of learning, fatigue, and any degradation of the phantom, such as residual needle tracks, between injections.
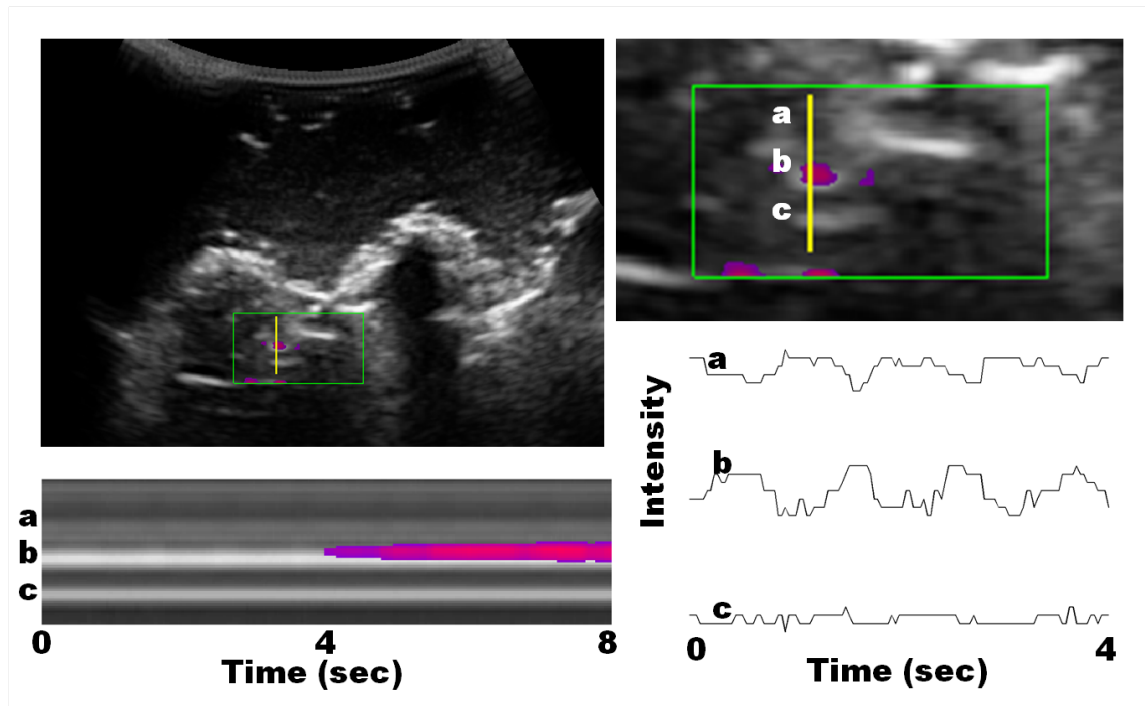
Figure 3.7: US acquired on phantom showing user defined region of interest in green and detected pulsatile motion in red is shown top left. A zoomed in view of the region of interest is shown top right. A time-profile taken across the yellow line is shown bottom left. The intensity time series at the points a, b and c are shown bottom right. As the processing was performed in real-time on the US machine with only the output visualization being captured by a second computer, the internal state of the EKF is unavailable.

These paired injections were measured in terms of the normalized path length, which is the length of the needle trajectory normalized by the shortest distance between the start and end points, the number of attempts taken to successfully complete the injection procedure, and the time taken for the injection. Figures 3.8, 3.9, and 3.10 display the results for each measure, respectively. Although not tested for, due to low sample size, no obvious learning effect or fatigue is visible in any of performance metric graphs.

The differences between the results are presented in Table 3.1. Statistically significant differences were found between the two methods for the normalized path length using a

paired t-test ($p = 0.007$) and the number of attempts using a nonparametric permutations test ($p = 0.016$). No significant difference was found in the procedure time ($p = 0.138$).
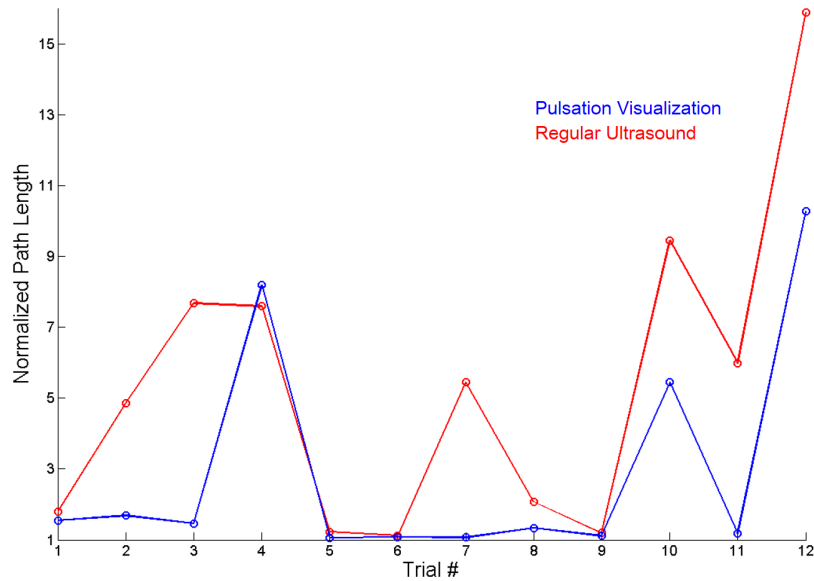
Figure 3.8: Normalized path length for mock epidural injections
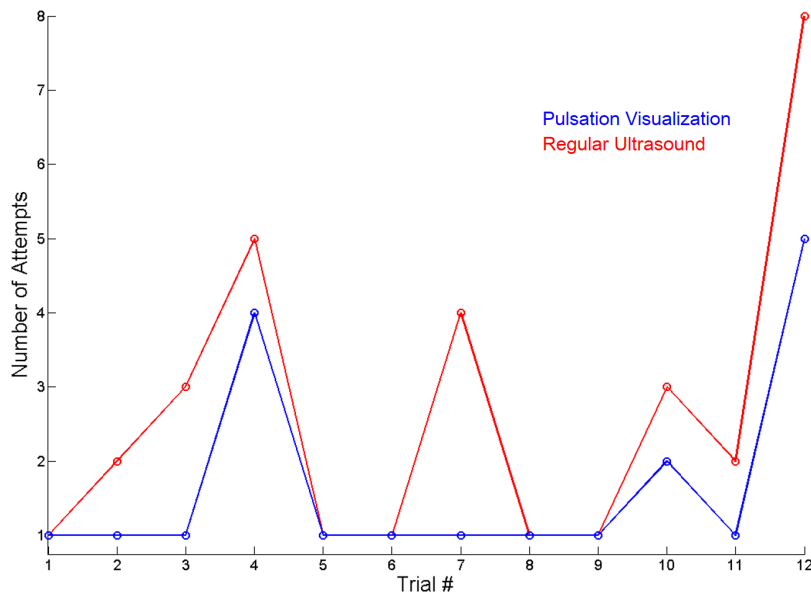
Figure 3.9: Number of attempts for mock epidural injections
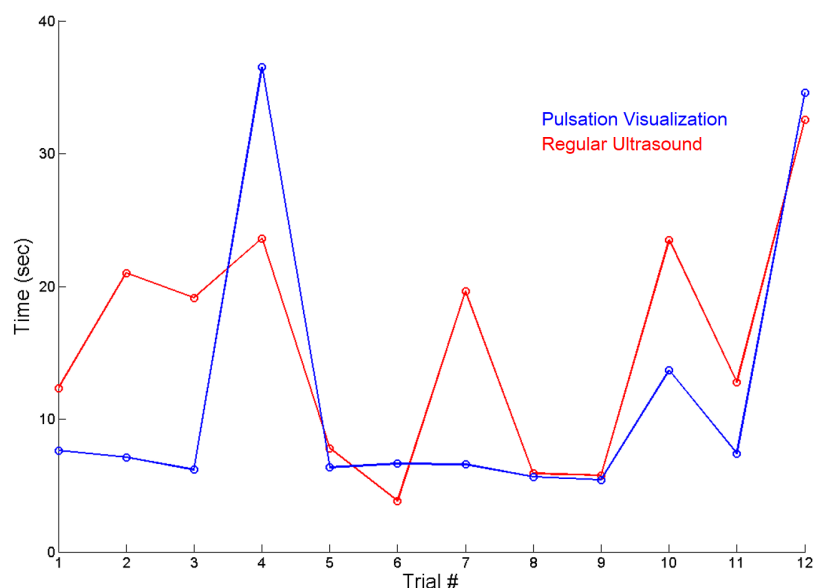
Figure 3.10: Time required for mock epidural injections

Table 3.1: Numerical results for mock epidural injections

	With Motion Detection	Without Motion Detection
Normalized Path Length	3.0 ± 3.2	5.4 ± 4.4
Number of Attempts	1.7 ± 1.4	2.7 ± 2.1
Time (sec)	12.0 ± 11.2	15.7 ± 9.0

3.4 Discussion

This approach has several advantages, in particular, its computational efficiency and real-time capabilities allow for ready integration into any clinical US with video output capabilities, with minimal impact on clinical workflow.

Using our current implementation, running the AR environment was difficult due to limited computational resources on a clinical US machine (SonixTouch, Ultrasonix, Richmond, British Colombia) and the region of interest was set sufficiently large as to cover the spinal canal while maintaining an acceptable frame rate. This problem could be resolved

by upgrading to a version of the US machine that allows for GPGPU acceleration or by processing on a secondary computer.

The two US videos of healthy humans are not representative of the full patient population, but still provides a valuable proof-of-concept demonstration. Phantom images were employed to show the detection of very subtle pulsations that are on the edge of human perception. Future work in this area will include retrospective patient studies to account for this limitation, as well as more extensive validation through user studies on patient data and mock procedures performed on the phantom. In addition to traditional B-mode images, this method could be used to enhance in-plane periodic motion observed in both Doppler imaging and speckle tracking.

3.4.1 Augmented Reality Environment

The proposed framework can also improve more complex AR guidance systems for needle insertion by showing the location of the pulsating dura in the virtual environment. An augmented reality (AR) environment with an associated magnetic tracking system (NDI Aurora, Waterloo, Ontario) was used to show the tracked US in relation to a spine model and tracked surgical tools. The AR environment was displayed on the US screen side-by-side with a second view consisting solely of the US image. Both views were enhanced with the proposed EKF-based coloring mechanism.

In phantom experiments, the position of the spine can be determined *a priori*, but in a practical implementation the spine model would need to be obtained through registration with preoperative images or a generalized atlas [30]. Future work in analyzing the clinical efficacy of this framework will be centered around whether or not pulsation detection and AR combined improve performance on these needle insertion tasks (Figure 3.11).
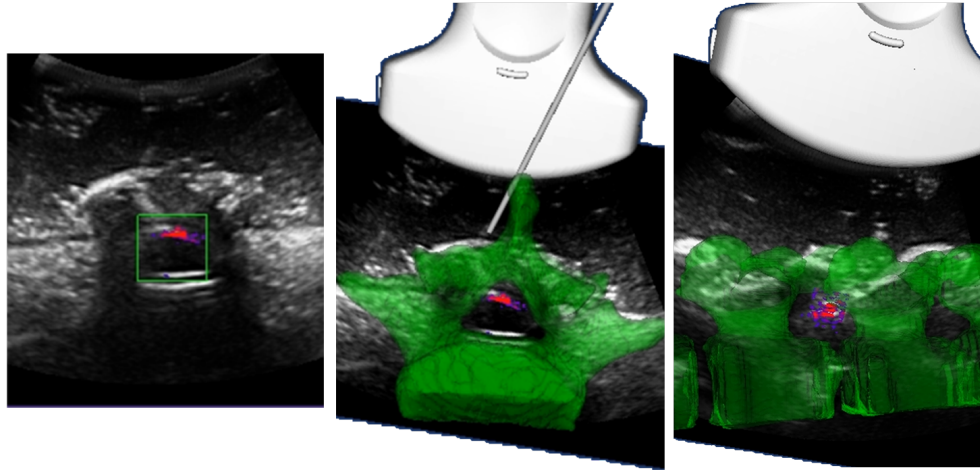
Figure 3.11: US image acquired with a midline view is shown on the left. The corresponding AR view with the needle being inserted is shown in the center. The AR system is also shown simulating a paramedian view on the right. The detected pulsation localizes the dura inside the spinal canal as seen in the AR views.

3.5   Conclusion

We found that subtle dural pulsations could be detected using this technique. While the EKF can generate a rich feature vector, simple thresholding of the estimated frequency and amplitude was sufficient to localize the dura. This model based approach was robust to background motion and noise present in the ultrasound videos. When used in mock procedures on a phantom, the pulsation visualization substantially decreased the normalized path length and number of attempts required to reach the epidural space. This method can be integrated directly into clinical scanners or on a separate computer receiving a video feed from the US. In this study, we used synthetic, human, and phantom images to validate this technique. The results presented here show promise in providing useful information in an interventional setting that we expect will provide great clinical benefit in spine needle interventions.

Bibliography

[1] TM Cook, D Counsell, and JAW Wildsmith. Major complications of central neuraxial block: report on the third national audit project of the royal college of anaesthetists. *British Journal of Anaesthesia*, 102(2):179–190, 2009.

[2] Daniel M Pöpping, Nadia Elia, Hugo K Van Aken, Emmanuel Marret, Stephan A Schug, Peter Kranke, Manuel Wenk, and Martin R Tramèr. Impact of epidural analgesia on mortality and morbidity after surgery: systematic review and meta-analysis of randomized controlled trials. *Annals of Surgery*, 259(6):1056–1067, 2014.

[3] CR Broadbent, WB Maxwell, R Ferrie, DJ Wilson, M Gawne-Cain, and R Russell. Ability of anaesthetists to identify a marked lumbar interspace. *Anaesthesia*, 55(11):1122–1126, 2000.

[4] G Furness, MP Reilly, and S Kuchi. An evaluation of ultrasound imaging for identificationof lumbar intervertebral level. *Anaesthesia*, 57(3):277–280, 2002.

[5] PH Conroy, C Luyet, CJ McCartney, and PG McHardy. Real-time ultrasound-guided spinal anaesthesia: a prospective observational study of a new approach. *Anesthesiology Research and Practice*, 2013, 2013.

[6] MK Karmakar, X Li, AM-H Ho, WH Kwok, and PT Chui. Real-time ultrasound-guided paramedian epidural access: evaluation of a novel in-plane technique. *British Journal of Anaesthesia*, 102(6):845–854, 2009.

[7] Y Rajakulendran, S Rahman, and N Venkat. Long-term neurological complication following traumatic damage to the spinal cord with a 25 gauge whitacre spinal needle. *International Journal of Obstetric Anesthesia*, 8(1):62–66, 1999.

[8] Thomas Grau, Rüdiger W. Leipold, Johannes Horter, Renate Conradi, Eike O Martin, and Johann Motsch. Paramedian access to the epidural space: the optimum window for ultrasound imaging. *Journal of Clinical Anesthesia*, 13(3):213–217, May 2001.

[9] Furqan Shaikh, Jack Brzezinski, Sarah Alexander, Cristian Arzola, Jose CA Carvalho, Joseph Beyene, and Lillian Sung. Ultrasound imaging for lumbar punctures and epidural catheterisations: systematic review and meta-analysis. *BMJ: British Medical Journal*, 346, 2013.

[10] Atsushi Kimura, Atsushi Seichi, Hirokazu Inoue, Teruaki Endo, Michiyoshi Sato, Takahiro Higashi, and Yuichi Hoshino. Ultrasonographic quantification of spinal cord and dural pulsations during cervical laminoplasty in patients with compressive myelopathy. *European Spine Journal*, 21(12):2450–2455, 2012.

[11] Ce Liu, Antonio Torralba, William T Freeman, Frédo Durand, and Edward H Adelson. Motion magnification. In *ACM Transactions on Graphics (TOG)*, volume 24, pages 519–526. ACM, 2005.

[12] Hao-Yu Wu, Michael Rubinstein, Eugene Shih, John V Guttag, Frédo Durand, and William T Freeman. Eulerian video magnification for revealing subtle changes in the world. *ACM Trans. Graph.*, 31(4):65, 2012.

[13] Neal Wadhwa, Michael Rubinstein, Frédo Durand, and William T Freeman. Phase-based video motion processing. *ACM Transactions on Graphics (TOG)*, 32(4):80, 2013.

[14] Neal Wadhwa, Michael Rubinstein, Fredo Durand, and William T Freeman. Quaternionic representation of the riesz pyramid for video magnification. 2014.

[15] A Jonathan McLeod, John SH Baxter, Sandrine de Ribaupierre, and Terry M Peters. Motion magnification for endoscopic surgery. In *SPIE Medical Imaging*, pages 90360C–90360C. International Society for Optics and Photonics, 2014.

[16] Alborz Amir-Khalili, Jean-Marc Peyrat, Julien Abinahed, Osama Al-Alao, Abdulla Al-Ansari, Ghassan Hamarneh, and Rafeef Abugharbieh. Auto localization and segmentation of occluded vessels in robot-assisted partial nephrectomy. In *Medical Image Computing and Computer-Assisted Intervention–MICCAI 2014*, pages 407–414. Springer, 2014.

[17] Steven M Seitz and Charles R Dyer. View-invariant analysis of cyclic motion. *International Journal of Computer Vision*, 25(3):231–251, 1997.

[18] Ramprasad Polana and Randal C Nelson. Detection and recognition of periodic, non-rigid motion. *International Journal of Computer Vision*, 23(3):261–282, 1997.

[19] Ross Cutler and Larry S. Davis. Robust real-time periodic motion detection, analysis, and applications. *Pattern Analysis and Machine Intelligence, IEEE Transactions on*, 22(8):781–796, 2000.

[20] Alexia Briassouli and Narendra Ahuja. Extraction and analysis of multiple periodic motions in video sequences. *Pattern Analysis and Machine Intelligence, IEEE Transactions on*, 29(7):1244–1261, 2007.

[21] Yang Ran, Isaac Weiss, Qinfen Zheng, and Larry S Davis. Pedestrian detection via periodic motion analysis. *International Journal of Computer Vision*, 71(2):143–160, 2007.

[22] Erik Pogalin, Arnold WM Smeulders, and Andrew HC Thean. Visual quasi-periodicity. In *Computer Vision and Pattern Recognition, 2008. CVPR 2008. IEEE Conference on*, pages 1–8. IEEE, 2008.

[23] Ronald Aylmer Fisher. Tests of significance in harmonic analysis. *Proceedings of the Royal Society of London. Series A*, 125(796):54–59, 1929.

[24] Sergio Bittanti and Sergio M Savaresi. On the parametrization and design of an extended Kalman filter frequency tracker. *Automatic Control, IEEE Transactions on*, 45(9):1718–1724, 2000.

[25] James McNames and Mateo Aboy. Statistical modeling of cardiovascular signals and parameter estimation based on the extended Kalman filter. *Biomedical Engineering, IEEE Transactions on*, 55(1):119–129, 2008.

[26] Shelten G Yuen, Paul M Novotny, and Robert D Howe. Quasiperiodic predictive filtering for robot-assisted beating heart surgery. In *Robotics and Automation, 2008. ICRA 2008. IEEE International Conference on*, pages 3875–3880. IEEE, 2008.

[27] Dan Simon and Tien Li Chia. Kalman filtering with state equality constraints. *Aerospace and Electronic Systems, IEEE Transactions on*, 38(1):128–136, 2002.

[28] Barry G Quinn and Edward James Hannan. *The estimation and tracking of frequency*. Cambridge University Press, 2001.

[29] Elvis C. S. Chen, Golafsoun Ameri, Hao Li, Rakesh V. Sondekoppam, Sugantha Ganapathy, and Terry M. Peters. Navigated simulator for spinal needle interventions. *Studies in Health Technology and Informatics*, 196:56–60, January 2014.

[30] Abtin Rasoulian, Purang Abolmaesumi, and Parvin Mousavi. Feature-based multi-
    body rigid registration of ct and ultrasound images of lumbar spine. *Medical Physics*,
    39(6):3154–3166, 2012.

Chapter 4

Analysis of Periodicity in Video Sequences through Dynamic Linear Modeling

This chapter includes material adapted from:

A. Jonathan McLeod, Dante P.I. Capaldi, John S.H. Baxter, Grace Parraga, Xiongbiao Luo and Terry M. Peters, Analysis of Periodicity in Video Sequences through Dynamic Linear Modeling. In *"Medical Image Computing and Computer-Assisted Intervention – MICCAI 2017* [In Press].

4.1   Introduction

Analyzing quasiperiodic variations in a video sequence is frequently performed in medical imaging with the goal of extracting information related to the cardiac or respiratory cycles.

Natural video of a person's face or hand can be used for non-contact monitoring of vital signs including heart rate, respiratory rate, and pulse transit time [1, 2] or to generate maps showing the spatial distribution of tissue perfusion [3, 4]. Fourier-decomposition MRI is an emerging technique for imaging lung perfusion and ventilation that relies on Fourier analysis of a sequence of non-contrast enhanced MR images [5]. Another area where periodicity is useful in medical imaging is in the detection of critical pulsating structures in medical interventions [6, 7, 8, 9]. Most of these techniques require extensive filtering and preprocessing that have been fine-tuned for their respective problems. This is necessary to produce a sufficiently clean periodic signal that can be extracted through Fourier analysis or band-pass filtering.

In this paper we propose the use of dynamic linear modeling for analyzing periodicity in video sequences. We show how a cyclic + random walk model can be used to estimate the frequency and amplitude of quasi-periodic components. We also propose a log-likelihood ratio statistic for determining the presence of periodicity. In addition, we derive the power spectral density function for this model and show that it closely resembles that of the observed spectrum commonly found in video sequences. This approach is applied to natural video, ultrasound and MRI.

4.2   Methods

4.2.1   Dynamic Linear Models

Dynamic Linear Models (DLM) are linear state-space time series models [10] of the form,

$$y_t = Za_t + \epsilon_t, \qquad \epsilon_t \sim N(0, \Sigma_\epsilon), \qquad a_t = Ta_{t-1} + \eta_t, \qquad \eta_t \sim N(0, \Sigma_\eta), \qquad (4.1)$$

where y_t and a_t are the observation and state vectors at time t. The observation and state transition matrices are Z and T with independent normally distributed noise covariances Σ_ϵ and Σ_η. Often these are block diagonal matrices formed from several simpler models whose parameters have an intuitive or physical meaning. Maximum likelihood estimates (MLE) for unknown parameters in Z, T, Σ_ϵ and Σ_η can be obtained by numerically optimizing the log-likelihood function,

$$\log L(\theta|Y_t) = \sum \log p(y_t|Y_t, \theta), \tag{4.2}$$

where Y_t denotes the vector of observations up to time t, θ are the unknown model parameters and $p(\cdot)$ is the probability density function. Kalman filtering is used to evaluate $\log L(\theta|Y_t)$.

We propose a nested DLM to model quasi-periodicity in video sequences. This model consists of a stationary cyclic component, random walk component and additive measurement noise as specified in Equation 4.3,

$$Z = \begin{bmatrix} 1 & 0 & 1 \end{bmatrix}, \quad T = \begin{bmatrix} \rho\cos\omega_0 & \rho\sin\omega_0 & 0 \\ -\rho\sin\omega_0 & \rho\cos\omega_0 & 0 \\ 0 & 0 & 1 \end{bmatrix}, \quad \Sigma_\epsilon = \sigma_n^2, \quad \Sigma_\eta = \begin{bmatrix} \sigma_c^2 & 0 & 0 \\ 0 & \sigma_c^2 & 0 \\ 0 & 0 & \sigma_l^2 \end{bmatrix}. \tag{4.3}$$

The parameters ω_0 and ρ represent the frequency and bandwidth of the cyclic component. The variances σ_c^2, σ_l^2 and σ_n^2 specify the strength of cyclic, random walk and additive noise components respectively. In the state vector, $a_t = [a_{t,1}, a_{t,2}, a_{t,3}]^T$, the first two states, $a_{t,1}$, and $a_{t,2}$ are analogous to the real and imaginary components of a complex oscillator, while the third state, $a_{t,3}$ follows a random walk to account for signal drift and other low frequency variations. The model observation matrix, Z, adds $a_{t,1}$ and $a_{t,3}$ to obtain a cyclic model with a local level that follows a random walk.

The power spectral density of the model can be derived by breaking apart the cyclic and random walk components. Transfer functions from the cyclic component state noise $\eta_{t,1}$ and $\eta_{t,2}$ to the output y_t can be obtained directly from the state-space model:

$$G_1(z) = \frac{z - \rho \cos(\omega_0)}{z^2 - 2\rho \cos(\omega)z + \rho^2}, G_2(z) = \frac{-\rho \sin(\omega_0)}{z^2 - 2\rho \cos(\omega)z + \rho^2}, \tag{4.4}$$

where $G_1(z)$, $G_2(z)$ are the respective transfer functions and z is the forward shift operator. The power spectral density can be obtained by evaluating the transfer functions at $z = e^{j\omega}$ yielding,

$$S_{yy}^{cyclic}(\omega) = \frac{\sigma_c^2(1 + \rho^2 - 2\rho \cos \omega_0 \cos \omega)}{[1 + \rho^2 - 2\rho \cos(\omega - \omega_0)][1 + \rho^2 - 2\rho \cos(\omega + \omega_0)]}. \tag{4.5}$$

The random walk is non-stationary with a well known frequency drop-off approximately proportional to ω^{-2}. An exact expression for its power spectral density, $S_{yy}^{rw}(\omega)$, with a finite length time series can be obtained through Fourier analysis where the Fourier transform of the random walk state, $a_{t,3}$, is expressed in terms of the incremental state noise, $\eta_{t,3}$:

$$F(a_{t,3}) = \sum_{i=0}^{N} F(\eta_{i,3}H(t - i)), \tag{4.6}$$

where F is the discrete Fourier transform operator and $H(t)$ is the Heaviside function. Since $\eta_{t,3}$ are independent random variables, the power spectral density can be obtained from the expected value of Equation 4.6 as,

$$S_{yy}^{rw}(\omega) = \mathbf{E}|F(a_{t,3})|^2 = \sum_{i=1}^{N} \mathbf{E}|F(\eta_{t,3}H(t - i))|^2 = \frac{\sigma_l^2}{1 - \cos \omega}. \tag{4.7}$$

The total power spectral density for Equation 4.3 is obtained from Equations 4.5 & 4.7 plus

the white additive measurement noise,

$$S_{yy}(\omega) = \frac{\sigma_c^2(1 + \rho^2 - 2\rho\cos\omega_0\cos\omega)}{[1 + \rho^2 - 2\rho\cos(\omega - \omega_0)][1 + \rho^2 - 2\rho\cos(\omega + \omega_0)]} + \frac{\sigma_l^2}{1 - \cos\omega} + \sigma_n^2. \quad (4.8)$$

As can be seen in Figure 4.1, the power spectral density of the model slopes downward at -20dB/decade with a small peak near ω_0 corresponding to the cyclic component. This closely resembles the empirical spectrum observed in Figures 4.2 & 4.4. When $\sigma_c^2 \to 0$, the cyclic component vanishes and we are left with just the random walk and additive noise also known in structural time series as the local level model. Thus, to test for the presence of a cyclic component, we can test $\mathcal{H}_0 : \sigma_c^2 = 0$ against simple negation. Let $\hat{\theta}_0$ denote the MLE in the restricted model, $\sigma_c^2 = 0$. Then, if $\mathcal{H}_0$ is correct, the likelihood-ratio test statistic,

$$D = -2[\log L(\hat{\theta}|Y_t) - \log L(\hat{\theta}_0|Y_t)], \quad (4.9)$$

measures the relative plausibility of $\mathcal{H}_0$. We use D to test for periodically varying regions in the video.

4.2.2 Experiments

To demonstrate the effectiveness of this model, we considered three very different datasets consisting of MRI, ultrasound and natural video. The first dataset consisted of natural video of a human hand. We demonstrate how DLM can be used to estimate the frequency (heart rate) and amplitude (perfusion map) from the video. Next we apply DLM to an ultrasound video of the lumbar spine where pixels in the dura exhibit subtle pulsation. Here we use the likelihood ratio statistic, D, to test for the presence of periodicity. Finally, we consider a free-breathing lung MRI sequence where local ventilation images can also be generated
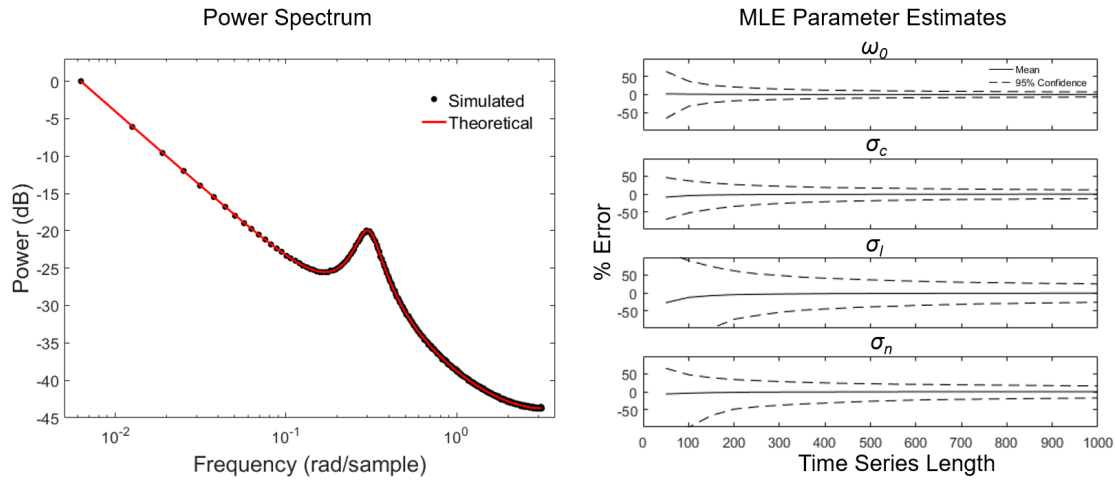
Figure 4.1: The analytic spectrum of the DLM given in Equation (4.8) and convergence of the MLE of model parameters are verified through numerical simulations. These graphs are shown for $\omega_0 = 0.3$, $\rho = 0.95$, $\sigma_c / \sqrt{(1 - \rho^2)} = 5\sigma_l = 5\sigma_n$
.

from DLM.

4.3   Results

4.3.1   Natural Video

The photoplethysmogram (PPG) is an optical measurement of cardiac activity. While infrared light is typically used in pulse oximeters due to better tissue penetration depth, the ubiquity of digital cameras has led to increasing interest in monitoring vital signs using ambient visible light. These systems have the advantage of monitoring vital signs remotely without requiring carefully controlled lighting or any direct contact with the patient. Methods have been proposed to extract heart rate, respiratory rate, and pulse transit time from videos of a person's face or hand [1, 2]. Beyond simply measuring vital signs, it is also possible to generate spatial maps showing variations in the magnitude of the PPG signal

[3, 4]. PPG imaging has the potential to show tissue perfusion relevant to many clinical problems such as evaluating skin-flaps and burn injuries. These techniques typically require extensive preprocessing to detrend the PPG signal and remove the effects of motion or variations in ambient light. For this experiment 8 videos were acquired showing the hands of seven subjects. Videos 1& 2 were acquired of the same subject to demonstrate perfusion mapping. The hand was gently scratched between these aquisitions to stimulate blood flow. This test has been previously used for perfusion mapping techniques based on PPG imaging [3] and laser Doppler imaging[11].

First, we demonstrate that heart rate can be estimated from all 8 videos. A PPG signal was extracted by averaging the green channel intensity over a 400x400 block as shown in Figure 4.2. The proposed DLM was fit to the PPG signal and the estimate of ω_0 compared with the Fourier spectral peak and the readings from the pulse oximeter (Table 4.1). The absolute error between DLM frequency estimation and the nearest pulse oximeter reading was 2.3 ± 1.0 bpm (mean $\pm$ standard error). This was significantly lower ($p < 0.05$) than the estimates through simple Fourier analysis or quadratic peak interpolation (QPI) of the spectral peak, which were 5.4 ± 1.3 and 3.8 ± 1.4 respectively.

Next, to generate perfusion maps, the DLM is fitted on a per pixel level for videos 1&2. Here, the amplitude of the cyclic component corresponds to perfusion. The original 1080x1920 videos were reduced to 135x240 by applying a Gaussian blur with $\sigma = 8$ and a

Table 4.1: Heart rate estimated from the eight video clips (bpm)

	1	2	3	4	5	6	7	8	Abs Err
DLM	84 .1	79.6	86.6	89.1	73.6	78.5	55.1	63.3	2.3 ± 1.0
Fourier	84.0	72.0	84.0	84.0	72.0	84.0	60.0	60.0	5.4 ± 1.3
QPI	82.7	76.4	83.7	86.9	70.7	82.8	55.7	63.1	3.8 ± 1.4
Pulse Ox.	84	82	94-98	90-91	79	80-81	56	63-65	
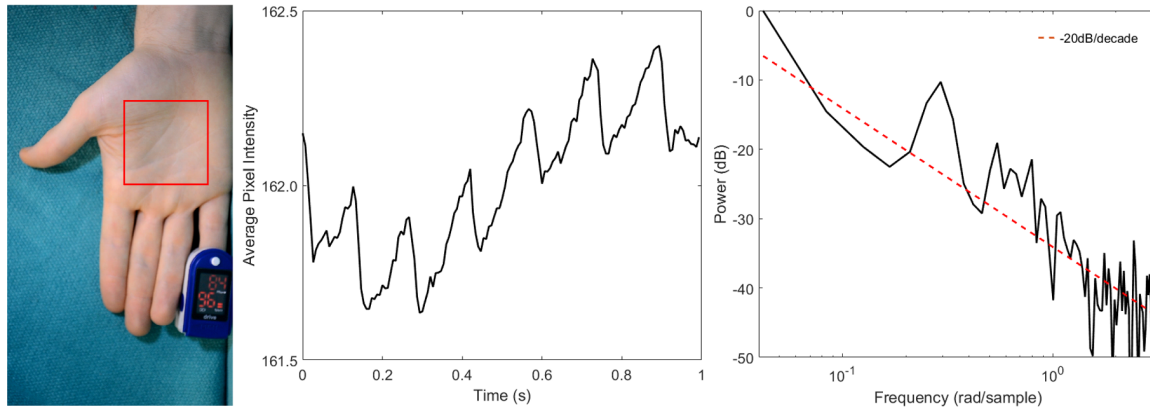
Figure 4.2: Video clips were recorded of the subjects' hands and the PPG signal was calculated from the average intensity over the 400x400 box. The -20dB/decade slope observed in the spectrum is consistent with the proposed DLM.

down-sampling factor of 8. The DLM was fit with the frequency fixed to the MLE estimate given in Table 4.1. The quantity $\sigma_c/(\sqrt{1-\rho^2})$, corresponding to the amplitude of the cyclic component, is shown in Figure 4.3. For comparison, the Fourier estimates of amplitude are also shown.

Without any preprocessing or tuning for this specific problem, a relatively simple DLM was able to identify very subtle changes in tissue perfusion that occurred after gently scratching the hand. Furthermore, this was accomplished with very short video clips only 5 seconds in length unlike previous methods that required much longer video clips and extensive preprocessing and detrending.

4.3.2   Ultrasound

Dural pulsation is a valuable cue in ultrasound guided epidural injections. Previously, McLeod et al.[8] proposed an extended Kalman filtering (EKF) method that estimated frequency and amplitude of the pulsating dura on a per-pixel basis in lumbar spine ultrasound. Here, our main objective is to identify which pixels in the image exhibit periodicity. The
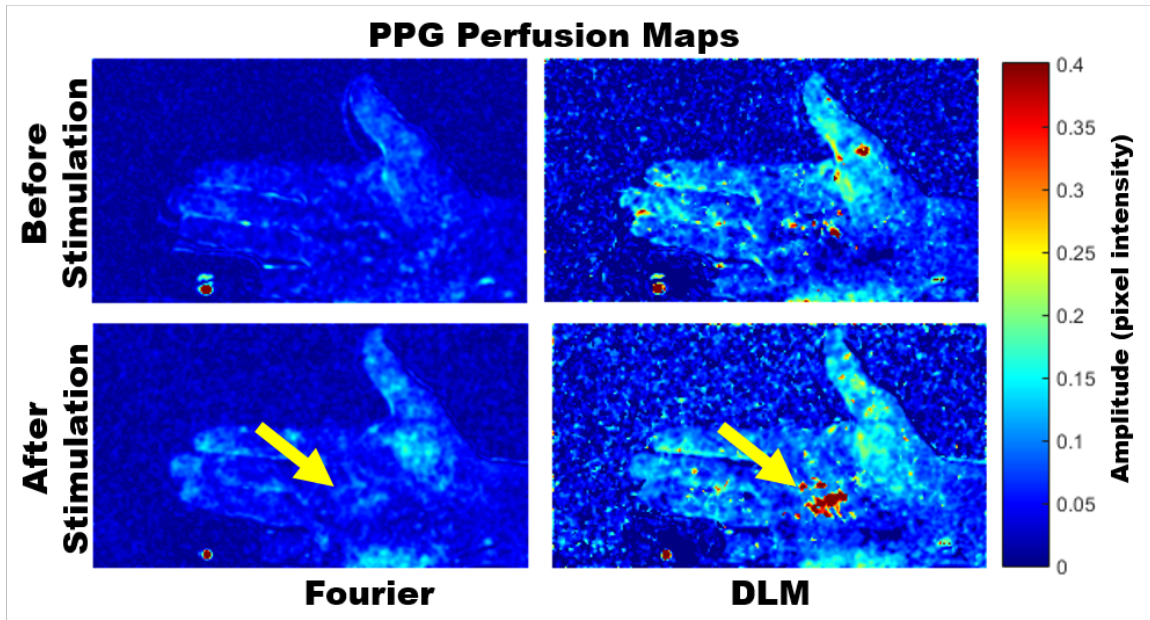
Figure 4.3: PPG imaging using Fourier analysis and DLM. The yellow arrow indicates where the hand was scratched.

likelihood-ratio statistic in Equation 4.9 is ideal for this purpose. We fit the proposed DLM on a per-pixel basis to a video of the lumbar ultrasound and compared it against those obtained from the EKF method in McLeod et al [8]. The results are nearly identical despite the EKF having being developed for this application only, and requiring extensive smoothing and tight thresholds on the frequency and amplitude (Figure 4.4).

4.3.3   MRI

Fourier-decomposition of free-breathing proton MRI (FDMRI) has recently emerged as a non-contrast enhanced MRI technique to generate regional pulmonary ventilation maps on any clinically available MRI system [5, 12]. This technique exploits fast pulmonary MRI acquisition and non-rigid image registration to acquire a time series of registered proton MR images. Since the proton density within lung tissue varies with the respiratory cycle as
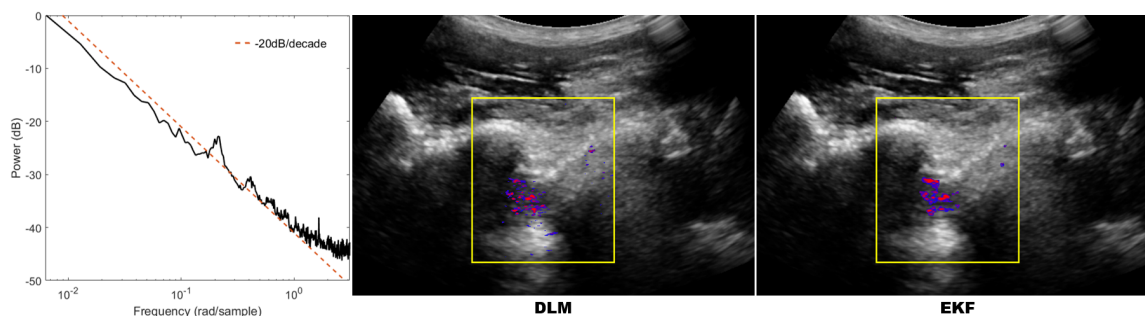
Figure 4.4: The average power spectrum of the lumbar ultrasound ROI exhibits an approximately -20dB/decade slope with a small peak at the cardiac frequency, closely resembling the theoretical DLM spectrum in Figure 4.1. The likelihood ratio estimated from the DLM immediately reveals the location of the dural pulsation. The results are very similar to the hand-crafted EKF method [8].

the aveoli expand and contract, periodicity in the signal intensity of the registered images provides a measure of tissue ventilation. In FDMRI, the amplitude of the Fourier component at the respiratory frequency is used as a measure of lung ventilation. We acquired a dynamic free-breathing MRI of a non-small cell lung cancer patient over 125 seconds at a rate of 4 frames per second where the left lung was obstructed and poorly ventilated. A hyperpolarized ^{129}Xe MR static ventilation image was acquired as a benchmark and shows a lack of ventilation in the left lung. The DLM was fit to the MRI sequence (Figure 4.5). The DLM amplitude map was visually similar to FDMRI, but with slightly better rejection of background tissue motion. The likelihood-ratio statistic provided a statistical test for the presence of ventilation. It showed a lack of ventilation in the left lung, only exhibiting motion artifacts around the lung boundary and was qualitatively closest to the ^{129}Xe MRI.
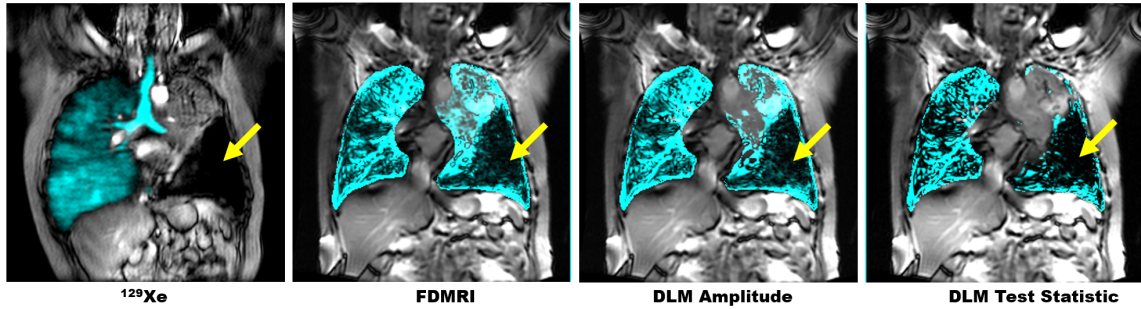
Figure 4.5: The benchmark ^{129}Xe MR image is compared with FDMRI and the two DLM images (amplitude, and likelihood-ratio). The cyan overlays display the ventilation maps and the yellow arrows point to the lack of ventilation in the left lung. Of the three images generated from the free-breathing sequence, the DLM likelihood-ratio appears most similar to the ^{129}Xe MR image.

4.4   Discussion and Conclusion

We have shown how DLM provides a powerful framework for analyzing periodicity in various video sequences. The same DLM was applied directly to natural video, ultrasound and MRI without additional preprocessing or fine-tuning and it provided frequency and amplitude estimates, as well as log-likelihood statistic testing for the presence of periodicity. The main strength of this model is that it provides a general method for analyzing periodicity in video sequences that typically require individually handcrafted techniques. In addition, DLM can easily be extended to include multiple frequencies and harmonics, as well as more advanced background noise models.

Bibliography

[1] Ming-Zher Poh, Daniel J McDuff, and Rosalind W Picard. Advancements in non-contact, multiparameter physiological measurements using a webcam. *Biomedical Engineering, IEEE Transactions on*, 58(1):7–11, 2011.

[2] Dangdang Shao, Yuting Yang, Chenbin Liu, Francis Tsow, Hui Yu, and Nongjian Tao. Noncontact monitoring breathing pattern, exhalation flow rate and pulse transit time. *Biomedical Engineering, IEEE Transactions on*, 61(11):2760–2767, 2014.

[3] Alexei A Kamshilin, Serguei Miridonov, Victor Teplov, Riku Saarenheimo, and Ervin Nippolainen. Photoplethysmographic imaging of high spatial resolution. *Biomedical Optics Express*, 2(4):996–1006, 2011.

[4] Wim Verkruysse, Lars O Svaasand, and J Stuart Nelson. Remote plethysmographic imaging using ambient light. *Optics Express*, 16(26):21434–21445, 2008.

[5] Grzegorz Bauman, Michael Puderbach, Michael Deimling, Vladimir Jellus, Christophe Chefd'hotel, Julien Dinkel, Christian Hintze, Hans-Ulrich Kauczor, and Lothar R Schad. Non-contrast-enhanced perfusion and ventilation assessment of the human lung by means of Fourier decomposition in proton MRI. *Magnetic Resonance in Medicine*, 62(3):656–664, 2009.

[6] Alborz Amir-Khalili, Ghassan Hamarneh, and Rafeef Abugharbieh. Automatic vessel segmentation from pulsatile radial distension. In *Medical Image Computing and Computer-Assisted Intervention–MICCAI 2015*, pages 403–410. Springer, 2015.

[7] Alborz Amir-Khalili, Ghassan Hamarneh, Jean-Marc Peyrat, Julien Abinahed, Osama Al-Alao, Abdulla Al-Ansari, and Rafeef Abugharbieh. Automatic segmentation of

occluded vasculature via pulsatile motion analysis in endoscopic robot-assisted partial nephrectomy video. *Medical Image Analysis*, 25(1):103–110, 2015.

[8] A Jonathan McLeod, John SH Baxter, Golafsoun Ameri, Sugantha Ganapathy, Terry M Peters, and Elvis CS Chen. Detection and visualization of dural pulsation for spine needle interventions. *International journal of computer assisted radiology and surgery*, 10(6):947–958, 2015.

[9] A Jonathan McLeod, John SH Baxter, Sandrine de Ribaupierre, and Terry M Peters. Motion magnification for endoscopic surgery. In *SPIE Medical Imaging*, volume 9036, pages 90360C–1–8, 2014.

[10] James Durbin and Siem Jan Koopman. *Time series analysis by state space methods*. Oxford University Press, 2012.

[11] J David Briers. Laser doppler, speckle and related techniques for blood perfusion mapping and imaging. *Physiological Measurement*, 22(4):R35–R66, 2001.

[12] Dante PI Capaldi, Khadija Sheikh, Fumin Guo, Sarah Svenningsen, Roya Etemad-Rezai, Harvey O Coxson, Jonathon A Leipsic, David G McCormack, and Grace Parraga. Free-breathing pulmonary ^{1}H and hyperpolarized ^{3}He MRI: Comparison in COPD and bronchiectasis. *Academic Radiology*, 22(3):320–329, 2015.

Chapter 5

Microvasculature Segmentation from B-mode Ultrasound Video Sequences

This chapter includes material adapted from:

A. Jonathan McLeod, Matthew R. Lowerison, Mai Elfarnawany, Sugantha Ganapathy, Ashley Makela, Hon S. Leong, James C. Lacefield, and Terry M. Peters. Microvasculature Segmentation from B-mode Ultrasound Video Sequences. *Ultrasound in Medicine and Biology* [In Preparation]

5.1   Introduction

Power Doppler ultrasound is frequently used to assess the efficacy of anti-angiogenic drugs in preclinical studies as it can image microvasculature *in vivo* without requiring contrast agent [1, 2]. In these studies, the color pixel density (CPD) can be used as a proxy for the fractional blood volume within the region of interest [3]. This metric is the ratio of pixels

104

identified as having blood flow to the total number of pixels within a region of interest and is also referred to as the vascularization index. To prevent background tissue from being erroneously identified as blood, the sonographer sets the clutter or wall filter cut-off frequency to reject slow moving tissue. However, tuning the clutter filter to reject artifacts while showing small, low-flow microvasculature is challenging and must be done consistently throughout the entire study to avoid introducing observer bias. Small vessels missed by Doppler ultrasound are often visible in the original B-mode video, but are difficult to quantify.

Another approach is to process the B-mode ultrasound images directly. When a series of B-mode images is acquired by recording a video or cine loop, the B-mode intensity values are temporally decorrelated in blood due to the erythrocytes moving with the blood flow. Previously, Rubin et al. [4] proposed a method for estimating 3D flow vectors and volume flow measurements from B-mode. This approach fitted a Gaussian function to the empirical autocorrelation coefficients estimated from the B-mode image sequence and used the anisotropic beam correlation width together with the in-plane 2D velocity estimated through speckle tracking or conventional Doppler to estimate the 3D velocity vector. This approach requires the spatially varying 3D beam correlation width to be characterized, the log-compression during scan conversion to be inverted and is effective only at high frame rate.

Yang et al. [5] developed speckle variance flow processing as a simpler technique based on the variance of the B-mode intensity values with respect to time. Assuming static background tissue, pixels exhibiting a high variance time-series correspond to moving blood. They also proposed a real-time alternative where instead of calculating the variance explicitly, the absolute first differences of the time series could be filtered to give a speckle

flow index (SFI). Using a flow phantom vessel 1 mm in diameter and 30 frames per second (fps) B-mode imaging, the SFI was found to exhibit a nearly linear relation with blood velocity up to velocities of 2 mm/s after which point it became saturated [5, 6]. These methods for B-mode processing have focused on obtaining velocity estimates of slowly moving blood with static background tissue and were validated in phantoms where these conditions could be achieved. *In vivo*, much of the relevant microvasculature is smaller than the 1 mm vessel phantoms, significant background motion is present and, in many cases, blood flow is too fast relative to the imaging frame-rate to obtain measurable auto-correlation in B-mode signal. While Cheung et al. [7] used speckle variance flow processing approach to assess tumor microvasculature *in vivo*, they thresholded the SFI, using it as a flow detector, and took the ratio of pixels where blood flow was detected within the tumor as a metric of vascularization, analogous to CPD metrics in Doppler studies. In this chapter we focus solely on microvasculature detection and segmentation, which can be used to compute vascularization metrics similar to CPD. Towards this end we use Bartlett's test statistic to distinguish between blood and background tissue by measuring how closely their cumulative periodograms resemble that of an uncorrelated time series. This technique tests for regions where the B-mode pixel values are temporally decorrelated indicative of blood flow. Our proposed method is validated in a chick embryo chorioallantoic membrane (CAM) model, commonly used for angiogenesis studies [8]. Receiver operating characteristic (ROC) curves are used to compare the B-mode segmentation to power Doppler imaging on well defined small vessels and qualitative comparison is performed on microvasculature segmentations in ten tumor xenografts. In addition, it can be used to help declutter traditional power Doppler imaging by removing some of the false positives caused by background tissue motion.

5.2 Methods

5.2.1 Bartlett's Cumulative Periodogram Test

Speckle in images of blood flowing farther than the beam correlation width between frames is effectively decorrelated. For B-mode video, this typically occurs between 1–2 mm/s depending on the ultrasound probe resolution and B-mode video frame rate.

In the CAM model the blood velocity of vessels of this size is considerably higher [9]. As a result, the intensity values of a pixel within a vessel closely resembles white noise with a very flat spectrum. However, background tissue moving more than the speckle width can exhibit similar variance but with a very different spectrum. In the CAM models used in this study, periodic motion induced by the cardiac cycle, spontaneous muscle movement and low velocity flow within the albumen all result in large background motions. To separate background tissue from blood flow, we propose using Bartlett's test for white noise [10]. This is accomplished by computing the cumulative periodogram of the B-mode log-compressed intensity on a pixel-by-pixel basis. The Kolmogorov-Smirnov statistic is then used to compare the observed cumulative periodiogram to the theoretical cumulative periodogram for a serial uncorrelated time series.

The periodogram, $f(\omega)$, of a time series $x_t : t = 1, ..., N$ evaluated at the Fourier frequencies $\omega = 2\pi k/M$ for $k = 1, ..., M$, $M = \lfloor (N-1)/2 \rfloor$ is

$$f(\omega) = \frac{|\sum_{t=1}^{N} x_t e^{i\omega t}|^2}{2\pi N}. \tag{5.1}$$

The normalized cumulative periodogram, $F(\omega)$, is given by:

$$F(\omega_k) = \frac{\sum_{j=1}^{k} f(\omega_j)}{\sum_{j=1}^{M} f(\omega_j)}, \tag{5.2}$$

If x_t is serially uncorrelated, its theoretical cumulative periodogram is simply, $F_{null}(\omega_k) = \frac{k}{M}$. The test statistic, D, measures the distance between observed periodogram and this result:

$$D = \sqrt{M} \sup_{\omega} |F(\omega) - F_{null}(\omega)|, \tag{5.3}$$

where sup is the supremum. Under the null hypothesis D asymptotically converges to the Kolmogorov distribution.

5.2.2   Blood-flow Segmentation from B-mode Video Sequences

Using Bartlett's test statistic, we can distinguish between blood flow and background tissue motion in a short B-mode video. Figure 5.1 shows Bartlett's test applied to a five second, 20 fps B-mode video clip of a CAM tumor xenograft. As an example, the cumulative periodograms for a pixel within the tumor's microvasculture and background tissue are shown in Figure 5.1b. While the cumulative spectrum of blood closely resembles the theoretical result for white noise, so do the very low signal regions of the background which are dominated by electronic noise. A map of the test statistic, D, (Figure 5.1c) shows the microvasculature inside the tumor mass, the feeder vessels as well as a large artery. However, much of the low intensity background is also detected. This background can be removed by thresholding out the low intensity background to only keep soft tissue.

The scatter plot in Figure 5.2 shows that together, the test statistic, D, and mean intensity, μ, separate blood and background tissue with a large margin. Furthermore, many
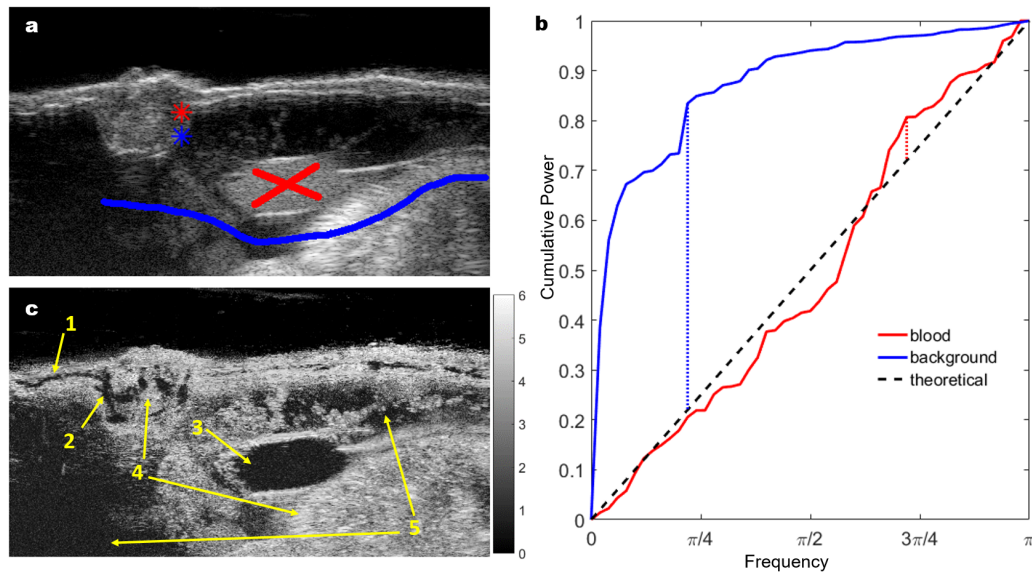
Figure 5.1: Bartlet's whiteness test for identifying blood flow. (a) One frame from five second B-mode video sequence. To illustrate the computation of the test statistic using cumulative periodograms, two pixels were chosen in the tumor, one where blood flow appeared to be present in the B-mode sequence marked by the red asterisk, and the other in background tissue marked by the blue asterisk. The cumulative periodogram at these locations are shown in (b). The red and blue brushstrokes show the blood and background pixels used for the scatter plots in Figure 5.2. The blood pixels here come from a larger vessel so as not to depend on the accuracy of a very challenging segmentation of the microvasculature. (b) The cumulative power spectral density with the dotted line denoting the maximum deviation from the theoretical distribution of independent noise from which the test statistic (D) is computed. (c) A map of the the test statistic, D. (1) A small vessel feeding the tumor (2), the tumor microvasculature (3), and a larger, short-axis vessel all exhibit low values of D indicating blood flow. (4) High values of D are present where background tissue was visible in the original B-mode. However, regions of the background with very low B-mode intensity also have low values of D, despite having no blood flow present (5).

background pixels exhibiting sufficient motion have a similar variance to flowing blood. Simply looking at the mean and standard deviation of the pixel time-series was insufficient to separate blood from background tissue.
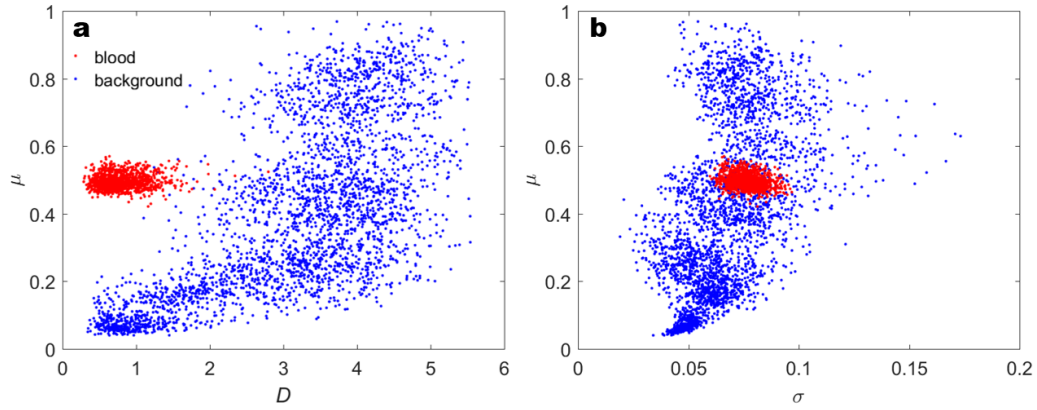
Figure 5.2: Scatter plots of the test statistic, D, the mean, μ, and the standard deviation, σ, of the image intensity taken from the blood and background as sampled in Figure 5.1. There is a large margin between the blood and background pixels in (a), indicating that D and μ together can be used to separate blood from background. On the other hand, (b) shows that variance and mean intensity of blood pixels are within the range exhibited by background tissue.

To generate a binary mask of the blood flow, simple thresholding of D and μ is applied:

$$B(x, y) = (D(x, y) < D_{th}) \wedge (\mu(x, y) \geq \mu_{th}), \qquad (5.4)$$

where D_{th} and μ_{th} are the thresholds on D and μ respectively and $\wedge$ is the and operator. This mask can further be refined by removing isolated pixels and holes. In this study we removed connected components with areas less than nine pixels (3×10^{-3} mm^2). Since the pixels in the B-mode images are sampled at a much higher density than the spatial resolution, neighbouring pixels were highly correlated and this processing removed the effects of an isolated error.

5.2.3 Vessel Images

To evaluate the proposed method for B-mode blood flow segmentation a series videos of CAM vessels were acquired in an ex-ovo chicken embryo. Each sequence was five seconds in length with a frame rate of twenty frames per second and showed clear, unambiguous vasculature within the region of interest (ROI) that was manually segmented. The first image sequence is dominated by a long axis vessel just under 1 mm in diameter. Several smaller long and short axis vessel segments are also visible within the ROI and ranged in size from 60–420 μm. The second image sequence contains a short axis view of an artery and a vein, each approximately 0.75 mm in diameter, as well as several smaller vessels. The image sequence shows more complex vascularization, including vessel bifurcations and vessels of various sizes and orientations. ROC analysis was performed for both the proposed B-mode flow detection and conventional power Doppler using manual vessel segmentation as the gold standard.

A 40 MHz micro-ultrasound imaging system (MS-550D probe attached to a Vevo 2100 system, FujiFilm VisualSonics Inc., Toronto, ON, Canada) was used to acquire the beam-formed, quadrature demodulated (IQ) echo signals from which the Doppler and B-mode image sequences were reconstructed. This approach ensured that the B-mode and power Doppler images were acquired simultaneously and allowed the Doppler clutter filter and color gain to be tuned retrospectively. A conventional reconstruction pipeline was implemented for B-mode and Doppler image processing. The B-mode image sequence was reconstructed from the background IQ data using Hilbert transform envelope detection followed by log compression. The power Doppler IQ data were acquired with 11 pulse repetitions per frame and a third order Chebychev I clutter filter was applied with step initialization. The power was averaged across all 100 frames, making use of the 5 second

video to improve the signal to noise ratio in the Doppler images. Blood segmentations were obtained from the Doppler by applying a threshold, P_{th}, to the power of the filtered signal. In this processing pipeline, adjusting the cut-off frequency, f_c, and power threshold, P_{th}, corresponds to adjusting the wall filter and Doppler gain settings on the scanner.

The values of (D_{th}, μ_{th}) in the B-mode segmentation and (f_c, P_{th}) in Doppler processing determine the trade-off between the sensitivity and specificity of the segmentation methods. Each parameter set defines a classifier for which the true positive rate (TPR) and false positive rate (FPR) can be calculated and corresponds to a point in ROC space. The convex hull of these points defines a curve through ROC space representing optimal classification [11] and the area under the curve (AUC) provides a metric for comparing the performance of the two methods.

5.2.4 Tumor Xenografts

The second experiment qualitatively compared the B-mode processing to power Doppler in ten videos of tumor xenografts in a CAM model. These images were acquired as part of a larger study to perform drug paneling of first-line anti-angiogenic therapies on patient-derived renal cell carcinoma cell-lines. The tumor samples were obtained from patients that provided oral and written consent to a University of Western Ontario Research Ethics Board approved protocol (REB #104278), allowing for the use of surgical specimens for research at the London Health Sciences Centre. In this study the Doppler and B-mode data were acquired sequentially with the probe clamped between acquisitions. A Doppler window, 4.4 mm by 7.0 mm in dimension, was positioned over the tumor xenografts. B-mode processing was performed on short video clips 51-100 frames in length at 20 fps.

This approach used the machine's built-in processing with both the Doppler and B-

mode settings set by an expert sonographer prior to the beginning of the study, producing higher quality video than realized through our IQ reconstruction pipeline. Our segmentations are fairly robust to B-mode threshold parameters and $D_{th} = 2$ and $\mu_{th} = 0.2$ were chosen for all images in this study. The scanner's wall filter and Doppler gain settings were set by the expert sonographer and have a similar function to that of P_{th} and f_c from the previous experiment. The tumor microvasculature was much more difficult to manually segment than the vessel images in the previous section. In addition, despite the probe being clamped, the sequential nature of the acquisitions resulted in small shifts in the imaging plane between the B-mode and Doppler images, preventing perfect alignment between them. For these reasons, we performed a qualitative evaluation of the vasculature observed in B-mode and Doppler.

5.2.5   Doppler Decluttering using B-mode Data

While the main focus of this chapter is on obtaining blood segmentations solely from B-mode data, Doppler and B-mode processing are not mutually exclusive. The proposed B-mode processing could also be helpful in decluttering difficult Doppler videos. A full segmentation is not required for this purpose, rather, the statistic D can be used directly to ensure that pixels exhibiting correlation in the B-mode intensities are not assigned a color value. This was accomplished by incorporating a threshold of $D < 0.2$ into the color pixel priority mask of a power Doppler acquisition.

5.3   Results

5.3.1   Vessel Images

The results of the ROC analysis are shown in Figure 5.3. The AUC for Doppler imaging was 0.97, 0.93, 0.96 for the long axis, short axis, and complex vessel images respectively. These results are very similar to values reported in the literature for using power Doppler to classify blood in microvascular ultrasound. For comparison, Pinter et al. [12] performed ROC analysis on power Doppler of phantom vessels and found AUC ranging from 0.94 for high vascularity phantom images with blood velocities between 1.35-2.4mm/s to 0.99 for low vascularity phantom images with blood velocity between 5.4–9.5 mm/s. Furthermore, this study was performed in phantom images where background motion was minimal and vessel geometry was simplified to consist of tubes.

The B-mode approach consistently out-performed Doppler with AUC of 0.99, 0.99, 0.97 for the three vessel images. These improvements were statistically significant ($p <$ 0.05) under a block boot-strap test. To visually compare the B-mode and Doppler methods we show the microvascular segmentations obtained at a FPR=2.5% in Figure 5.4. Power Doppler flow detection is sensitive to blood velocity and the clutter filter cut-off frequency must be tuned high enough to reject clutter but still detect low-flow regions. As a result, several of the small vessels are not visible in the Doppler image (classified as false negatives) and motion artifacts are still visible in echogenic background tissue. In addition, Doppler had difficulties where there were large variations in blood velocity or direction. In the long-axis image sequence, the boundary between the upper and lower vessel sections is segmented poorly, while in the short-axis image, the artery had much higher blood velocities than the neighboring vein and appeared much larger in Doppler despite the two vessels
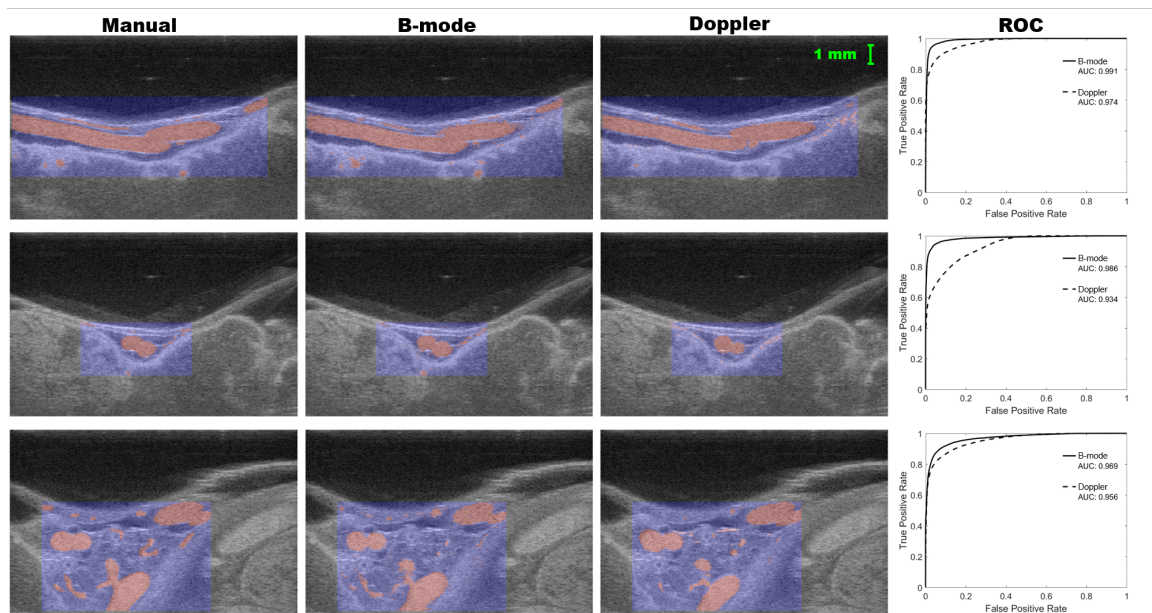
Figure 5.3: ROC analysis of B-mode and Doppler vessel images sequences. The manual segmentation of the long-axis, short-axis and complex vessel images are shown in the leftmost column. The B-mode and Doppler segmentation parameters were adjusted to calculate the ROC curves shown in the rightmost column. The manual, B-mode and Doppler segmentations are shown with red indicating blood and blue indicating background. The segmentations from B-mode and Doppler are shown in the middle two columns at the operating point on the ROC curve with a 2.5% false positive rate. The ROI from these images are enlarged and compared against the manual segmentations in Figure 5.4.

being of similar size. Finally, in the complex vessel images, much of the detail around vessel bifurcations was lost in Doppler but still visible through B-mode processing.

5.3.2   Tumor Xenografts

The results from the ten xenograft images are shown in Figure 5.5. Overall, the B-mode and Doppler were in close agreement as to the location of major vessels and most of the microvasculature. In four of the cases, B-mode revealed significantly more detail in the tumor microvasculature. It is also worth noting that, in B-mode, the blood segmentations of medium and large sized vessels were neatly contained within their vessel walls. This is very difficult to achieve in Doppler and most of the larger vessels exhibited blooming well beyond the vessel walls. Furthermore, motion artifacts adversely affected Doppler, with three of the images showing substantial false positive regions in the background tissue surrounding the tumor.

5.3.3   Doppler Decluttering using B-mode Data

A power Doppler acquisition with and without D incorporated into the color pixel priority mask is shown in Figure 5.6. As expected, the major vessels appear identical since the same power Doppler processing was performed in each vessel. However, some areas in the background, especially along tissue boundaries and vessel walls, produced a strong Doppler signal. The extent of these false positives was reduced by rejecting pixels that display correlation in their B-mode intensity values.
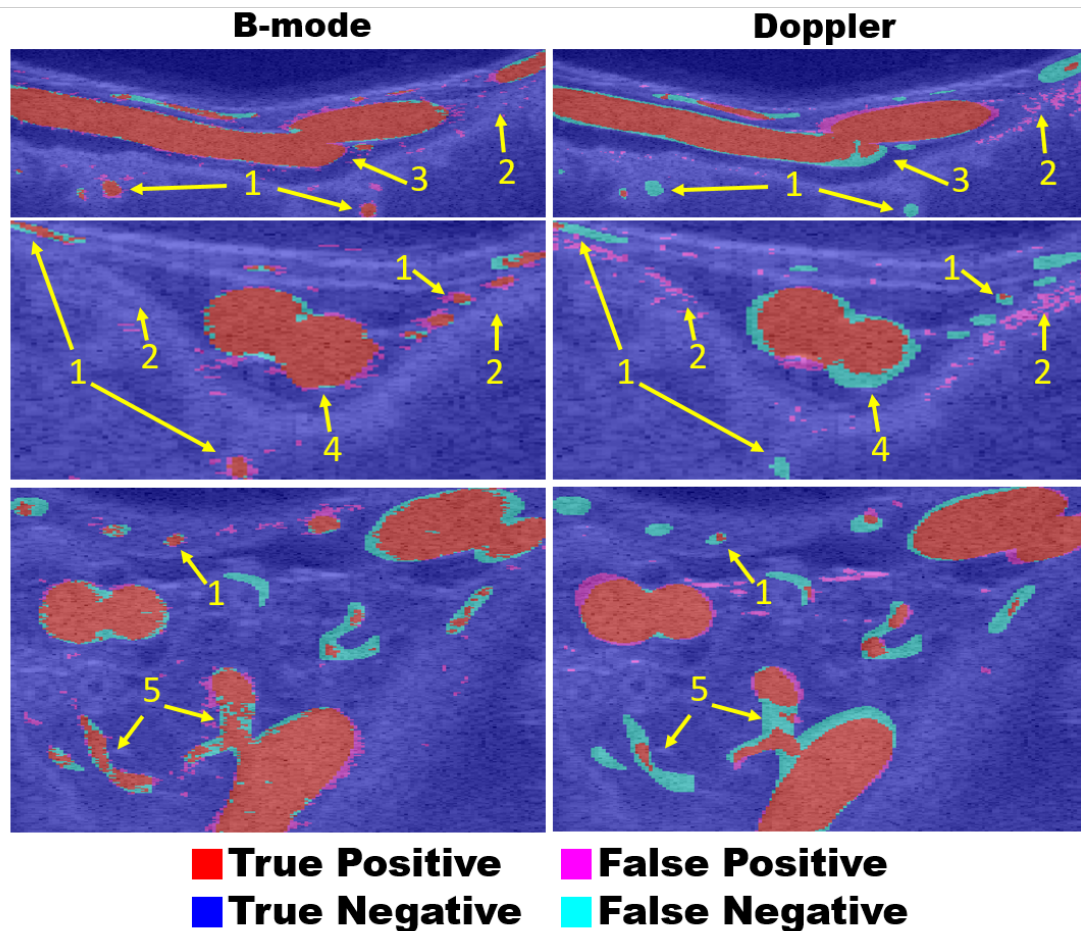
Figure 5.4: Comparison of B-mode and Doppler to the manual segmentations. The ROI from Figure 5.3 are enlarged and the manual segmentations are used as ground truth for the long axis (top row), short axis (middle row) and complex (bottom row) image sequences. In these images note that (1) many of the smaller vessels are visible in the B-mode segmentation but are missing and show as false negatives in the Doppler segmentation. (2) Motion artifacts result in false positives in the echogenic tissue surrounding the vessels in Doppler. (3) The area where the two main long axis segments meet is better shown in B-mode while in Doppler this region has larger false positive and false negative areas. (4) In Doppler, the short-axis vein appears substantially smaller than the neighbouring artery. Both vessels were of similar size but with different blood velocities. The B-mode method results were closer to the manual segmentations and showed similar size for the two vessels. (5) B-mode was better able to preserve vessel bifurcations in the complex vasculature image.
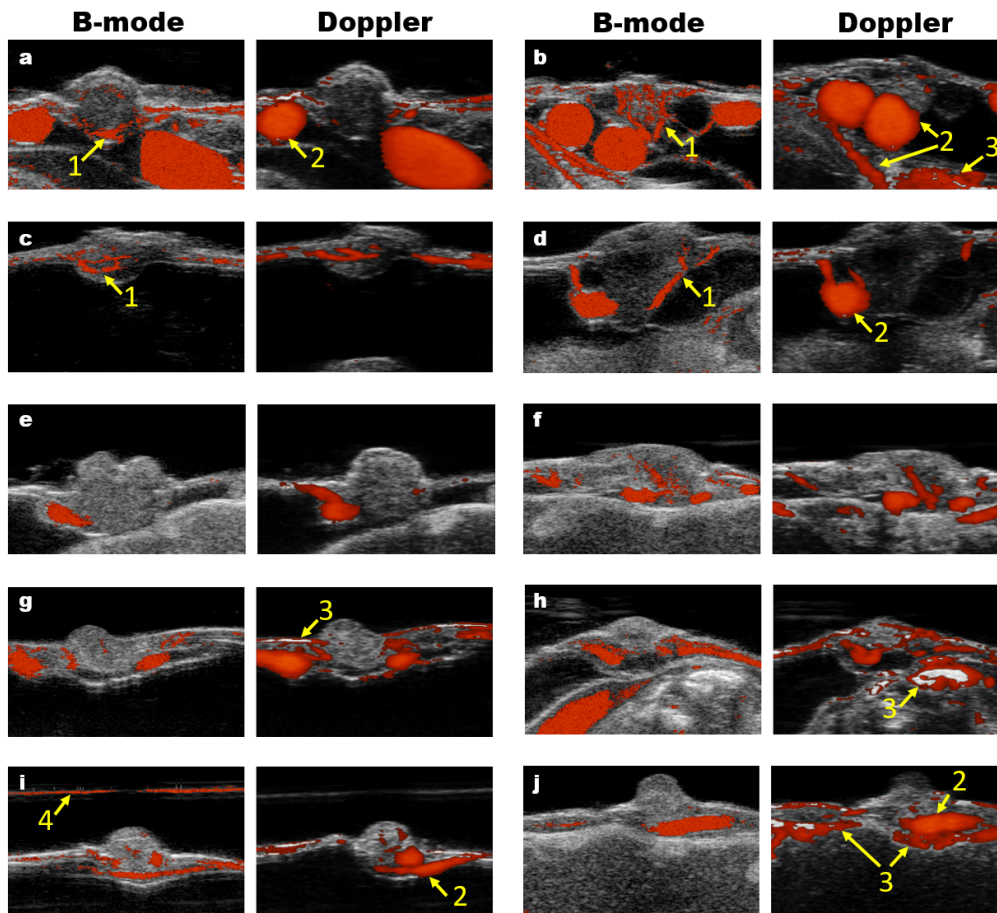
Figure 5.5: Qualitative comparison of vasculature in B-mode and Doppler images on ten CAM tumor xenografts. Each ROI is 4.4 mm by 7.0 mm in size and was defined by the Doppler processing box placed over the tumor. Note that (1) subtle microvasculature missed by Doppler is detected through B-mode processing. (2) Doppler imaging of the larger vessels exhibits blooming while in the B-mode the segmented blood is neatly contained within the vessel walls. (3) Highly echogenic tissue sometimes produces motion artifacts in Doppler that cause it to be falsely classified as blood. (4) One of B-mode images was corrupted by a scanning artifact that affected the CAM surface but the tumor itself was not compromised and showed microvasculature agreeing with Doppler. In four of the videos (a-d) substantially more detail was detected in the tumor microvasculture using the B-mode processing. Additionally, in two of the videos (h,j), Doppler suffered from severe motion and blooming artifacts near the tumor mass, which could result in poor estimates of vascularization. The microvasculature inside the tumor in the remaining four videos was qualitatively similar, with B-mode processing tending to show slightly more detail in the smaller microvasculature and less blooming from the larger vessels.

Original   **B-mode Decluttering**
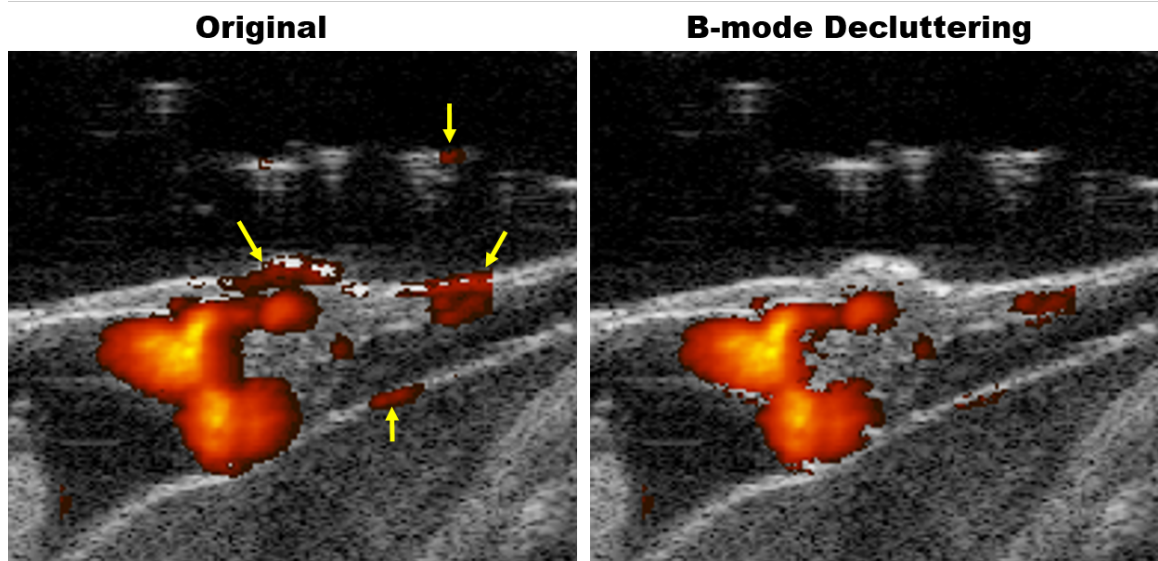
Figure 5.6: Decluttering power Doppler using B-mode video data. A threshold, $D < 0.2$, was incorporated into the color pixel priority mask to better reject motion in the vessel walls, CAM surface and background tissue (yellow arrows).

5.4 Discussion

Two sets of experiments were performed on CAM models to demonstrate the effectiveness of the B-mode processing method. In the quantitative experiments on vessel images the B-mode and Doppler were reconstructed from the IQ data, allowing all processing for both methods to be performed retrospectively. This enabled the ROC analysis to objectively compare B-mode and Doppler processing independent of how the tuning parameters are set. While the Doppler processing produced good results of a quality similar to that reported in the literature, the B-mode processing resulted in a substantial improvement, both quantitatively in terms of AUC in the ROC analysis and qualitatively providing better visibility of small low-flow vessels, more consistent visualization of vessels with differing flow rates or directions, and better rejection of motion in the background tissue. These qualitative observations were confirmed in ten sets of tumor xenograft images obtained from a

preclinical study. In addition, this type of B-mode processing can easily be combined with traditional power Doppler to help reject clutter. This is especially helpful in the vessel walls where a strong auto-correlated signal is present.

5.5 Conclusion

We proposed a processing method that, when applied to B-mode ultrasound images, can distinguish between the flowing blood in microvasculature and background tissue. This method was robust to background tissue motion and substantially outperformed Doppler in a series of *in vivo* vessel and tumor images from a CAM model. Processing short 5 second video clips revealed more detailed vasculature with less clutter from background motion than conventional power Doppler and is easily incorporated into the workflow of preclinical studies. This could improve preclinical studies on anti-angiogenic drugs, including anti-VEGF agents, by providing better blood segmentations for quantifying tumor vascularity.

Bibliography

[1] F Stuart Foster, John Hossack, and S Lee Adamson. Micro-ultrasound for preclinical imaging. *Interface Focus*, page rsfs20110037, 2011.

[2] Katherine W Ferrara, Christopher RB Merritt, Peter N Burns, F Stuart Foster, Robert F Mattrey, and Samuel A Wickline. Evaluation of tumor angiogenesis with US: imaging, Doppler, and contrast agents. *Academic Radiology*, 7(10):824–839, 2000.

[3] Arthur C Fleischer, Walter E Wojcicki, Edwin F Donnelly, David R Pickens, Graham Thirsk, Gary B Thurman, and Carl G Hellerqvist. Quantified color Doppler sonography of tumor vascularity in an animal model. *Journal of Ultrasound in Medicine*, 18(8):547–551, 1999.

[4] Jonathan M Rubin, Theresa A Tuthill, and J Brian Fowlkes. Volume flow measurement using Doppler and grey-scale decorrelation. *Ultrasound in Medicine & Biology*, 27(1):101–109, 2001.

[5] VXD Yang, A Needles, D Vray, S Lo, BC Wilson, IA Vitkin, and FS Foster. High frequency ultrasound speckle flow imaging-comparison with Doppler optical coherence tomography (DOCT). In *Ultrasonics Symposium, 2004 IEEE*, volume 1, pages 453–456. IEEE, 2004.

[6] W Aoudi, H Liebgott, A Needles, V Yang, FS Foster, and D Vray. Estimation methods for flow imaging with high frequency ultrasound. *Ultrasonics*, 44:e135–e140, 2006.

[7] Alison MY Cheung, Allison S Brown, Viviene Cucevic, Marcia Roy, Andrew Needles, Victor Yang, Daniel J Hicklin, Robert S Kerbel, and F Stuart Foster. Detecting

vascular changes in tumour xenografts using micro-ultrasound and micro-ct follow-ing treatment with VEGFR-2 blocking antibodies. *Ultrasound in Medicine & Biology*, 33(8):1259–1268, 2007.

[8] Domenico Ribatti, Anna Gualandris, Maria Bastaki, Angela Vacca, Monica Iurlaro, Luisa Roncali, and Marco Presta.   New model for the study of angiogenesis and antiangiogenesis in the chick embryo chorioallantoic membrane: the gelatin sponge/chorioallantoic membrane assay. *Journal of Vascular Research*, 34(6):455–463, 1997.

[9] Martin Maibier, Bettina Reglin, Bianca Nitzsche, Weiwei Xiang, Wen Wei Rong, Björn Hoffmann, Valentin Djonov, Timothy W Secomb, and Axel R Pries. Structure and hemodynamics of vascular networks in the chorioallantoic membrane of the chicken. *American Journal of Physiology - Heart and Circulatory Physiology*, 2016.

[10] MS Bartlett. The spectral analysis of point processes. *Journal of the Royal Statistical Society. Series B (Methodological)*, pages 264–296, 1963.

[11] Tom Fawcett.   An introduction to ROC analysis.   *Pattern Recognition Letters*, 27(8):861–874, 2006.

[12] Stephen Z Pinter and James C Lacefield. Objective selection of high-frequency power Doppler wall filter cutoff velocity for regions of interest containing multiple small vessels. *IEEE Transactions on Medical Imaging*, 29(5):1124–1139, 2010.

Chapter 6

Motion Magnification for Endoscopic Surgery

This chapter includes material adapted from:

A. Jonathan McLeod, John S.H. Baxter, Sandrine de Ribaupierre, and Terry M. Peters. Motion Magnification for Endoscopic Surgery. In *Proc. SPIE* 9036: 90360C-1-8, 2014.

A. Jonathan McLeod, John S.H. Baxter, Uditha Jayarathne, Stephen Pautler, Terry M. Peters and Xiongbiao Luo. Stereoscopic Motion Magnification in Minimally-Invasive Robotic Prostatectomy. In *CARE 2015*. *Lecture Notes in Computer Science* 9515: 35-45, 2015

6.1 Introduction

One common problem in endoscopic procedures is the identification and sparing of vessels. When arteries are close to the surface of the tissue, the vessels themselves may be visible

or the tissue might appear to pulsate. While pulsation provides a useful visual cue in identifying vascularized tissue, it is not always visible in challenging cases or in less than ideal conditions. Compared with conventional surgery, in endoscopic procedures the identification of vessels becomes much more challenging because of the lack of haptic feedback and limited view angles. Several methods have been proposed to help identify important vessels during surgery including intraoperative Doppler ultrasound for endoscopic third ventriculostomy [1], atrial venous malformation resections [2] and robotic prostatectomy [3]. Intraoperative ultrasound adds considerable complexity to the procedure, especially in neurosurgical procedures where ultrasound imaging often requires a partial craniotomy or a disposable ultrasound probe to be inserted through the working channel of the endoscope. Alternatively, augmented reality systems have been developed that overlay preoperatively identified vessels on the endoscopic video but require accurate spatial tracking as well as non-rigid registration with preoperative images or intraoperative ultrasound[4]. Here we present an alternative approach for identifying vascularization where small periodic motions are amplified creating a synthetic video in which pulsating tissue is visually enhanced. This approach would be easily integrated into existing surgical work flow without expensive hardware requirements. Motion magnification was first proposed by Liu et al. [5] using explicitly tracked feature points to estimate a motion field. More recently, Eulerian video magnification (EVM)[6, 7] has been developed as an alternative technique that does not require explicit estimation of the motion field. This approach is advantageous in terms of simplicity and computational efficiency and can achieve better results with smooth features. Here, a method based on this technique is developed for endoscopic procedures focusing on two common surgeries: endoscopic third ventriculostomy and robotic prostatectomy.

6.2 Eulerian Video Magnification

The object of video magnification is to synthesize a video amplifying small motion. Following the derivation in Wu et al. [6], let the stationary image be $f(\mathbf{x})$ where $\mathbf{x} = [x_1, x_2]^T$ is a spatial position and $\delta(\mathbf{x}, t)$ is the displacement field at time t. The observed intensity, $I(\mathbf{x}, t)$, in the video is then given by the brightness constancy constraint as:

$$I(\mathbf{x}, t) = f(\mathbf{x} + \delta(\mathbf{x}, t)) \tag{6.1}$$

The goal of motion magnification is to synthesize a video $\hat{I}(\mathbf{x}, t)$ where

$$\hat{I}(\mathbf{x}, t) = f(\mathbf{x} + (1 + \alpha)\delta(\mathbf{x}, t)) \tag{6.2}$$

and α is the magnification factor. If the motion is small, the image may be approximated as being locally linear so that

$$I(\mathbf{x}, t) \approx f(\mathbf{x}) + g(\mathbf{x})\delta(\mathbf{x}, t) \tag{6.3}$$

The corresponding approximation for the synthesized video becomes

$$\hat{I}(\mathbf{x}, t) \approx f(\mathbf{x}) + (1 + \alpha)g(\mathbf{x})\delta(\mathbf{x}, t)$$
$$\approx I(\mathbf{x}, t) + \alpha(I(\mathbf{x}, t) - f(\mathbf{x})) \tag{6.4}$$

where $g(\mathbf{x}) = [\frac{\partial f}{\partial x_1}(\mathbf{x}), \frac{\partial f}{\partial x_2}(\mathbf{x})]$ is the gradient of the image.

Laplacian Pyramid

Directly amplifying all temporal variations in the video, $\bar{I}(\mathbf{x}, t) = I(\mathbf{x}, t) - f(x)$, as suggested by Equation 6.4 will included many unwanted effects from noise, lighting and other sources of motion including camera jitter. Instead, spatiotemporal filtering is used to isolate the variations of the video that occur at the right spatial and temporal frequencies. Wu et al. [6] used image pyramids to decompose the video frames into successive spatial frequency subbands. Image pyramids are created by repeatedly applying filtering and sub-sampling operations to an image so each level in the pyramid contains information at different spatial scales. In a Gaussian pyramid each level is generated by smoothing the previous level with a Gaussian kernel followed by subsampling. This generates a pyramid where each level contains lowpass filtered version of the original. A Laplacian pyramid consists of the differences between consecutive lowpass filtered images in a Gaussian pyramid 6.1. In this pyramid each level is a bandpass filtered version of the original image. To enhance motion, Wu et al., processed each level of a Laplacian pyramid independently with a temporal bandpass filter. By using this filtered image, $I_{BP}(x, t)$, in-place of $\bar{I}$ the enhanced video can be limited to motions occurring at the frequency of interest (ie heart rate). The magnification factor, α, would be decreased at higher levels to keep linear approximation in Equation 6.3 valid. After this processing, the Laplacian pyramid was then collapsed by iteratively upsampling each level and adding it with the bandpass residual from the level above it. Figure 6.2a shows an overview of this method. Since the Laplacian pyramid construction/reconstruction and temporal filtering can be expressed as linear operations, which are associative, identical results can be achieved by applying the temporal filtering after the pyramid is collapsed instead of independently on each level (Figure 6.2b). This can reduce the floating point operations and memory requirements for temporal filtering
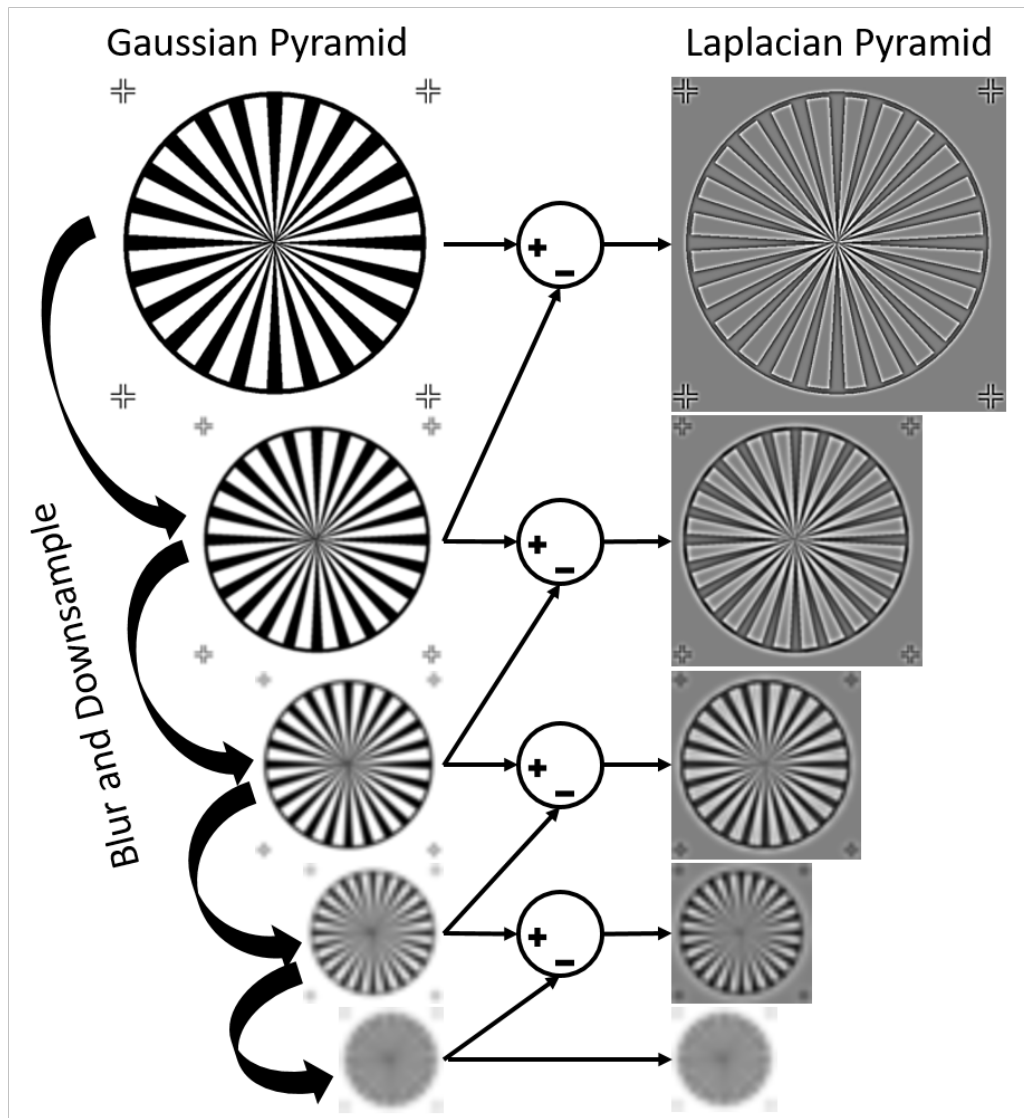
Figure 6.1: Image pyramids are used to decompose the frame into different spatial scales or sub-bands. A Gaussian pyramid is created by repeatedly blurring and downsampling the image. A Laplacian pyramid can be constructed from a Gaussian pyramid by taking the difference between consecutive levels.
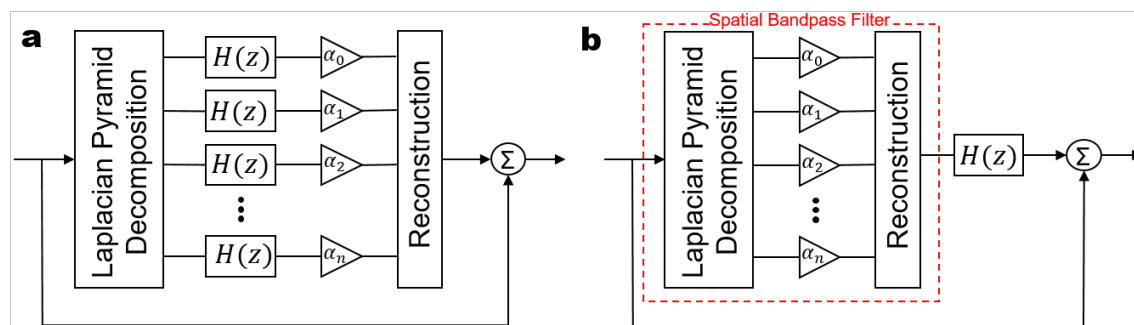
Figure 6.2: Eulerian video magnification using a Laplacian pyramid. (a) Each scale processed independently as presented in [6]. (b) The same processing pipeline with the temporal filtering performed after the Laplacian pyramid is collapsed. Note that the Laplacian pyramid reduces to a spatial band-pass filter.

by one-third since only a single image (the same size as the first level in the pyramid with non-zero α) needs to be processed. More importantly, the entire pyramid processing can thus be replaced by a single spatial bandpass filter. If desired, this filter could be chosen to have the same frequency response as the pyramid method. Alternatively, it could be chosen to maintain the condition proposed by Wu et al., that $(1 + \alpha)\delta$ be less than an eighth wavelength, continuously across all spatial frequencies. We use a difference of Gaussian filter in place of the pyramid since it can easily be adjusted to remove high spatial frequencies where the linear approximation breaks down and more noise is present as well as low spatial frequencies which often contain effects due to endoscopic lighting and other unwanted large scale changes in the image. Visually, a difference of Gaussian filter can produce near identical results to the pyramid method (Figure 6.3).
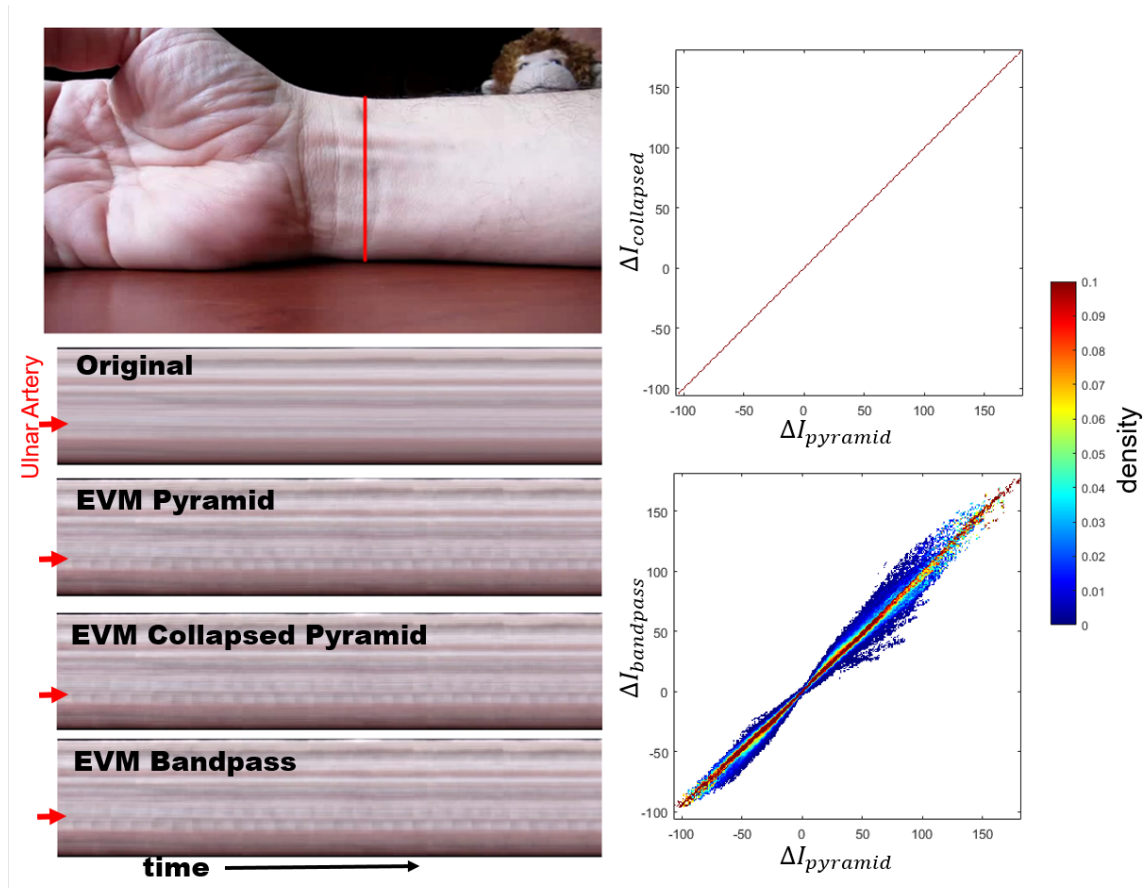
Figure 6.3: The wrist video and supplemental code from [6] were used to to demonstrate spatial processing using a Laplacian pyramid. Identical intensity values were achieved by collapsing the pyramid before applying the temporal filtering. The graphs of $\Delta I = \hat{I} - I$ show that identical intensity values were obtained by collapsing the pyramid before applying the temporal filtering. Replacing the pyramid with a bandpass filter produced very similar results. The time profiles show the pulsation of the ulnar artery after all EVM methods. The bandpass filtering was visually nearly indistinguishable from the pyramid based methods.

Spatiotemporal Filtering

We obtained the motion enhanced image, $\hat{I}(x,t)$, through the pipeline shown in Figure 6.4. This pipeline includes spatial band-pass filtering, adaptive temporal filtering and techniques for artifact reduction.
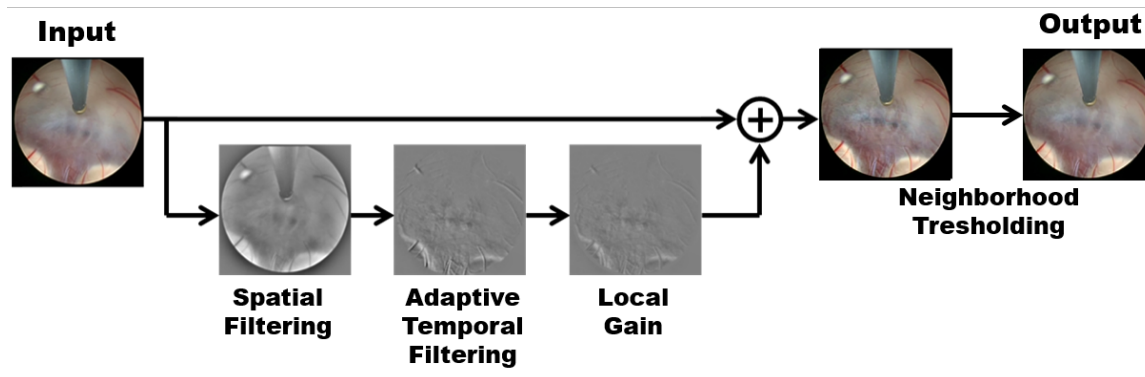
Figure 6.4: Overview of the adaptive magnification with artifact reduction. For simplicity the filtering is shown for the intensity channel only, while in this chapter it is performed on all channels.

The first step in the pipeline is spatial filtering using a difference of Gaussian bandpass filter with high and low pass standard deviations of σ_H and σ_L respectively. This helps remove the high spatial frequency components over which the linear approximation is not valid and also large scale changes in lighting conditions, which are not desirable to amplify. Next, to enhance only the motion due to pulsation, $I_{BP}(x,t)$ is obtained through adaptive filtering so external knowledge of the heart rate is not required. We used an infinite impulse response filter because of its low memory and computational requirements. The *dc* component of the signal is removed using an exponential moving average (EMA) filter and the adaptive line enhancer (ALE) described in Hush et al. [8] is used to enhance cardiac frequencies. Figure 6.5 shows the temporal bandpass filtering algorithm.
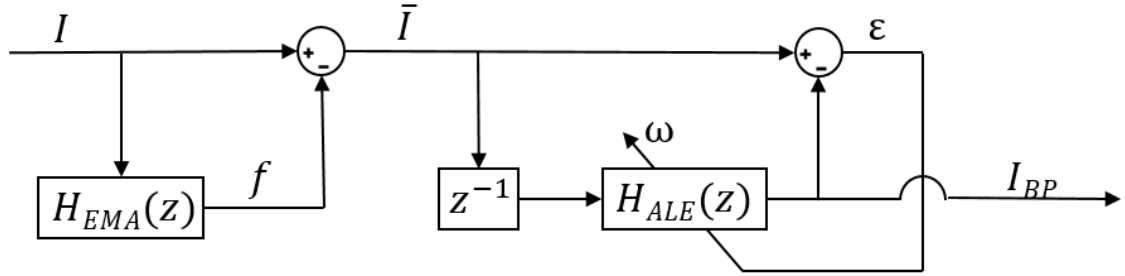
Figure 6.5: This figure shows the adaptive bandpass filtering algorithm. The input, I, is obtained after spatial filtering of the image as described earlier in this section.

The EMA filter is a low pass filter with a transfer function defined by

$$H_{EMA}(z) = \frac{\beta_{EMA}}{1 - (1 - \beta_{EMA})z^{-1}}, \tag{6.5}$$

where $0 < \beta_{EMA} < 1$. This filter estimates the dc component of the signal which is then removed before applying the ALE. The ALE utilizes a band pass filter defined by

$$H_{ALE}(z) = \frac{\frac{1-r^2}{1+r^2}\omega - (1 - r^2)z^{-1}}{1 - \omega z^{-1} + r^2 z^{-2}}, \tag{6.6}$$

where r is a constant that determines the bandwidth of the filter and is the tuning parameter, which is related to the filter's resonance frequency, γ, by

$$\gamma = \cos^{-1} \frac{\omega}{1 + r^2}. \tag{6.7}$$

This filter has the property that $z^{-1}H_{ALE}(z) = 1$ at $z = e^{j\gamma}$ so that it will perfectly predict the next value of a purely sinusoidal input. To form the ALE, a one-step delay is applied to the input and is tuned to minimize the one step prediction error. This is achieved using the same normalized least mean squares algorithm as in Hush et al. [8]; however, we must

minimize the sum of the squared errors across all pixels and color channels instead of for a single channel. The estimate of ω is updated each frame according to

$$\omega_{t+1} = \omega_k + \mu \frac{\sum_p \sum_c \epsilon_t \alpha_k}{\psi_t}, \tag{6.8}$$

where μ is the stepsize constant, ϵ_t is the error in the one step prediction, p and c are the set of all the pixels and channels, which are to be used in updating ω, and a_t is an approximation of the partial derivative of I_{BP} with respect to ω_k given by

$$a_k = \frac{1 - r^2}{1 + r^2} \bar{I}_{t-1} + I_{BP}. \tag{6.9}$$

This approximation leaves out the recursive terms and improves the performance of the optimization when compared with a recursive expression for the partial derivative. The step size is normalized by the square of the gradient magnitude, ψ_k. Low pass filtering of ψ_k is used to prevent sudden changes of the step size which could hamper convergence:

$$\psi_t = (1 - \beta_{ALE})\psi_{t-1} + \beta_{ALE} \sum_p \sum_c a_t^2. \tag{6.10}$$

where $0 < \beta_{ALE} < 1$. The convergence of the estimated heart rate along with the effect of the filtering on moving and static points in the image is shown in Figure 3.
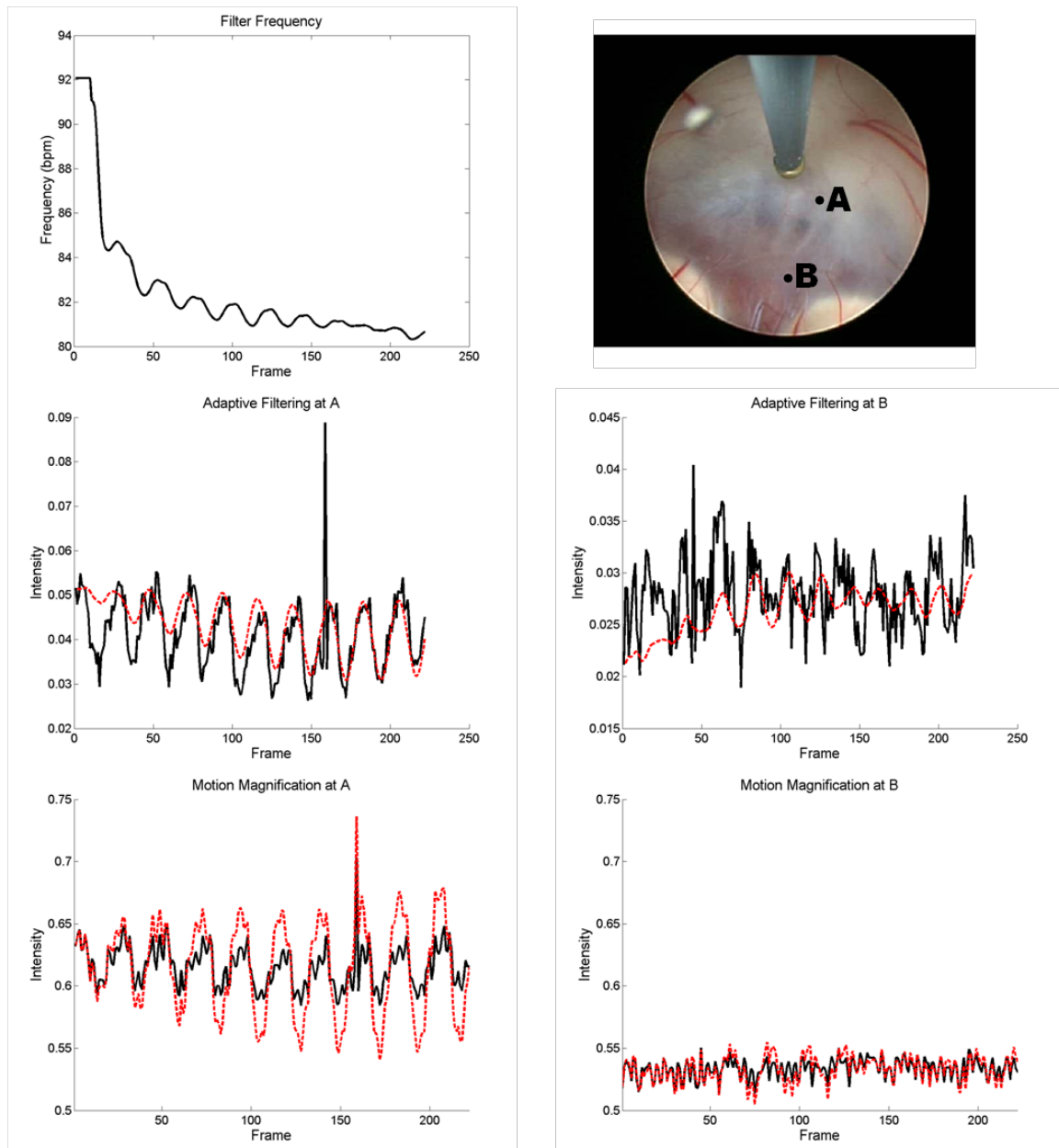
Figure 6.6: The convergence of the filter frequency is shown (top left). The heart rate for this video is approximately 80bpm when averaged across the entire video. The effect of filtering on the intensity signal is shown at the moving and static test points, A and B respectively (top right). For each of these test points the spatial filtered signal (black solid line) and the adaptive filtered signal plus dc, $I_B P + f$, (red dashed line) are shown together in the middle row and the original signal (black solid line) and motion magnified signal (red dashed line) are shown together in the bottom row. The filter begins to catch the fundamental frequency after a couple heart beats. A is greatly enhanced through motion magnification while B remains relatively unchanged.

Artifact Reduction

A rough estimate of the effects of nonlinearity in video magnification can be obtained from the quadratic approximation:

$$I(\mathbf{x}, t) \approx f(\mathbf{x}) + g(\mathbf{x})\delta(\mathbf{x}, t) + \frac{\delta(\mathbf{x}, t)^T H(\mathbf{x})\delta(\mathbf{x}, t)}{2}, \tag{6.11}$$

where $H(x) = \begin{bmatrix} \frac{\partial^2 f}{\partial x_1{}^2} & \frac{\partial^2 f}{\partial x_1 \partial x_2} \\ \frac{\partial^2 f}{\partial x_1 \partial x_2} & \frac{\partial^2 f}{\partial x_2{}^2} \end{bmatrix}$ is the Hessian of the image. When the linear processing in Equation 6.4 is applied to enhance motion, the synthesized video becomes:

$$\begin{aligned} \hat{I}(\mathbf{x}, t) &\approx I(\mathbf{x}, t) + \alpha(I(\mathbf{x}, t) - f(\mathbf{x})) \\ &\approx f(\mathbf{x}) + (1 + \alpha)\left(g(\mathbf{x})\delta(\mathbf{x}, t) + \frac{\delta(\mathbf{x}, t)^T H(\mathbf{x})\delta(\mathbf{x}, t)}{2}\right), \end{aligned} \tag{6.12}$$

while the quadratic estimate for the enhanced video according to Equation 6.11, $\hat{I}_q(x, t)$, would be:

$$\hat{I}_q(\mathbf{x}, t) \approx f(\mathbf{x}) + (1 + \alpha)g(\mathbf{x})\delta(\mathbf{x}, t) + \frac{(1 + \alpha)^2 \delta(\mathbf{x}, t)^T H(\mathbf{x})\delta(\mathbf{x}, t)}{2}, \tag{6.13}$$

leading to an error, ξ:

$$\xi \approx \hat{I}(\mathbf{x}, t) - \hat{I}_q(\mathbf{x}, t) = -\frac{\alpha(1 + \alpha)\delta(\mathbf{x}, t)^T H(\mathbf{x})\delta(\mathbf{x}, t)}{2}. \tag{6.14}$$

This error takes on a maximum when $\delta(\mathbf{x}, t)$ is in the direction of the principle eigenvector of the Hessian:

$$|\xi|_{\max} \approx \frac{\alpha(1 + \alpha)\,|\lambda_0((x)|\,\|\delta(\mathbf{x}, t)\|^2}{2}. \tag{6.15}$$

Weighting the local gain at each pixel location to penalize high $abs\lambda_0$ (principle eigenvalue of the Hessian) can reduce the error. The gain α can be replaced by its local version $\alpha_{local}(\mathbf{x})$ where K is an arbitrary constant:

$$\alpha_{local} = \alpha\, e^{-K|\lambda_0(\mathbf{x})|} \tag{6.16}$$

This is especially beneficial in removing the overshoot artifacts near high contrast regions. In addition to the local weighting, it is useful to threshold the intensities to within the range found in a local neighborhood, N, in the original image. Doing so is consistent with the brightness constancy constraint, assuming the amplified displacement falls within the neighborhood, and ensures that the intensities do not become too extreme in the worst overshoot artifacts. These techniques for reducing artifacts in the magnified video are shown in Figure 6.7.
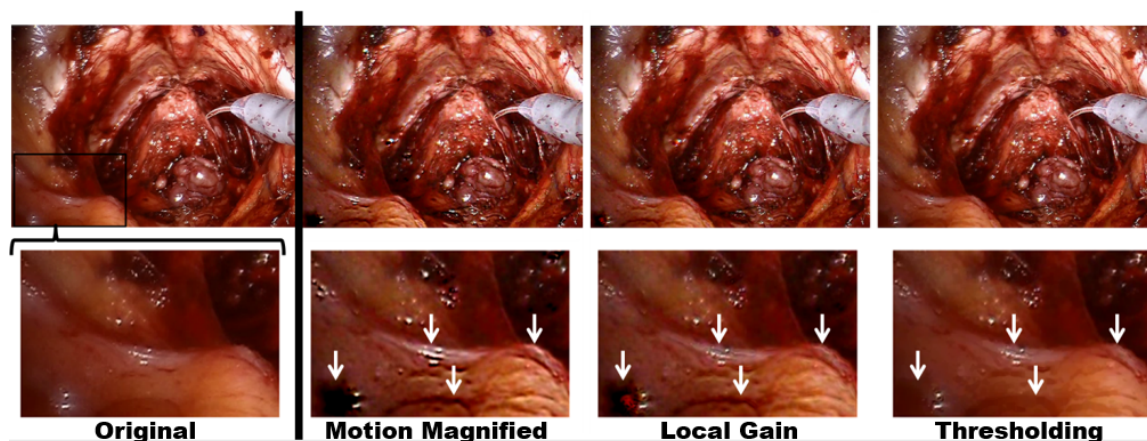
Figure 6.7: A frame from the original video is shown along with corresponding frames from the motion magnified video after each stage of artifact reduction. An enlarged view of a small region in the image is included with white arrows denoting prominent artifacts. Local weighting of the gain reduces the worst artifacts. Finally, thresholding the pixel values to be within the range exhibited by their local neighborhood helps restore the overall brightness in the highlights and shadows. This allows the motion of pulsating structures to be enhanced without large distortions in their intensity and color.

Results

A MATLAB implementation of the described algorithm was run on videos acquired from two procedures that could benefit from video magnification, endoscopic third ventriculostomy (ETV) and robotic prostatectomy. Both of these videos were processed with the same parameters, except for the gain α. Since the prostatectomy procedure had considerably less motion than the ETV, it required a higher gain for the desired pulsation to become visible. The parameters used for the processing are shown in Table 6.1.

Table 6.1: Parameters for motion magnification

	α	σ_H	σ_L	β_{EMA}	r	μ	β_{ALE}	K	N
ETV	5	50	1.5	150	0.98	1e-4	120	150	7x7
Prostate	20	50	1.5	150	0.98	1e-4	120	150	7x7

Endoscopic Third Ventriculostomy

Endoscopic third ventriculostomy (ETV) is a common procedure used to treat hydro-cephalus. In this procedure, the surgeon must fenestrate the floor of the third ventricle between the basilar artery and the clivus. In most patients, the basilar artery is clearly visible through the translucent floor of the third ventricle in the endoscopic video but in some cases the ventricular floor becomes too thick or opaque for the basilar artery to be identified. In these cases there is an increased risk of injury to the basilar artery causing intraventricular hemorrhaging. Many different techniques have been proposed to attempt to deal with opaque ventricular floors, including the use of intraoperative ultrasound [1], but none have seen widespread adoption. If the basilar artery cannot be located, the surgeon will often abort the procedure and install a shunt instead. A system using motion magni-fication to enhance the pulsation of the basilar artery would be very useful in such cases. This technique would not interrupt the surgical work flow and could be activated only when needed for challenging cases. Figure 6.8 shows the results of video magnification applied to endoscopic video acquired during surgery. The enhanced pulsation makes the basilar artery much more prominent making it easier to locate and avoid. This effect is very visible in the processed video file.

Robotic Prostatectomy

Nerve-sparing robotic prostatectomy is another procedure that could benefit from motion magnification. Locating the neurovascular bundles can be challenging and pulsation is a valuable cue for identifying these structures. Tewari et al. used pulsation to identify neu-rovascular bundles during nerve sparing procedures and stressed the importance of thor-oughly removing all blood from the surgical field and using an endoscope with appropriate
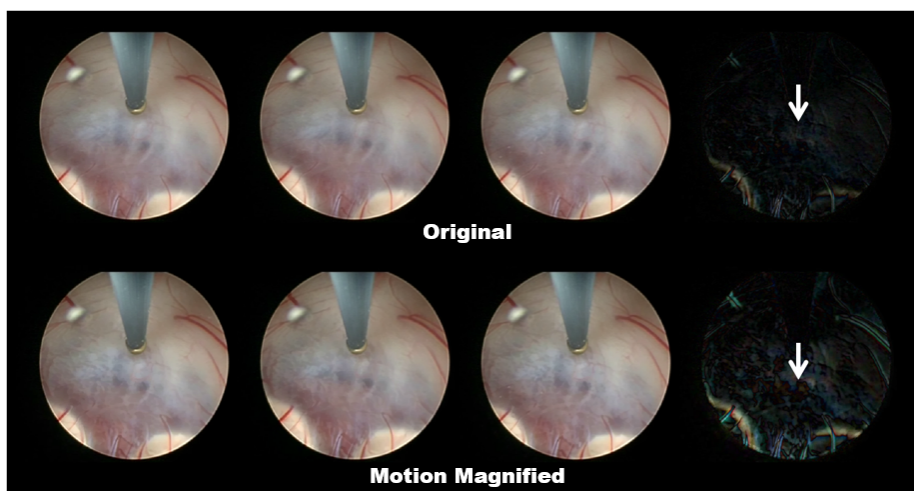
Figure 6.8: The endoscopic video is shown with (bottom) and without (top) motion magnification. The first three columns on the left cover a single cardiac cycle with the leftmost frames being acquired during diastole, the middle frames during systole, and the right frames in diastole again. On the far right are the color difference images between systole and diastole with the absolute value of the RGB intensity differences enhanced by a factor of 2. The motion magnified difference image shows a brighter region along the basilar artery (white arrows) and smaller vessels indicative of motion.

magnification as the pulsation is very subtle [9]. Motion magnification could aid in identifying the neurovascular bundles more easily and in less ideal conditions. This method was applied to an endoscopic video acquired during a robotic prostatectomy where the pulsation is almost imperceptible (Figure 6.9). After magnification the pulsation of even small vessels becomes apparent.

6.3   Future Directions

6.3.1   Identification of Prostatic Artery in Robotic Prostatectomy

While the preliminary investigation of EVM for endoscopic video appears promising there is still considerable work to be done before such a system is ready for clinical use. We are
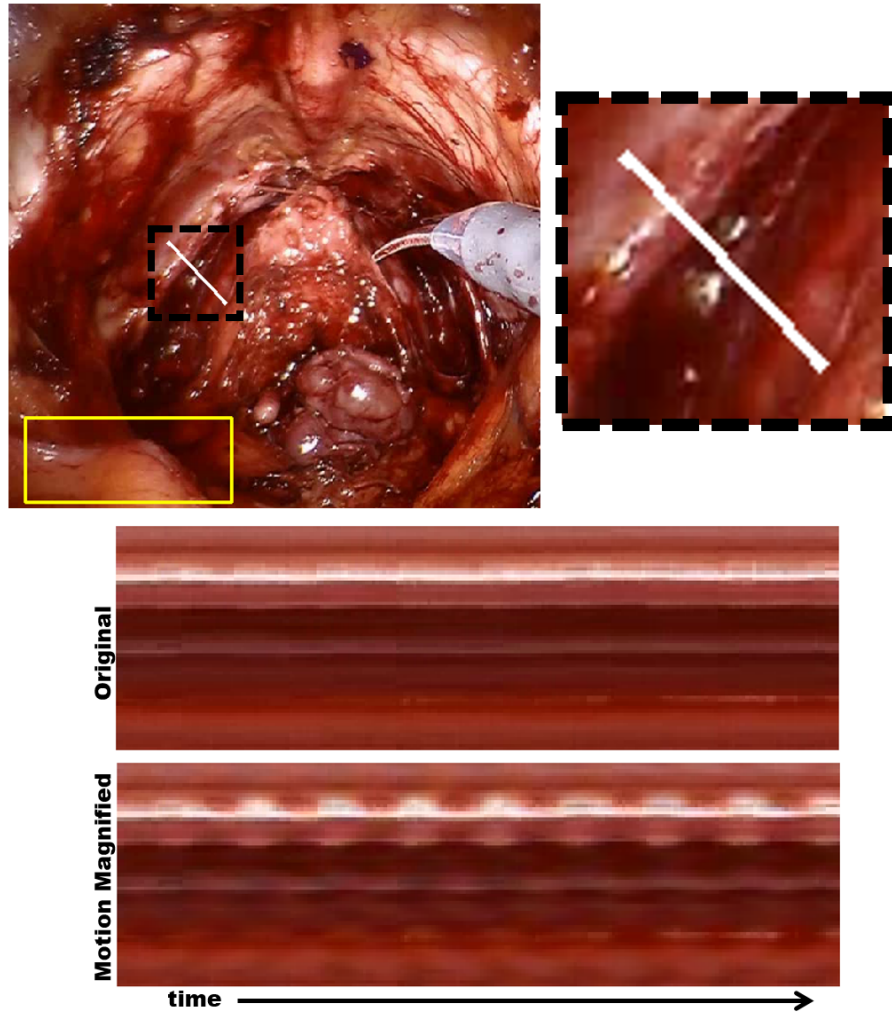
Figure 6.9: A single frame from the endoscopic video of the prostatectomy is shown on the left. The white line intersects the area where the neurovascular bundles are located (enlarged on right). While the original video appears almost completely stationary, a pulsatile motion is visible in the neurovascular area. This can be seen from the time-profile (bottom) and is apparent in the motion magnified video. A sub-region (yellow box) was selected where pulsatile motion was most visible in the surgical field. This sub-region was used for updating the frequency parameter while the bandpass filtering was applied to the entire frame to enhance pulsatile motion.

currently conducting a more in depth study of robotic prostatectomy. In particular, we are interested to see if EVM can improve the saliency of the prostatic artery. These arteries are located medial to neurovascular bundles and can be used as landmarks during nerve-sparing procedures [10]. Although the prostatic artery can be difficult to identify, when the resection plane is medial to neurovascular bundle the amount of residual nerve tissue in the excised prostate is greatly decreased [10]. Currently, twenty one cases have been recorded for retrospective analysis. However, we need to ensure that the methods used produce real-time high quality video that will be useful to the surgeon.

6.3.2   Stereo Endoscopy

Robotic prostatectomy with the da Vinci system uses a stereo endoscope to provide the surgeon with a sense of depth. It is important to ensure that our processing can be applied to stereo video so it can be used by the surgeon without interfering with workflow. The equations for motion magnification were derived based on amplifying 2D displacements in a 2D image. For processing stereoscopic video we want to ensure that the synthesized left and right frames are consistent with amplifying the 3D motion of the object being imaged. Let $\mathbf{z} = [z_1, z_2, z_3]^T$ be a point in 3D space that is mapped to x by the camera projection operator. If $\mathbf{z}$ moves according to the displacement field δ_{3D} then the linear approximation in Equation 6.3 becomes

$$I(\mathbf{x}, t) \approx f(\mathbf{x}) + g(\mathbf{x}) \, J_{\mathbf{z} \to \mathbf{x}} \, \delta_{3D}(\mathbf{z}, t), \qquad (6.17)$$

where $J_{\mathbf{z}\rightarrow\mathbf{x}}$ is the Jacobian of the camera projection. Thus, Equation 6.4 becomes

$$\hat{I}(\mathbf{x},t) \approx f(\mathbf{x}) + (1+\alpha)g(\mathbf{x})\, J_{\mathbf{z}\rightarrow\mathbf{x}}\, \delta_{3D}(\mathbf{z},t)$$
$$\approx I(\mathbf{x},t) + \alpha(I(\mathbf{x},t) - f(\mathbf{x})). \tag{6.18}$$

Applying EVM to any camera projection image is thus consistent with magnifying the underlying 3D motion so long as the camera projection can be approximated as linear and the 3D surface and deformation field are continuous with no self-occlusions. The projection for a simple pinhole camera model with z_3 perpendicular to the imaging plane is

$$[x_1 x_2]^T = [\frac{fz_1}{z_3}, \frac{fz_1}{z_3}]^T, \tag{6.19}$$

which is linear for $\delta_{3D}(\mathbf{z},t) \ll z_3$. This assumption would only be broken if the motion being magnified involved spatial displacements similar in size to the distance between the camera and the target which is antithetical to our purposes of amplifying small, nearly imperceptible motions.

6.3.3 Real-Time Local Phase Processing

One of the main challenges with the EVM is its sensitivity to extraneous sources motion. Phase based variants of EVM [7, 11] amplify changes in the local image phase instead of the raw intensity values. These approaches have a couple of advantages over linear EVM. Displacements can be extrapolated over a much larger range than when using raw intensity [7]. Changes in local phase relate directly to the displacement field as phase shifts in the frequency domain are equivalent to translations in the spatial domain. This allows more sophisticated analysis of the motion to be performed such as masking out large displace-

ments [7] or finding regions with high spatial divergence corresponding to radial distention of an artery [12]. However, local phase processing is more intensive than intensity based EVM and, because computing local phase is non-linear and only valid over a narrow spatial frequency band, the pyramid processing cannot be collapsed. While local phase EVM was originally developed using orientated filter banks [7], the Reisz transform can also be used for motion magnification [11]. We implemented such a GPU accelerated method that could process stereo full resolution (1280x1024) video at 30 fps, producing high-quality videos where subtle pulsations are greatly enhanced. By masking out large changes in local phase, most of the artifacts due to unwanted large motions were eliminated. In addition, subtle organ motion was removed by band-pass filtering the local phase at each level of the pyramid to eliminate large scale motions while retaining more of the localized pulsation of small vessels. This is especially helpful in enhancing pulsation in the prostatic artery as the lateral walls of the prostate visibly pulse with the cardiac cycle. This extraneous motion is larger than that of the prostatic artery, occurs at the same frequency, and dominates the results if not suppressed. For the real-time implementation, the processed stereo video was displayed back to the user on the da Vinci Xi system using TilePro (an auxiliary window which the surgeon could bring up on demand underneath the original video feed). In porcine studies, vessels in the gall-bladder region were used to demonstrate this method (Figure 6.10) as pigs lack prostates.

6.4   Conclusions

Motion magnification shows potential for identifying vessels in a variety of endoscopic or laparoscopic procedures. In the two examples described here, EVM was able to greatly enhance the motion of the basilar artery during endoscopic third ventriculostomy and reveal

the almost imperceptible pulsation around the neurovascular bundles in robotic prostatectomy. This could help surgeons identify these important structures, thus reducing complications and improving patient outcomes. Our future work is focused on validated real-time stereo processing for robotic prostatectomy where this method has the potential to improve the visibility of the prostatic artery and help spare neurovascular tissue.
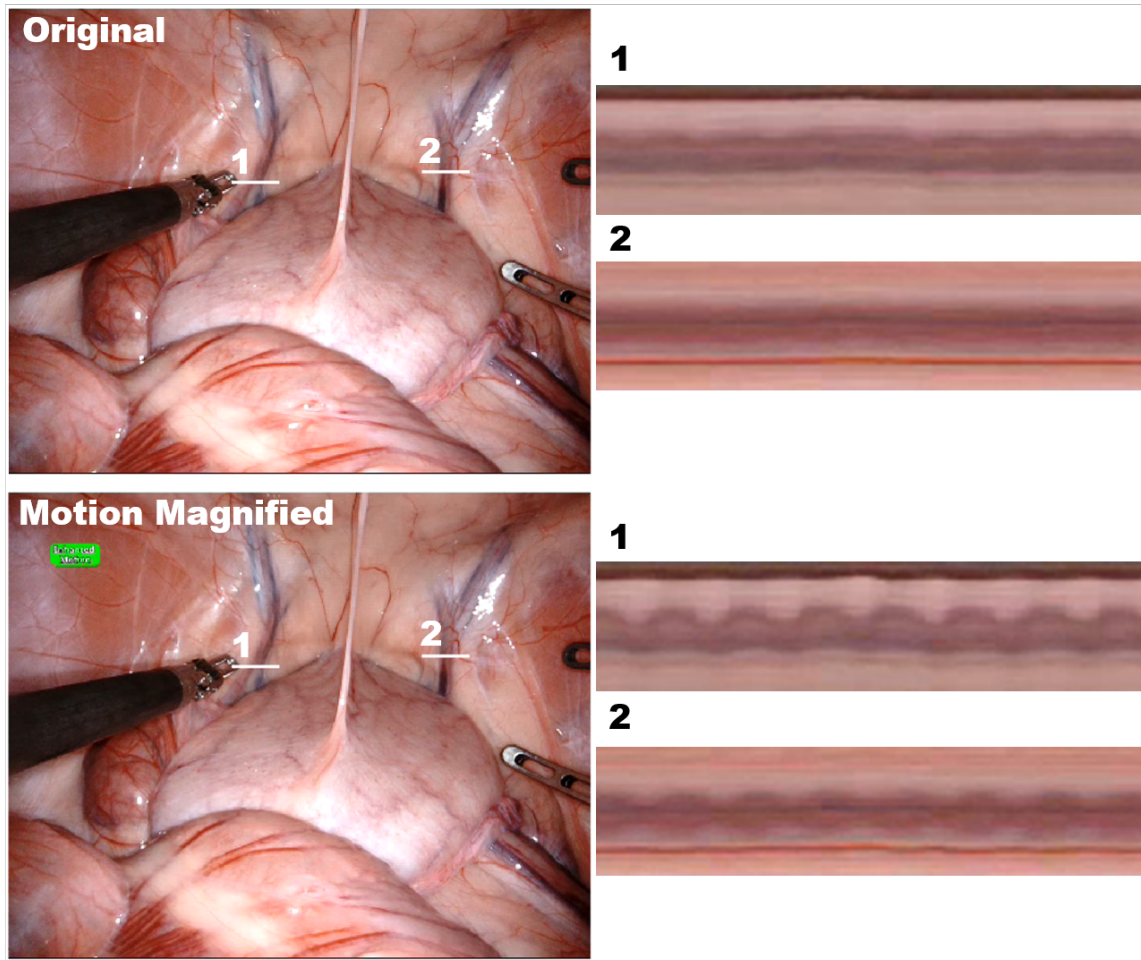
Figure 6.10: Local phase motion magnification running in real-time (30 fps with full resolution stereo video) in a porcine study. Pulsation of the arteries was greatly enhanced while the the overall image quality was preserved. This pulsation can be seen in the two time profiles taken across arteries.

Bibliography

[1] Richard H Schmidt. Use of microvascular doppler probe to avoid basilar artery injury during endoscopic third ventriculostomy. *Journal of Neurosurgery*, 90(1):156–159, 1999.

[2] H Akdemir, S Öktem, A Menkü, B Tucer, B Tuğcu, and O Günaldi. Image-guided microneurosurgical management of small arteriovenous malformation: role of neuronavigation and intraoperative doppler sonography. *Minimally Invasive Neurosurgery*, 50(03):163–169, 2007.

[3] Misop Han, Chunwoo Kim, Pierre Mozer, Felix Schäfer, Shadie Badaan, Bogdan Vigaru, Kenneth Tseng, Doru Petrisor, Bruce Trock, and Dan Stoianovici. Tandem-robot assisted laparoscopic radical prostatectomy to improve the neurovascular bundle visualization: a feasibility study. *Urology*, 77(2):502–506, 2011.

[4] Kozo Konishi, Makoto Hashizume, Masahiko Nakamoto, Yoshihiro Kakeji, Ichiro Yoshino, Akinobu Taketomi, Yoshinobu Sato, Shinichi Tamura, and Yoshihiko Maehara. Augmented reality navigation system for endoscopic surgery based on three-dimensional ultrasound and computed tomography: Application to 20 clinical cases. In *International Congress Series*, volume 1281, pages 537–542. Elsevier, 2005.

[5] Ce Liu, Antonio Torralba, William T Freeman, Frédo Durand, and Edward H Adelson. Motion magnification. *ACM Trans. Graph. (Proceedings SIGGRAPH 2005)*, 24(3):519–526, 2005.

[6] Hao-Yu Wu, Michael Rubinstein, Eugene Shih, John Guttag, Frédo Durand, and William T. Freeman. Eulerian video magnification for revealing subtle changes in the world. *ACM Trans. Graph. (Proceedings SIGGRAPH 2012)*, 31(4), 2012.

[7] Neal Wadhwa, Michael Rubinstein, Frédo Durand, and William T. Freeman. Phase-based video motion processing. *ACM Trans. Graph. (Proceedings SIGGRAPH 2013)*, 32(4), 2013.

[8] D Hush, Nasir Ahmed, Ruth David, and S Stearns. An adaptive iir structure for sinusoidal enhancement, frequency estimation, and detection. *IEEE Transactions on Acoustics, Speech, and Signal Processing*, 34(6):1380–1390, 1986.

[9] Ashutosh Tewari, James O Peabody, Melissa Fischer, Richard Sarle, Guy Vallancien, V Delmas, Mazen Hassan, Aditya Bansal, Ashok K Hemal, Bertrand Guillonneau, et al. An operative and anatomic study to help in nerve sparing during laparoscopic and robotic radical prostatectomy. *European urology*, 43(5):444–454, 2003.

[10] Vipul R Patel, Oscar Schatloff, Sanket Chauhan, Ananthakrishnan Sivaraman, Rair Valero, Rafael F Coelho, Bernardo Rocco, Kenneth J Palmer, and Darian Kameh. The role of the prostatic vasculature as a landmark for nerve sparing during robot-assisted radical prostatectomy. *European urology*, 61(3):571–576, 2012.

[11] Neal Wadhwa, Michael Rubinstein, Frédo Durand, and William T Freeman. Riesz pyramids for fast phase-based video magnification. In *Computational Photography (ICCP), 2014 IEEE International Conference on*, pages 1–10. IEEE, 2014.

[12] Alborz Amir-Khalili, Ghassan Hamarneh, and Rafeef Abugharbieh. Automatic vessel segmentation from pulsatile radial distension. In *International Conference on Medi-*

cal Image Computing and Computer-Assisted Intervention, pages 403–410. Springer, 2015.

Chapter 7

Conclusions

The main objective of this thesis is to use temporal information from intraoperative imaging to improve image guidance. Chapter 2 focused on acquiring and visualizing the intraoperative ultrasound video for positioning tasks in beating heart cardiac surgery. Here, I integrated an ultrasound probe directly into tools for beating heart aortic and mitral valve surgery. In the case of TAVI, the integrated ultrasound allowed the final positioning and monitoring of the expandable valve-stent as it was deployed in the native aortic valve. When combined with augmented reality, this imaging achieved similar variability in deployment depths as conventional fluoroscopic guidance in a phantom model. When used for mitral valve repair using NeoChord, the integrated ultrasound was displayed within the augmented reality guidance system allowing the live ultrasound to be augmented with virtual representations of the valve annuli, previously deployed sutures, and NeoChord jaws. This aided in leaflet capture by providing the necessary context and real-time imaging to evenly deploy sutures along the posterior leaflet.

The remaining chapters dealt with developing techniques to process intraoperative video in order to extract hidden information. Chapters 3 and 4 dealt with periodicity detection

in medical videos. Chapter 3 proposed a method for detecting dural pulsations in spinal ultrasound. These pulsations can provide a valuable cue when performing epidural injections and spinal anesthesia as they appear when the anesthesiologist has a clear path to the epidural space. An extended Kalman filter was used to estimate the frequency and amplitude of pulsations so they could be detected automatically. This method ran in real-time on a commercial ultrasound system and was used in a series of mock-epidural injections in a phantom environment where it decreased the number of needle insertion attempts and tortuosity of the needle path when compared with regular ultrasound guidance. In addition, this processing was included in an augmented reality environment to show how automatically detected dural pulsation could be spatially related to virtual models of the tracked needle and spinal anatomy. Adding real-time image processing to tracked ultrasound in an augmented reality environment is of particular interest. While the virtual objects add a great deal of context that help interpret the ultrasound image, they also add clutter and reduce the screen space available for the ultrasound image (which is then often viewed at an oblique angle in the augmented reality environment). This makes it difficult to identify subtle cues such as dural pulsation in the augmented reality guidance. However, by extracting these cues automatically, the best of both worlds can be achieved with virtual models for the spine and tracked needle and the automatic processing highlights where the dural pulsations show a clear path through the interlamanar space all shown within a single augmented reality environment.

Chapter 4 developed a more general framework, based on dynamic linear modeling, for analyzing periodicity in videos. Like the extended Kalman filtering, this approach relied on state-space modeling of variations in pixel intensity to estimate physically meaningful parameters such as frequency and amplitude of pulsation. However, extended Kalman

filtering for state estimation requires careful tuning and can easily be trapped in local minima. The dynamic linear modeling approach finds maximum likelihood estimates of the parameters. Furthermore, by fitting models both with and without a periodic component, a likelihood ratio test could test for the presence of periodicity. In addition to detecting dural pulsations in spinal ultrasound, the same dynamic linear model was used for both heart rate estimation and perfusion mapping from natural video and ventilation imaging from free-breathing MRI to demonstrate the versatility of this approach.

While the previous two chapters dealt with detecting periodicity in videos, other kinds of statistical analysis can be used to recover hidden temporal information. Chapter 5 demonstrated how blood flow can be segmented from B-mode microvascular ultrasound video. In these videos, flowing blood was effectively decorrelated from one frame to the next while background tissue motions resulted in highly autocorrelated pixel intensities. Using Bartlett's test, a non-parametric, frequency domain, statistical method, blood could distinguished from background clutter. From five second B-mode videos acquired in a chick embryo model this method achieved vessel segmentations with better area under the ROC curve than power Doppler. Qualitatively, this type of processing also revealed more microvasculature inside tumor xenografts which would help in studies of anti-angiogenic cancer drugs.

Chapter 6 dealt with processing endoscopic video using Eulerian video magnification to enhance the pulsation of important arteries. Surgeons already rely on pulsation to find important vessels. Enhancing this pulsation provides natural videos that are easily interpreted by the surgeon where arteries are more salient. This chapter demonstrated how adaptive temporal filtering could be used to track the patient's heart rate, automatically enhancing motions at the cardiac frequency. Additionally, I developed techniques for artifact reduc-

tion that preserved the quality of the enhanced videos. My main focus for future work is to apply these techniques to help identify the prostatic artery in nerve sparing robotic prostatectomy. Towards this end, I implemented GPU accelerated phase based motion magnification capable of processing full resolution stereo video at 30 frames per second. This technique was demonstrated in animal labs and further validation is ongoing through retrospective study on video acquired from human prostatectomy cases.

It is my hope that by developing the techniques described in this thesis, guidance for minimally invasive interventions can be improved. This thesis demonstrated how ultrasound could be integrated into tools for cardiac valve surgery that, together with augmented reality, can be used to position and monitor the deployment of TAVI prosthetic valves or grasp flailing leaflets during beating heart mitral valve repair. Furthermore, it showed how processing videos, acquired from a wide range of medical imaging modalities, could extract hidden temporal information. This information was used to detect dural pulsation from lumbar spine ultrasound in order to guide epidural injections and help surgeons identify critical arteries in endoscopic procedures. These advances have the potential to reduce complications and improve patient outcomes for a wide range of interventions.

Appendix A

Ethics Approval Notices

Western Research

Western University Health Science Research Ethics Board
HSREB Annual Continuing Ethics Approval Notice

Date: October 07, 2016
Principal Investigator: Dr. Nicholas Power
Department & Institution: Schulich School of Medicine and Dentistry\Surgery,London Health Sciences Centre

Review Type: Expedited
HSREB File Number: 104278
Study Title: Predicting drug resistance in metastatic renal cell carcinoma: Individualizing targeted therapy for xenografting patient tumors into chick embryos

HSREB Renewal Due Date & HSREB Expiry Date:
Renewal Due -2017/10/31
Expiry Date -2017/11/05
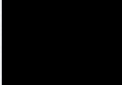
The Western University Health Science Research Ethics Board (HSREB) has reviewed the Continuing Ethics Review (CER) Form and is re-issuing approval for the above noted study.

The Western University HSREB operates in compliance with the Tri-Council Policy Statement Ethical Conduct for Research Involving Humans (TCPS2), the International Conference on Harmonization of Technical Requirements for Registration of Pharmaceuticals for Human Use Guideline for Good Clinical Practice (ICH E6 R1), the Ontario Freedom of Information and Protection of Privacy Act (FIPPA, 1990), the Ontario Personal Health Information Protection Act (PHIPA, 2004), Part 4 of the Natural Health Product Regulations, Health Canada Medical Device Regulations and Part C, Division 5, of the Food and Drug Regulations of Health Canada.

Members of the HSREB who are named as Investigators in research studies do not participate in discussions related to, nor vote on such studies when they are presented to the REB.

The HSREB is registered with the U.S. Department of Health & Human Services under the IRB registration number IRB 00000940.

_____
Ethics Officer, on behalf of Dr. Joseph Gilbert, HSREB Chair

Ethics Officer: Erika Basile ___ Katelyn Harris___ Nicole Kaniki___ Grace Kelly ___ Vikki Tran ___ Karen Gopaul ___

Western Research

Western University Health Science Research Ethics Board
HSREB Delegated Initial Approval Notice

Principal Investigator: Dr. Terry Peters
Department & Institution: Schulich School of Medicine and Dentistry\Medical Biophysics, Robarts Research Institute

HSREB File Number: 106565
Study Title: Video Processing for Laparoscopic and Robotic Surgery
Sponsor: Intuitive Surgical

HSREB Initial Approval Date: May 14, 2015
HSREB Expiry Date: May 14, 2016

Documents Approved and/or Received for Information:

Document Name	Comments	Version Date
Western University Protocol	Revised submission clean	
Letter of Information & Consent		2015/05/11

The Western University Health Science Research Ethics Board (HSREB) has reviewed and approved the above named study, as of the HSREB Initial Approval Date noted above.

HSREB approval for this study remains valid until the HSREB Expiry Date noted above, conditional to timely submission and acceptance of HSREB Continuing Ethics Review.

The Western University HSREB operates in compliance with the Tri-Council Policy Statement Ethical Conduct for Research Involving Humans (TCPS2), the International Conference on Harmonization of Technical Requirements for Registration of Pharmaceuticals for Human Use Guideline for Good Clinical Practice Practices (ICH E6 R1), the Ontario Personal Health Information Protection Act (PHIPA, 2004), Part 4 of the Natural Health Product Regulations, Health Canada Medical Device Regulations and Part C, Division 5, of the Food and Drug Regulations of Health Canada.

Members of the HSREB who are named as Investigators in research studies do not participate in discussions related to, nor vote on such studies when they are presented to the REB.

The HSREB is registered with the U.S. Department of Health & Human Services under the IRB registration number IRB 00000940.

_____
er, on behalf of Dr. Marcelo Kremenchutzky, HSREB Vice Chair

Ethics Officer to Contact for Further Information

Erika Basile	Grace Kelly	Mina Mekhail	Vikki Tran
ebasile@uwo.ca	grace.kelly@uwo.ca	mmekhail@uwo.ca	vikki.tran@uwo.ca

This is an official document. Please retain the original in your files.

LAWSON FINAL APPROVAL NOTICE

LAWSON APPROVAL NUMBER: R-15-220

PROJECT TITLE: Video Processing for Laparoscopic and Robotic Surgery

PRINCIPAL INVESTIGATOR: Dr. Terry Peters

LAWSON APPROVAL DATE: September 15, 2015

Health Sciences REB#:   106565

Please be advised that the above project was reviewed by the Clinical Research Impact Committee and Lawson Administration and the project:

Was Approved

Please provide your Lawson Approval Number (R#) to the appropriate contact(s) in supporting departments (eg. Lab Services, Diagnostic Imaging, etc.) to inform them that your study is starting. The Lawson Approval Number must be provided each time services are requested.


Dr. David Hill
V.P. Research
Lawson Health Research Institute

All future correspondence concerning this study should include the Lawson Approval Number and should be directed to Sherry Paiva, Research Approval Officer, Lawson Health Research Institute, 750 Baseline Road, East, Suite 300.

cc: Administration

Appendix B

Permission to Reproduce Copyrighted Material
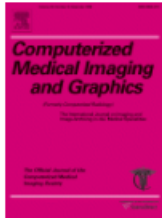
156

Title:	Phantom study of an ultrasound guidance system for transcatheter aortic valve implantation
Author:	A. Jonathan McLeod,Maria E. Currie,John T. Moore,Daniel Bainbridge,Bob B. Kiaii,Michael W.A. Chu,Terry M. Peters
Publication:	Computerized Medical Imaging and Graphics
Publisher:	Elsevier
Date:	June 2016

© 2014 Elsevier Ltd. All rights reserved.

Logged in as:
Jonathan McLeod
Robarts Research Institute (UWO)
Account #:
3001184813

LOGOUT

Order Completed

Thank you for your order.

This Agreement between Robarts Research Institute (UWO) -- Jonathan McLeod ("You") and Elsevier ("Elsevier") consists of your license details and the terms and conditions provided by Elsevier and Copyright Clearance Center.

Your confirmation email will contain your order number for future reference.

Printable details.

License Number	4178591150643
License date	Aug 30, 2017
Licensed Content Publisher	Elsevier
Licensed Content Publication	Computerized Medical Imaging and Graphics
Licensed Content Title	Phantom study of an ultrasound guidance system for transcatheter aortic valve implantation
Licensed Content Author	A. Jonathan McLeod,Maria E. Currie,John T. Moore,Daniel Bainbridge,Bob B. Kiaii,Michael W.A. Chu,Terry M. Peters
Licensed Content Date	Jun 1, 2016
Licensed Content Volume	50
Licensed Content Issue	n/a
Licensed Content Pages	7
Type of Use	reuse in a thesis/dissertation
Portion	full article
Format	electronic
Are you the author of this Elsevier article?	Yes
Will you be translating?	No
Title of your thesis/dissertation	Exploiting Temporal Image Information in Minimally Invasive Surgery
Expected completion date	Dec 2017
Estimated size (number of pages)	160
Requestor Location	Robarts Research Institute (UWO) 151 Richmond St London, ON N6A 3K7 Canada Attn: Jonathan McLeod
Total	0.00 CAD

ORDER MORE | CLOSE WINDOW

Title: Detection and visualization of dural pulsation for spine needle interventions

Author: A. Jonathan McLeod

Publication: International Journal of Computer Assisted Radiology and Surgery

Publisher: Springer

Date: Jan 1, 2015

Copyright © 2015, CARS

Logged in as:
Jonathan McLeod
Robarts Research Institute (UWO)
Account #:
3001184813

LOGOUT

Order Completed

Thank you for your order.

This Agreement between Robarts Research Institute (UWO) -- Jonathan McLeod ("You") and Springer ("Springer") consists of your license details and the terms and conditions provided by Springer and Copyright Clearance Center.

Your confirmation email will contain your order number for future reference.

Printable details.

License Number	4178600005608
License date	Aug 30, 2017
Licensed Content Publisher	Springer
Licensed Content Publication	International Journal of Computer Assisted Radiology and Surgery
Licensed Content Title	Detection and visualization of dural pulsation for spine needle interventions
Licensed Content Author	A. Jonathan McLeod
Licensed Content Date	Jan 1, 2015
Licensed Content Volume	10
Licensed Content Issue	6
Type of Use	Thesis/Dissertation
Portion	Full text
Number of copies	10
Author of this Springer article	Yes and you are the sole author of the new work
Order reference number	
Title of your thesis / dissertation	Exploiting Temporal Image Information in Minimally Invasive Surgery
Expected completion date	Dec 2017
Estimated size(pages)	160
Requestor Location	Robarts Research Institute (UWO) 151 Richmond St London, ON N6A 3K7 Canada Attn: Jonathan McLeod
Billing Type	Invoice
Billing address	Robarts Research Institute (UWO) 151 Richmond St London, ON N6A 3K7 Canada Attn: Jonathan McLeod
Total	0.00 CAD

ORDER MORE | CLOSE WINDOW

Springer
the language of science

Title:	Stereoscopic Motion Magnification in Minimally-Invasive Robotic Prostatectomy
Author:	A. Jonathan McLeod
Publication:	Springer eBook
Publisher:	Springer
Date:	Jan 1, 2016

Copyright © 2016, Springer International Publishing Switzerland

Order Completed

Thank you for your order.

This Agreement between Robarts Research Institute (UWO) -- Jonathan McLeod ("You") and Springer ("Springer") consists of your license details and the terms and conditions provided by Springer and Copyright Clearance Center.

Your confirmation email will contain your order number for future reference.

Printable details.

License Number	4178600584426
License date	Aug 30, 2017
Licensed Content Publisher	Springer
Licensed Content Publication	Springer eBook
Licensed Content Title	Stereoscopic Motion Magnification in Minimally-Invasive Robotic Prostatectomy
Licensed Content Author	A. Jonathan McLeod
Licensed Content Date	Jan 1, 2016
Type of Use	Thesis/Dissertation
Portion	Full text
Number of copies	10
Author of this Springer article	Yes and you are the sole author of the new work
Order reference number	
Title of your thesis / dissertation	Exploiting Temporal Image Information in Minimally Invasive Surgery
Expected completion date	Dec 2017
Estimated size(pages)	160
Requestor Location	Robarts Research Institute (UWO) 151 Richmond St

London, ON N6A 3K7 Canada Attn: Jonathan McLeod |
| Billing Type | Invoice |
| Billing address | Robarts Research Institute (UWO) 151 Richmond St

London, ON N6A 3K7 Canada Attn: Jonathan McLeod |
| Total | 0.00 CAD |

ORDER MORE | CLOSE WINDOW

Jonathan McLeod

Imaging Research Laboratories
Robarts Research Institute, Western University
1151 Richmond St N, London, Ontario, N6A 3K7

Education:

2011-Present   Doctor of Philosophy
Biomedical Engineering
Western University, London, Ontario, Canada
Thesis: "Exploiting Temporal Image Information in Minimally Invasive Surgery"
Supervisor: Terry Peters

2007-2011   Bachelor of Engineering Science
Electrical Engineering
Western University, London, Ontario, Canada
4th Year Project: "Automatic 3D Ultrasound Calibration"
Supervisors: Roy Eagleson and Terry Peters

Refereed Journal Papers:

1. Baxter, J.S., Rajchl, M., **McLeod, A.J**., Yuan, J., Peters, T.M. "Directed acyclic graph continuous max-flow image segmentation for unconstrained label orderings" *International Journal of Computer Vision* 123(3), 415–434 (2017)

2. Luo, X., **McLeod, A.J.**, Pautler, S.E., Schlachta, C.M., Peters, T.M. "Vision-Based Surgical Field Defogging" *IEEE Transactions on Medical Imaging* 36(10): 2021-2030 (2017)

3. Ameri, G., Baxter, J.S., **McLeod, A.J**., Peters, T.M., & Chen, E.C. "Effects of line fiducial parameters and beamforming on ultrasound calibration" *Journal of Medical Imaging,* 4(1), doi:10.1117/1.JMI.4.1.015002 (2017)

4. **McLeod, A.J.**, Currie, M.E., Moore, J.T., Bainbridge, D., Kiaii, B.B., Chu, M.W., & Peters, T.M. "Phantom study of an ultrasound guidance system for transcatheter aortic valve implantation" *Computerized Medical Imaging and Graphics* 50, 24-30 (2016)

5. Currie, M.E., **McLeod, A.J.**, Moore, J.T., Chu, M.W.A., Patel, R., Kiaii, B., Peters, T. "Augmented Reality System for Ultrasound Guidance of Transcatheter Aortic Valve Implantation" *Innovations* 11(1), 31-39 (2016)

6. Rajchl, M., Baxter, J.S.H., **McLeod, A.J**., Yuan, J., Qiu, W., Peters, T.M., Khan, A.R. "Hierarchical max-flow segmentation framework for multi-atlas segmentation with Kohonen self-organizing map based Gaussian mixture modeling" *Medical Image Analysis* 27,45-56(2016)

7. **McLeod, A.J.**, Baxter, J.S.H., Ameri, G., Ganapathy, S., Peters, T.M., & Chen, E.C. "Detection and visualization of dural pulsation for spine needle interventions" *International Journal of Computer Assisted Radiology and Surgery*, 10(6), 947-958 (2015)

8. Chen, E.C.S., **McLeod A.J.,** Baxter, J.S.H., & Peters, T.M. *International Journal of Computer Assisted Radiology and Surgery*, 10(6), 867-878 (2015)

9. Qiu, W., Yuan, J., Kishimoto, J., **McLeod, J.**, Chen, Y., de Ribaupierre, S., Fenster, A. "User-Guided Segmentation of Preterm Neonate Ventricular System from 3-D Ultrasound Images Using Convex Optimization" *Ultrasound in Medicine & Biology*, 41(2), 542-556 (2015)

10. Kayvanrad, M. H., **McLeod, A. J.**, Baxter, J. S., McKenzie, C. A., Peters, T. M. "Stationary wavelet transform for under-sampled MRI reconstruction" *Magnetic Resonance Imaging*, 32(10), 1353-1364 (2014)

Jonathan McLeod

Conference Proceedings:

1   **McLeod. A.J.,** Capaldi, D.P., Baxter, J.S., Parraga, G., Luo, X., & Peters, T.M. "Analysis of Periodicity in Video Sequences Through Dynamic Linear Modeling", *MICCAI 2017 Lecture Notes in Computer Science,* 10434, 386-393 (2016)

2   **McLeod, A.J.,** Baxter, J.S.H., Jayarathne, U.L., Pautler, S., Peters, T.M., Luo, X. "Stereoscopic Motion Magnification in Minimally-Invasive Robotic Prostatectomy", *2nd International MICCAI-Workshop on Computer-Assisted and Robotic Endoscopy, Lecture Notes in Computer Science,* 9515, 35-45 (2015)

3   Ameri, G., Baxter, J.S.H., **McLeod, A.J.,** Peter, T.M., Chen, E.C.S. "Augmented Reality Ultrasound Guidance for Central Line Procedures: Preliminary Results" *The 10th International Workshop On Augmented Environments for Computer Assisted Interventions, Lecture Notes in Computer Science* (2014)

4   Chen, E.C.S., **McLeod, A.J.,** Baxter, S.H., Peters, T.M., "Augmented Reality Ultrasound Guidance for Central Line Procedures: Preliminary Results" *The 10th International Workshop On Augmented Environments for Computer Assisted Interventions, Lecture Notes in Computer Science* (2015)

5   **McLeod, A.J.**, Moore, J.T., Peters, T.M, "Beating heart mitral valve repair with integrated ultrasound imaging" *Proceedings of SPIE* 9415 (2015)

6   Vannelli, C., Moore, J., **McLeod, J.**, Ceh, D., Peters T., "Dynamic heart phantom with functional mitral and aortic valves" *Proceedings of SPIE* 9415: 941503, 1-10, (2015)

7   Ameri, G., **McLeod, A.J.**, Baxter, J.S.H., Chen, E.C.S., Peters, T.M., "Line fiducial material and thickness considerations for ultrasound calibration" *Proceedings of SPIE* (2015)

8   **McLeod, A.J,** Baxter, J.S.H., de Ribaupierre, S., Peters, T.M. "Motion Magnification for Endoscopic Surgery. *Proceedings of SPIE* (2014)

9   Chen, E.C.S., **McLeod, A.J,** Jayarathne, U.L., Peters, T.M. "Solving for free-hand and real-time 3D ultrasound calibration with anisotropic orthogonal Procrustes analysis". *Proceedings of SPIE* (2014)

10   Baxter, J.S.H., Rajchl, M., **McLeod, A.J.**, Khan, A.R., Yuan, J., Peters, T.M., "Smoothness parameter tuning for generalized hierarchical continuous max-flow segmentation". *Proceedings of SPIE* (2014)

11   Ameri, G., Baxter, J.S.H., **McLeod, A.J.**, Jayarathne, U.L., Chen, E.C.S., Peters, T.M., "Synthetic aperture imaging in ultrasound calibration", *Proceedings of SPIE* 9036 (2014)

12   **McLeod. A.J.,** Currie, M., Moore, J., Peters, T.M., "Augmented Reality Guidance System for Transcatheter Aortic Valve Implantation", *Proceedings of the 2nd International MICCAI-Workshop on Computer Assisted Stenting*, 21-28 (2015)

13   Jayarathne, U.L., **McLeod. A.J.,** Peters, T.M., Chen, C.S.E., "Robust Intraoperative US Probe Tracking Using A Monocular Endoscopic Camera", *MICCAI 2013*, *Lecture Notes in Computer Science,* 8151, 363-370 (2013)

14   **McLeod, A.J.**, Moore, J., Lang, P., Bainbridge, D., Campbell, G., Jones, D.L., Guiraudon, G.M., Peters, T.M. "Evaluation of mitral valve replacement anchoring in a phantom". *Proceedings of SPIE* (2012)

15   Lang, P., Rajchl, M., **McLeod, A.J.**, Chu, M., Peters, T.M. "Feature identification for image-guided transcatheter aortic valve implantation". *Proceedings of SPIE* (2012)

16   **McLeod, A.J.**, Moore, J., Lang, P., Bainbridge, D., Campbell, G., Jones, D.L., Guiraudon, G.M., Peters, T.M. "Surgical Phantom for Off-Pump Mitral Valve Replacement". *Proceedings of SPIE* (2011)

Jonathan McLeod

Refereed Conference Abstracts:

1 Currie, M.E., **McLeod, A.J.**, Moore, J.T, Patel, R., Kiaii, B, Chu, M.W.A., & Peters, T.M., "Augmented Reality System for Ultrasound Guidance of Transcatheter Aortic Valve Implantation" *Innovation,* 9(3), 167 (2014)

2 Currie, M.E., **McLeod, A.J.**, Patel, R., Peters, T.M., & Kiaii, B. "Localization of Aortic Annulus with Transesophageal Echocardiography for Transcatheter Aortic Valve Implantation", *Innovation,* 9(3), 225-226 (2014)

3 Kayvanrad, M., **McLeod, A.J.**, Baxter, J.S.H., McKenzie, C.A., Peters, T.M. "T1 Map Reconstruction from Under-sampled KSpace Data using a Similarity Constraint" ISMRM, (2012)

4 Chen, E.C.S., **McLeod, A.J.**, Lang, P., Li, F., Peters, T.M., "Automatic 3D ultrasound calibration using single US volume". *IJCARS*, 6 (Suppl 1), S39-S41, (2011)

Grants

2013-2016 **A.J. McLeod**
"Improved Video Guidance for Minimally Invasive Interventions"
VP Research Support Grant
Western University
$10,000

2015 T. Peters (PI), **J. McLeod**, X. Luo, J Baxter, U. Jayarathne, E. Chen, S. Pautler
"Enhanced endoscopic video for detecting the neurovascular bundles through motion magnification in robotic prostatectomy"
Intuitive Surgical 2015 Technology Research Grant
Intuitive Surgical Inc.
$50,000

Scholarships

2013-2016 Vanier Canadian Graduate Scholarship
Government of Canada
$50,000 per year for 3 years

2012-2013 Ontario Graduate Scholarship
Ontario Ministry of Training, Colleges and Universities
$15,000 for 1 year

2011-2012 NSERC CGS-M
National Science and Engineering Research Council Scholarship
$17,500 for 1 year

2007-2011 UWO President's Continuing Scholarship
Western University
$30,000 over 4 years
A total of nine President's scholarships were awarded in 2007

Jonathan McLeod

Awards

June 2015	3rd Place in IPCAI Oral Presentation Awards

June 2015   3rd Place in IPCAI Oral Presentation Awards
Information Processing in Computer Assisted Interventions

March 2015   2nd Place in IMNO Poster Competition
Imaging Network Ontario: Simulations

June 2013   1st Place in LID Poster Competition
London Imaging Discovery

February 2013   1st Place in IMNO Poster Competition
*Imaging Network Ontario: Building a Better Brain: An Ontario
Neuroimaging Consortium*

February 2012   3rd Place in IMNO Poster Competition
*Imaging Network Ontario: Ontario Consortium in Imaging for
Cardiovascular Therapeutics*

June 2011   Governor General's Academic Medal
*Awarded to the graduating student with the highest academic standing in a
4 year undergraduate honors program
(2 Medals awarded in a graduating class of 6,668 students)*

                       Ontario Professional Engineers Gold Medal in Engineering
*Awarded to the graduating student with the highest average as calculated
over 4 years of study in Engineering
(1st out of 216 students enrolled in 4th year Engineering)*

                       Harry Cross Gold Medal in Electrical Engineering
*Awarded to the graduating student with the highest average as calculated
over the final 2 years of study in Electrical Engineering
(1st out of 56 students enrolled in 4th year Electrical Engineering)*

April 2011   4th Year Project Award
*Awarded for the best 4th year project in Electrical Engineering
Project: "Automatic 3D Ultrasound Calibration"*

October 2010   Hydro One Undergraduate Award
*Awarded to 4th year students in Electrical Engineering based on academic
achievement*
$3,000

                       Jean Ann Maynard Scholarship in Electrical Power Engineering
*Awarded to a 4th year student in Electrical Engineering based on
performance in courses related to power engineering*
$1,700

October 2009   Ontario Professional Engineers Scholarship
*Awarded to undergraduate students in Engineering based on academic
achievement and demonstration of leadership skills*
$1,250

Jonathan McLeod

<table>
<tr><td></td><td>Steinmetz-Wooton Scholarship
Awarded to an undergraduate student enrolled in Physics or Electrical Engineering based on academic achievement
$500</td></tr>
<tr><td>May-August 2008, 2009</td><td>Heart & Stroke Foundation John D. Schultz Science Student Scholarship
$4,000 per summer awarded</td></tr>
<tr><td>February 2008</td><td>Ontario Engineering Competition Social Awareness Award</td></tr>
<tr><td>September 2007</td><td>University of Western Ontario CWSF Gold Medal Entrance Scholarship
$2,000</td></tr>
<tr><td>May 2007</td><td>Canada Wide Science Fair Gold Medal in Engineering
$1,500</td></tr>
<tr><td>July-August 2006, 2007</td><td>Heart & Stroke Foundation Martin L. Willis High School Student Scholarship
$2,250 per summer awarded</td></tr>
</table>

Invited Talks

<table>
<tr><td>November 25th 2017</td><td>"Recovering hidden information from video images in Robot Assisted Radical Prostatectomy"
Imaging Applications in Prostate Cancer
Western University</td></tr>
<tr><td>January 8th 2016</td><td>"Enhanced Endoscopic Video for Detecting the Neurovascular Bundles Through Motion Magnification in Robotic Prostatectomy"
Clinical and Technology Research Grant Symposium
Intuitive Surgical</td></tr>
<tr><td>October 22nd 2014</td><td>"Motion Processing for Image Guided Interventions"
Biomedical Engineering Research Day
Western University</td></tr>
</table>

Oral Presentations

1   **McLeod, A.J.**, Baxter, J.S.H., Ameri, G., Ganapathy, S., Peters, T.M., & Chen, E.C. "Detection and visualization of dural pulsation for spine needle interventions" *IPCAI,* June 24th, 2015, Barcelona, Spain

2   **McLeod, A.J.**, Baxter, J.S.H., Ameri, G., Ganapathy, S., Peters, T.M., & Chen, E.C., *Robarts Research Retreat*, "Visualization of dural pulsation in ultrasound video of the lumbar spine", June 8th, 2015, London, Canada

3   **McLeod, A.J.**, Baxter, J.S.H., Ameri, G., Ganapathy, S., Peters, T.M., & Chen, E.C. "Automatically identifying dural pulsation in ultrasound video of the lumbar spine" *London Health Research Day*, April 1st, 2015, London, Canada

4   **McLeod, A.J.**, Moore, J.T., Peters, T.M, "Beating heart mitral valve repair with integrated ultrasound imaging" *SPIE Medical Imaging*, February 21st-26th, 2015

5   **McLeod, A.J,** Baxter, J.S.H., de Ribaupierre, S., Peters, T.M. "Motion Magnification for Endoscopic Surgery" *SPIE Medical Imaging*, February 15th-20th, 2014

6   **McLeod. A.J.,** Currie, M., Moore, J., Peters, T.M., "Augmented Reality Guidance System for Transcatheter Aortic Valve Implantation", *The 2nd International MICCAI-Workshop on Computer Assisted Stenting*. Nagoya, Japan, September 22, 2013

7   Kayvanrad, M.H., **McLeod, A.J.**, Baxter, J.S.H., McKenzie, C.A., Peters, T.M. "T1 Map Reconstruction from Under-sampled KSpace Data using a Similarity Constraint", *International Society for Magnetic Resonance in Medicine Meeting*. Melbourne, Australia, May 5-11, 2012

8   **McLeod, A.J.**, Moore, J. Guiraudon, G.M., Jones, D.L., Campbell, G., Peters, T.M. "Surgical Phantom for Off-Pump Mitral Valve Replacement". *SPIE Medical Imaging*. Orlando, Florida, February 12-17, 2011

9   Mak,H., **McLeod J.**, Peters, T., "Heart Valve Replacement Training System". *Second Annual Canadian Student Conference on Biomedical Computing*. London, Canada, March 16-18, 2007

Poster Presentations:

1   **McLeod. A.J.,** Capaldi, D.P., Baxter, J.S., Parraga, G., Luo, X., & Peters, T.M. "Analysis of Periodicity in Video Sequences Through Dynamic Linear Modeling", *MICCAI 2017, Lecture Notes in Computer Science,* Quebec City, Canada, September 10-14, 2017

2   **McLeod, A.J.,** Baxter, J.S.H., Jayarathne, U.L., Pautler, S., Peters, T.M., Luo, X. "Stereoscopic Motion Magnification in Minimally-Invasive Robotic Prostatectomy", *2nd International MICCAI-Workshop on Computer-Assisted and Robotic Endoscopy,* Munich, Germany, October 5, 2015

3   **McLeod, A.J.**, Baxter, J.S.H., Ameri, G., Ganapathy, S., Peters, T.M., & Chen, E.C. "Ultrasound video processing for identification of dural pulsation in the lumbar spine" *Imaging Network Ontario: Simulations,* March 30-31, 2015

4   **McLeod, A.J,** Baxter, J.S.H., de Ribaupierre, S., Peters, T.M. "Motion Magnification in Endoscopic Video for Vessel-Sparing Interventions" *Robarts Research Retreat*, London, Canada, June 9, 2014

5   **McLeod, A.J.**, de Ribaupierre, S., Peters, T.M. "Ultrasound Guided Endoscopic Third Ventriculostomy". *London Imaging Discovery*. London, Canada, June 13, 2013 (1st Place)

6   **McLeod, A.J.**, de Ribaupierre, S., Peters, T.M. "Ultrasound Guidance for Endoscopic Third Ventriculostomy". *Imaging Network Ontario: Building a Better Brain: An Ontario Neuroimaging Consortium*. Toronto, Canada, February 4-5, 2013 (1st Prize)

7   **McLeod, A.J.**, Moore, J., Lang, P., Bainbridge, D., Campbell, G., Jones, D.L., Guiraudon, G.M., Peters, T.M. "Off-Pump Mitral Valve Replacement Simulator". *London Imaging Discovery*. London, Canada, June 27, 2012

8   **McLeod, A.J.**, Moore, J., Lang, P., Bainbridge, D., Campbell, G., Jones, D.L., Guiraudon, G.M., Peters, T.M. "Mitral Valve Replacement Simulator for Off-Pump Surgery". *Imaging Network Ontario Symposium: Ontario Consortium in Imaging for Cardiovascular Therapeutics*. Toronto, Canada, February 13-14, 2012 (3rd Prize)

9   **McLeod, A.J.**, Moore, J., Lang, P., Bainbridge, D., Campbell, G., Jones, D.L., Guiraudon, G.M., Peters, T.M. "Evaluation of mitral valve replacement anchoring in a phantom". *SPIE Medical Imaging*, San Diego, California, February 4th-9th, 2012

10   Mak,H., **McLeod J.**,Peters, T. "Training System for Minimally Invasive Heart Valve Replacement Operation", *26th Annual Canadian Biomaterials Society Meeting*. London, Canada, May 25-27, 2007

Jonathan McLeod

Teaching Assistant:

Fall 2011, 2012   Introduction to Digital Image Processing
ECE4445 / MBP4445 / ECE9201 / BME9509 / MBP 9509
Instructor: Hanif Ladak, Ph.D., P.Eng

Winter 2011   Advanced Image Processing and Analysis
ECE4438 / MBP4438 / ECE9202 / BME9519 / MBP 9519
Instructor: Aaron Ward, Ph.D.

Related Activities:

2016, 2017   Chair, Organizing Committee
Computer-Assisted and Robotic Endoscopy MICCAI Workshop

2011-2017   Secretary for IEEE Engineering in Medicine and Biology
Western University Student Chapter

Computer Assisted Medical Interventions Training Program
an NSERC Collaborative Research and Training Experience program at Western University

May-Oct 2016   Medical Imaging Intern
Intuitive Surgical

February 2011   Ontario Engineering Competition: Competition Head for Innovative Design

Reviewer: Physics in Medicine and Biology, Computers in Medicine and Biology, IPCAI

Student Member: IEEE, IEEE EMBS, SPIE, MICCAI